

# LEVEL

REPORT ONR-CR215-237-3F

ADA087621



12

## VALIDATION OF HIGH ANGLE-OF-ATTACK ANALYSIS METHODS

Paul W. Berry  
John R. Broussard  
Sol Gully

THE ANALYTIC SCIENCES CORPORATION  
Six Jacob Way  
Reading, Massachusetts 01867

Contract N00014-75-C-0432  
ONR Task 215-237

20 SEPTEMBER 1979

ANNUAL TECHNICAL REPORT FOR PERIOD 1 FEBRUARY 77 - 31 DECEMBER 78

Approved for public release: distribution unlimited

DDC FILE COPY



PREPARED FOR THE  
OFFICE OF NAVAL RESEARCH ■ 300 N. QUINCY ST. ■ ARLINGTON ■ VA ■ 22217

DTIC  
ELECTRIC  
AUG 7 1980

80 8 4 265

#### CHANGE OF ADDRESS

Organizations receiving reports on the initial distribution list should confirm correct address. This list is located at the end of the report. Any change of address or distribution should be conveyed to the Office of Naval Research, Code 211, Washington, D.C. 22217.

#### DISPOSITION

When this report is no longer needed, it may be transmitted to other organizations. Do not return it to the originator or the monitoring office.

#### DISCLAIMER

The findings and conclusions contained in this report are not to be construed as an official Department of Defense or Military Department position unless so designated by other official documents.

#### REPRODUCTION

Reproduction in whole or in part is permitted for any purpose of the United States Government.

UNCLASSIFIED

(14) TASC-TR-612-3

SECURITY CLASSIFICATION OF THIS PAGE (When Data Entered)

1. REPORT DOCUMENTATION PAGE		READ INSTRUCTIONS BEFORE COMPLETING FORM	
2. GOVT ACCESSION NO.	3. RECIPIENT'S CATALOG NUMBER		
4. TITLE (and Subtitle)	5. TYPE OF REPORT & PERIOD COVERED		
6. AUTHOR(s)	7. PERFORMING ORG. REPORT NUMBER		
8. CONTRACT OR GRANT NUMBER(s)	9. PROGRAM ELEMENT, PROJECT, TASK AREA & WORK UNIT NUMBERS		
10. MONITORING AGENCY NAME & ADDRESS (if different from Controlling Office)	11. REPORT DATE		
12. DISTRIBUTION STATEMENT (of this Report)	13. NUMBER OF PAGES		
14. KEY WORDS (Continue on reverse side if necessary and identify by block number)	15. SECURITY CLASS. (of this report)		
16. ABSTRACT (Continue on reverse side if necessary and identify by block number)	17. DECLASSIFICATION/DOWNGRADING SCHEDULE		

1. REPORT DOCUMENTATION PAGE

2. GOVT ACCESSION NO. AD-A287621

3. RECIPIENT'S CATALOG NUMBER

4. TITLE (and Subtitle) Validation of High Angle-of-Attack Analysis Methods.

5. TYPE OF REPORT & PERIOD COVERED Annual Technical rept. 1 Feb 1977 - 31 Dec 1978

6. AUTHOR(s) Paul W. Berry, John R. Broussard and Sol W. Gully

7. PERFORMING ORG. REPORT NUMBER TR-612-3

8. CONTRACT OR GRANT NUMBER(s) N00014-75-C-0432

9. PROGRAM ELEMENT, PROJECT, TASK AREA & WORK UNIT NUMBERS

10. MONITORING AGENCY NAME & ADDRESS (if different from Controlling Office) The Analytic Sciences Corporation  
Six Jacob Way  
Reading, Massachusetts 01867

11. REPORT DATE 20 Sep 1979

12. DISTRIBUTION STATEMENT (of this Report) Approved for public release; distribution unlimited.

13. NUMBER OF PAGES 182

14. KEY WORDS Aircraft Stability and Control, Atmospheric Flight Mechanics, Modern Control Theory, Human Operator Dynamics, Pilot Model Analysis, Air Combat Maneuvering, Digital Flight Control, Hypothesis Testing.

15. SECURITY CLASS. (of this report) UNCLASSIFIED

16. ABSTRACT (Continue on reverse side if necessary and identify by block number) This report extends, applies, and validates the aircraft stability and control methodologies developed by TASC and reported in ONR-CR-215-237-2. These methodologies enable the prediction of airframe stability boundaries, control power difficulties, and stability boundaries of the combined pilot, control system, and aircraft. In the realm of control system design, these methods enable the construction of digital command augmentation systems.

DD FORM 1473

EDITION OF 1 NOV 65 IS OBSOLETE

UNCLASSIFIED

SECURITY CLASSIFICATION OF THIS PAGE (When Data Entered)

404565

Eun

## 20. Abstract (Continued)

which provide precise command response over the entire flight regime while augmenting the airframe stability characteristics. The design of an air combat digital flight control system for the F-14A is described in this report, and its performance is verified by the use of a nonlinear six-degree-of-freedom aircraft simulation and an air combat pilot model. Comparison of the tracking accuracy of the DFCS-aircraft to that of a conventionally controlled aircraft indicates that the DFCS provides better tracking and reduces the likelihood of control-induced departure. In the realm of pilot model validation, a method of choosing the best model among those hypothesized is described and its operation demonstrated. Piloted simulation data are processed which indicate that the pilot does not change his control strategy to correspond to changes in the aircraft flight condition. Not only does this validate the pilot-aircraft stability boundary calculation method, but it has significant control system design implications, since design of control system with uniform handling qualities is shown to be important. The methods and results presented in this study can have substantial impact on the development, analysis, and testing of high performance aircraft, enhancing safety, reliability, and effectiveness of flight operations.

## PREFACE

This investigation was conducted by The Analytic Sciences Corporation, Reading, Massachusetts, from 1 February 1975 under Contract N00014-75-C-0432 for the Office of Naval Research, Washington, D.C. This report is the third annual technical summary, and includes results through 31 December 1978. The sponsoring office was the Vehicle Technology Program, headed by Mr. David Siegel. Mr. Robert von Husen served as the Naval Technical Monitor for the program.

We would like to thank the Langley Research Center of the National Aeronautics and Space Administration, the Naval Air Development Center, and the Naval Air Systems Command for providing data and discussion which were helpful in conducting this research.

Engineering investigations were made by Mr. John R. Broussard and Mr. Paul W. Berry. Dr. Sol W. Gully provided technical guidance for the program.

Accession For	
NTIS GRA&I	<input checked="checked" type="checkbox"/>
DIC TAB	<input type="checkbox"/>
Unannounced	<input type="checkbox"/>
Justification	<input type="checkbox"/>
By	
Date	
Initials	
Signature	
DIST	Special

A

## TABLE OF CONTENTS

	<u>Page No.</u>
PREFACE	iii
List of Figures	vi
List of Tables	ix
1. INTRODUCTION	1
1.1 Background	1
1.2 Organization of This Report	4
2. AIR COMBAT DIGITAL FLIGHT CONTROL SYSTEM DESIGN	5
2.1 Type 0 and Type 1 Digital Controllers	5
2.2 Pseudoinverse Weighting Matrix for Fighter Aircraft Applications	13
2.3 Synthesis of Controllers Using Continuous-Time Specifications	18
2.4 Comparison of Discrete DFCS Type 0 and Type 1 Response	26
2.5 Design Performance at Thirty Flight Conditions	38
2.6 Effects of Gain Scheduling	45
2.7 Chapter Summary	50
3. EVALUATION OF A FIGHTER AIRCRAFT DIGITAL FLIGHT CONTROL SYSTEM BY NONLINEAR SIMULATION	54
3.1 Overview	54
3.2 Simulation Description and Test Procedure	55
3.2.1 Nonlinear 6-DOF Aircraft Simulation	55
3.2.2 ACM Pilot Model	57
3.2.3 ACM Tracking Tasks	61
3.3 Control System Candidates	62
3.4 Trajectory Tracking in the Wind-Up Turn	69
3.5 Accuracy in the Rolling Reversal	79
3.6 Digitally-Augmented Conventional Control System	85
3.7 Chapter Summary	
4. PILOT MODEL HYPOTHESIS TESTING	91
4.1 Introduction	91
4.2 Optimal Control Pilot Model with the Padé Approximation	97
4.3 Hypothesis Testing	104
4.4 Verification with Synthetic Data	106
4.5 Flight Test Selection	112

TABLE OF CONTENTS (Continued)

	<u>Page No.</u>
4.6 Tracking Task Model	119
4.7 Pursuit Tracking Pilot Model Parameters	122
4.8 Hypothesis Testing Results	125
4.9 Chapter Summary	133
5. CONCLUSIONS AND RECOMMENDATIONS	135
5.1 Summary and Conclusions	135
5.2 Recommendations	137
REFERENCES	141
APPENDIX A - AIRCRAFT EQUATIONS OF MOTION	145
APPENDIX B - AIR COMBAT EQUATIONS OF MOTION	164
APPENDIX C - HYPOTHESIS TESTING	168
APPENDIX D - LIST OF SYMBOLS	175

# LIST OF FIGURES

<u>Figure No.</u>		<u>Page No.</u>
1	Flight Vehicle Analysis Methods	3
2	Effects of Changing Flight Condition on Quad Partition Inverse Elements	17
3	Flight Conditions for DFCS Point Design	20
4	Comparison Between Continuous-Time and Mapped Discrete-Time Closed-Loop System Eigenvectors for the Dutch Roll Mode	25
5	Normal Acceleration Step Response at Design Point 1	30
6	Control Movements for Normal Acceleration Step Responses	31
7	Type 1 DFCS $\Delta a_n$ Step Response	33
8	Type 1 DFCS $\Delta p_w$ Step Response	33
9	Type 1 DFCS $\Delta \beta$ Step Response	34
10	Type 0 DFCS $\Delta a_n$ Step Response	34
11	Type 0 DFCS $\Delta p_w$ Step Response	35
12	Type 0 DFCS $\Delta \beta$ Step Response	35
13	Effects of a Normal Acceleration Command Which Saturates Maneuver Flap	37
14	Effects of the Gain Schedule on Closed-Loop Type 1 DFCS Mapped Eigenvalues	47
15	Effects of the Gain Schedule on Closed-Loop Type 1 DFCS Mapped Eigenvalues	47
16	Control Gain Variation with Angle of Attack ( $V = 183 \text{ m/s (600 fps)}$ , $p_w = 0 \text{ deg/sec}$ )	49
17	Control Gain Variation with Angle of Attack ( $V = 183 \text{ m/s (600 fps)}$ , $p_w = 0 \text{ deg/sec}$ )	50



LIST OF FIGURES (Continued)

<u>Figure No.</u>		<u>Page No.</u>
18	DFCS Step Response Performance at the Design Flight Condition	51
19	Test Structure	55
20	ACM Pilot Model	59
21	Wind-up Turn Trajectory Inputs	61
22	Rolling Reversal Trajectory Inputs	63
23	Conventional Control System	64
24	Digital Flight Control System	66
25	Digitally-Augmented Conventional Control System	68
26	DFCS Command Response in the Wind-up Turn	70
27	DFCS Control Surface Trajectories in the Wind-up Turn	72
28	Roll Angle Comparison for the Turn Entry	73
29	Aerodynamic Angle Response of the Conventional Control System (sas Off)	74
30	Stabilator Time Histories for a Conventionally-Controlled Aircraft in the Wind-up Turn	76
31	DFCS Aircraft in Bank-to-Bank at High Angle of Attack	77
32	Control Induced Departure for Conventional Control System	78
33	Roll Rate Accuracy in the Rolling Reversal	81
34	Angle of Attack Response in the Rolling Reversal	82
35	Sideslip in the Rolling Reversal	83
36	Rudder Time Histories in the Rolling Reversal	84
37	Digitally-Augmented Conventional Aircraft in the Rolling Reversal - Roll Rate and Angle of Attack	87

LIST OF FIGURES (Continued)

<u>Figure No.</u>		<u>Page No.</u>
38	Digitally-Augmented Conventional Aircraft in the Rolling Reversal - Sideslip and Rudder	89
39	Block Diagram of the Pilot Model Containing the Padé Approximation to Pure Time Delay	102
40	Pilot Model Hypothesis Testing Results for Different Feedback Gains	108
41	Pilot Model Hypothesis Testing Results for Different Time Delays	109
42	Pilot Model Hypothesis Testing Results for Different Neuromotor Noise	110
43	Pilot Model Hypothesis Testing Results for Different Neuromotor Noise Covariance and High-Passed Data	111
44	Pursuit-Tracking Task	113
45	Aircraft State Time Histories	115
46	Postprocessing of Flight Data to Obtain Target Dynamics	123
47	Comparison of Actual and Predicted Pilot Controls	129
48	Pilot Model Probabilities	131

## LIST OF TABLES

<u>Table No.</u>		<u>Page No.</u>
1	Transformation of the Continuous-Time Optimal Control Problem to Discrete-Time	7
2	Solution of the Discrete-Time Optimal Control Problem	8
3	Effects of Changing the Psuedoinverse Weighting Matrix on Quad Partition Inverse Elements	16
4	DFCS Weights at Design Point 1	22
5	Comparison Between Continuous-Time and Mapped Discrete-Time Closed-Loop System Eigenvalues	24
6	Comparison of Type 1 Discrete Closed-Loop Eigenvalues at Design Point 1 for Different Pseudoinverse Weighting Matrices	28
7	Type 1 DFCS Mapped Closed-Loop Eigenvalues for the Control Sweep	39
8	Type 0 DFCS Mapped Closed-Loop Eigenvalues for the Control Sweep	41
9	Step Response Characteristics for the Type 1 DFCS Sweep	43
10	Control Channel Details	58
11	ACM Pilot Model Gains	60
12	Pilot Model Assumptions	98
13	Elements of the Pilot-Aircraft System Model	101
14	Linearized Tracking Model Dynamics	120
15	Square Root of Pilot Model Cost Function Weights	125
16	Pilot-Model-Aircraft Closed-Loop Eigenvalues	126
17	Pilot Model Lateral Stick Gains	126

1.

## INTRODUCTION

### 1.1 BACKGROUND

Highly maneuverable aircraft must achieve good handling qualities over a wide range of flight conditions. The aircraft control system designer's task is difficult because the flight conditions for such aircraft involve high accelerations and rapid rolling. Additionally, significant changes in control power, or even control reversals, can occur at some flight conditions. The control system developed for such aircraft must be a command augmentation system (cas), which has two functions to perform. The first is to act as a stability augmentation system (sas), which modifies and damps the natural fast modes of motion of the aircraft (short period, Dutch roll and roll mode) so that the pilot has a "well-behaved" platform from which to prosecute the engagement. The second control system function consists of control response augmentation. The control system must modify the basic control response of the aircraft so that the response appears uniform over the range of flight conditions. Lateral stick should always produce similar aircraft roll response, longitudinal stick should always produce similar (although velocity-scaled) normal acceleration response, and pedals should always produce similar yawing motion. This uniformity of response is important, since the pilot is under a severe work load in maneuvering flight and should not be forced to attempt to adapt his input strategy to the specific aircraft flight condition -- a difficult task at best.

The complexity of the command-augmentation task implies a digital implementation of the aircraft control system, specifically a full-authority digital flight control system (DFCS). In principle, the pilot's control stick and pedal inputs drive the DFCS computers, which then command the control surface deflections. Previous work has been concerned with stability and control analysis techniques (Refs. 1 and 2) and control system design techniques (Refs. 3 and 4) that are intended to provide solutions to the control system designer's difficulty. This report details work done to extend and verify these analysis and design techniques. Figure 1 outlines the relationships among the flight vehicle analysis tools and illustrates the two portions of the program examined in this report: control system construction and validation using a nonlinear simulation, and pilot model hypothesis testing.

As illustrated in Fig. 1, the performance of the improved DFCS designs developed in this report are evaluated with a nonlinear 6-DOF aircraft model. An aircraft response comparison is made with the same pilot inputs but with different control systems: the DFCS and the conventional control system (with and without analog augmentation). Maneuvers are also simulated with a conventional mechanical control system with the DFCS driving only the limited-authority rudder actuators. The latter implementation of the DFCS has promise for the retrofit of present-day aircraft, and it has a major impact on the reliability-redundancy issue.

Previous work (Ref. 3) also demonstrated the usefulness of optimal control pilot models in determining pilot/aircraft stability boundaries. While Ref. 3 shows that these stability boundaries compare favorably with actual pilot response, no attempt was made there to verify the details of the pilot model predicted response. This report considers a method

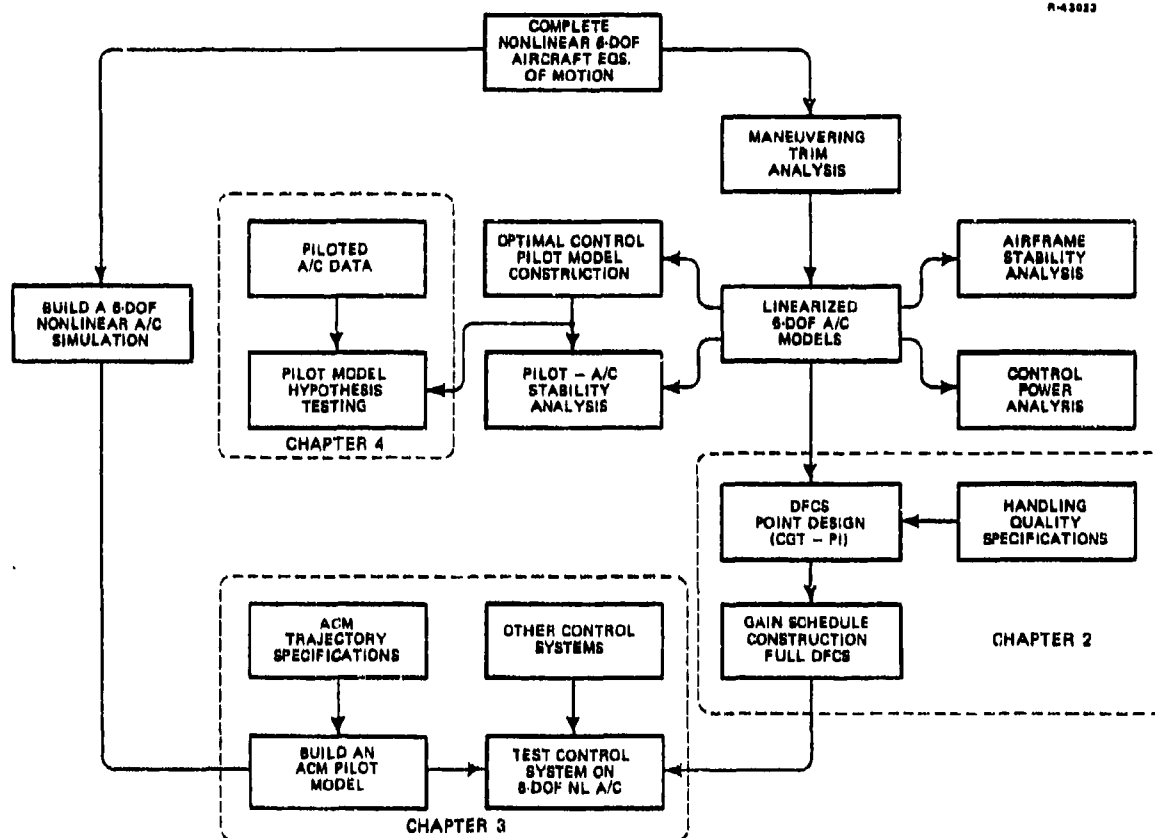


Figure 1 Flight Vehicle Analysis Methods

that can be used to verify pilot modeling techniques: hypothesis testing. In this method the pilot model that best matches the data among a set of hypothesized pilot models is chosen. In the application presented in this report, data from a full-order, nonlinear piloted simulation (the Differential Maneuvering Simulator at NASA Langley Research Center) is used to test the accuracy of the predictions of several different optimal control pilot models.

## 1.2 ORGANIZATION OF THIS REPORT

The research contained in this report draws heavily on past work TASC has performed for ONR (Ref. 3). Chapter 2 of this report details the four-step DFCS design procedure that has been developed at TASC; its application to the design of a control system for the F-14A is also discussed there\*. The DFCS is tested in Chapter 3 b. comparing its performance with that of a conventional control system in accurately controlling the aircraft along rapid ACM trajectories. Validating the prediction of piloting control strategy using a pilot model is addressed in Chapter 4, where a hypothesis testing procedure is discussed. Actual validation and testing with piloted simulation data is included. The conclusions of this report and recommendations concerning useful extensions of this work are given in Chapter 5.

---

\*Figure 1 illustrates the organization of the report.

2.

## AIR COMBAT DIGITAL FLIGHT CONTROL SYSTEM DESIGN

Two digital flight control systems (DFCS) for a highly maneuverable fighter aircraft are designed and described in this chapter. The objective is to develop and demonstrate digital flight control design technology which can improve the performance and mission effectiveness of a fighter aircraft. Based on coupled dynamic models of the aircraft, the two designs are formulated using modern control techniques as a Type 0 and Type 1 DFCS. The designs occur concurrently, since the control laws are related through an algebraic transformation. However, their implementation and response to any disturbances and modeling errors are different. These design differences are also discussed here.

The two DFCS designs have a fly-by-wire configuration and can be easily implemented in a digital flight computer. The three pilot commands used in the two DFCS are the same as in Ref. 3 (normal acceleration, stability-axis roll rate, and sideslip angle) and are transformed by each control law to five separate control surface deflections. This unique feature of the controllers whereby each control surface is deflected independently in an optimal coordinated fashion, will figure prominently in many of the discussions in the following sections.

### 2.1 TYPE 0 AND TYPE 1 DIGITAL CONTROLLERS

A Type 0 DFCS tracks constant commands without using a pure integration in the forward loop. The Type 0 DFCS relies



on proper choice of the matrix which feeds forward the command to achieve tracking. A Type 1 DFCS tracks constant commands with zero steady-state error by using a pure integration in the forward loop. The Type 1 DFCS asymptotically estimates the proper vector to feed forward to the control to maintain tracking.

Procedures for obtaining the Type 0 and Type 1 DFCS structures using optimal control are detailed fully in Refs. 3 to 10. The proportional-integral controller structure in incremental form developed in Ref. 7 has been programmed into a helicopter control minicomputer and successfully flight tested; it will be the structure used in this study.

The Type 0 and Type 1 control laws are obtained by forming a continuous-time optimal control problem, transforming the problem to discrete-time using the sampled-data regulator, then solving the discrete-time problem. The continuous-time linearized model of the aircraft with adjoined compensator states is shown in Table 1 along with the optimal control problem transformation accomplished by the computer algorithms during the design process. The designer works in continuous time by specifying the cost function weights  $Q$  and  $R$  and computer algorithms determine the discrete time weights  $\hat{Q}$ ,  $\hat{M}$ , and  $\hat{R}$ . The optimal control problem is solved using the Riccati equation in Table 2 and the Type 0 and Type 1 gains are computed. The Type 0 and Type 1 gains are found from the same optimal control solution and result in the same closed-loop eigenvalues and state eigenvectors if the number of controls equals the number of commands.

Table 2 shows the perturbation Type 1 control law which operates near the nominal controls,  $u_0$ , and state,  $x_0$ . As shown in Ref. 7, the Type 1 control law can be implemented

TABLE 1  
TRANSFORMATION OF THE CONTINUOUS-TIME OPTIMAL CONTROL  
PROBLEM TO DISCRETE-TIME T-2901

CONTINUOUS-TIME AIRCRAFT MODEL ERROR DYNAMICS WITH COMPENSATOR

$$\begin{bmatrix} \Delta \dot{x} \\ \Delta \dot{u} \end{bmatrix} = \begin{bmatrix} F & G \\ 0 & 0 \end{bmatrix} \begin{bmatrix} \Delta x \\ \Delta u \end{bmatrix} + \begin{bmatrix} 0 \\ I \end{bmatrix} \Delta v$$

CONTINUOUS-TIME COST FUNCTION

$$J = \int_0^{\infty} \left\{ \begin{bmatrix} \Delta x^T & \Delta u^T \end{bmatrix} Q \begin{bmatrix} \Delta x \\ \Delta u \end{bmatrix} + \Delta v^T R \Delta v \right\} dt$$

DISCRETE-TIME MODEL

$$\Phi = e^{F \Delta t} \quad \Gamma = \int_0^{\Delta t} e^{F \tau} d\tau G$$

$$\begin{bmatrix} \Delta x \\ \Delta u \end{bmatrix}_{k+1} = \begin{bmatrix} \Phi & \Gamma \\ 0 & I \end{bmatrix} \begin{bmatrix} \Delta x \\ \Delta u \end{bmatrix}_k + \begin{bmatrix} 0 \\ \Delta t I \end{bmatrix} \Delta v_k$$

DISCRETE-TIME COST FUNCTION

$$J = \sum_{k=0}^{\infty} \begin{bmatrix} \Delta x^T & \Delta u^T & \Delta v^T \end{bmatrix}_k \begin{bmatrix} \hat{Q} & \hat{M} \\ \hat{M}^T & \hat{R} \end{bmatrix} \begin{bmatrix} \Delta x \\ \Delta u \\ \Delta v \end{bmatrix}_k$$

DISCRETE-TIME WEIGHTING MATRICES

$$\hat{Q} = \int_0^{\Delta t} e^{\begin{bmatrix} F & G \\ 0 & 0 \end{bmatrix} \tau} Q e^{\begin{bmatrix} F & G \\ 0 & 0 \end{bmatrix} \tau} d\tau$$

$$\hat{M} = \int_0^{\Delta t} e^{\begin{bmatrix} F & G \\ 0 & 0 \end{bmatrix} \tau} Q \left[ \int_0^{\tau} e^{\begin{bmatrix} F & G \\ 0 & 0 \end{bmatrix} s} ds \right] d\tau \begin{bmatrix} 0 \\ I \end{bmatrix}$$

$$\hat{R} = \Delta t R + \begin{bmatrix} 0 & I \end{bmatrix} \int_0^{\Delta t} \left[ \int_0^{\tau} e^{\begin{bmatrix} F & G \\ 0 & 0 \end{bmatrix} s} ds \right] Q \left[ \int_0^{\tau} e^{\begin{bmatrix} F & G \\ 0 & 0 \end{bmatrix} \tau} d\tau \right] d\tau \begin{bmatrix} 0 \\ I \end{bmatrix}$$

TABLE 2  
SOLUTION OF THE DISCRETE-TIME OPTIMAL CONTROL PROBLEM  
T-2903

DISCRETE-TIME RICCATI EQUATION

$$\Phi_D = \begin{bmatrix} \Phi & \Gamma \\ 0 & I \end{bmatrix} \quad \Gamma_D = \begin{bmatrix} 0 \\ \Delta t I \end{bmatrix}$$

$$P = \Phi_D^T P \Phi_D - (\Gamma_D^T P \Phi_D + \hat{M}^T)^T (\hat{R} + \Gamma_D^T P \Gamma_D)^{-1} (\Gamma_D^T P \Phi_D + \hat{M}^T) + \hat{Q}$$

TYPE 0 DISCRETE-TIME OPTIMAL CONTROL LAW GAINS

$$[K_1 \ K_2] = (\hat{R} + \Gamma_D^T P \Gamma_D)^{-1} (\Gamma_D^T P \Phi_D + \hat{M}^T)$$

TYPE 1 DISCRETE-TIME OPTIMAL CONTROL LAW GAINS

$$[C_1 \ \Delta t C_2] \begin{bmatrix} (\Phi - I) & \Gamma \\ H & D \end{bmatrix} = [\Delta t K_1 \ \Delta t K_2]$$

TYPE 1 CONTROL LAW IN INCREMENTAL FORM

ERROR DYNAMICS:

$$\Delta \underline{u}_k = \Delta \underline{u}_{k-1} - C_1 (\Delta \underline{x}_k - \Delta \underline{x}_{k-1}) - \Delta t C_2 \Delta \underline{y}_{k-1}$$

ORIGINAL VARIABLES:

$$\begin{aligned} \Delta \underline{u}_k = \Delta \underline{u}_{k-1} - C_1 [\Delta \underline{x}_k - \Delta \underline{x}_{k-1}] - \Delta t C_2 \{ \Delta \underline{y}_{k-1} - \Delta \underline{y}_{d,k} \} \\ + [A_{21} + C_1 A_{11}] [\Delta \underline{x}_{m,k} - \Delta \underline{x}_{m,k-1}] \end{aligned}$$

without requiring the nominals if the incremental form discussed in Ref. 11 is used. The total value, zero-order hold, Type 1 control law in incremental form is

$$\underline{u}_k = \underline{u}_{k-1} - C_1 [\underline{x}_k - \underline{x}_{k-1}] - \Delta t C_2 [\underline{y}_{k-1} - \underline{y}_{d,k}] \quad (1)$$

In Eq. 1,  $\underline{u}_k$  is the  $(m \times 1)$  control command vector which is sent to the control actuators at time  $t_k$ ,  $\underline{x}_k$  is the measured or

estimated value of the  $(n \times 1)$  aircraft state vector in body axes used for feedback at time  $t_k$ ,  $y_{k-1}$  is the  $(\ell \times 1)$  measured or estimated value of the output vector at time  $t_{k-1}$  which is to match the pilot commands, and  $y_{d,k}$  is the  $(\ell \times 1)$  pilot command vector at time  $t_k$ . For simplicity all states are assumed measured and no estimation techniques are employed. Detailed estimation techniques are discussed in Ref. 7.

Equation 1 is the Type 1 control law simulated in Chapter 3 with the feedback gain  $C_1$  and the integrator gain  $C_2$  scheduled with flight condition. The prime on  $u'_{k-1}$  in Eq. 1 indicates the control command is reset always to lie within the control actuator range during control saturation and to prevent windup as discussed in Ref. 11. In the nonlinear simulations in Chapter 3, maneuvers are performed which require maximum performance from the aircraft and which briefly saturate some of the controls in  $u_k$ .

The Type 1 control law eliminates the need for computing nominal values by taking advantage of the integral property. The Type 0 control law does not have this property and depends on knowledge of the nominal. The total value Type 0 control law is as follows using Ref. 7,

$$u_k = u'_{k-1} - \Delta t K_1 [x_{k-1} - x_k^*] - \Delta t K_2 [u_{k-1} - u_k^*] \quad (2)$$

$$x_k^* = x_{o,k} + \Omega_{12} (y_{d,k} - y_{o,k}) \quad (3)$$

$$u_k^* = u_{o,k} + \Omega_{22} (y_{d,k} - y_{o,k}) \quad (4)$$

The states  $x_k^*$  and  $u_k^*$  in Eqs. 3 and 4 are estimates of the current nominal states and controls of the aircraft based on perturbations from some fixed nominal. The states  $x_o$ ,  $u_o$ , and  $y_o$  are the fixed nominal of the aircraft. Periodically,

if the pilot command,  $y_{d,k}$ , is significantly different from the fixed nominal command  $y_{o,k-1}$ , then  $x_{o,k}$ ,  $u_{o,k}$ , and  $y_{o,k}$  must be updated as the aircraft transitions between flight conditions. Numerous procedures exist for determining the fixed nominal values in flight, including trim maps, scheduling, or updating  $x_o$ ,  $u_o$  and  $y_o$  using low-pass filtered versions of  $x$ ,  $u$ , and  $y$ .

In Eq. 2,  $K_1$  is the state feedback gain and the gain  $K_2$  causes the low-pass filter action of the Type 0 control law. The matrices  $\Omega_{12}$  and  $\Omega_{22}$  are the steady state feedforward gains (Ref. 12) and are obtained from the following equations

$$\begin{bmatrix} (\phi - I) & \Gamma \\ H & D \end{bmatrix} \begin{bmatrix} \Delta x^* \\ \Delta u^* \end{bmatrix} = \begin{bmatrix} 0 \\ \Delta y_d \end{bmatrix} \quad (5)$$

$$\begin{bmatrix} (\phi - I) & \Gamma \\ H & D \end{bmatrix}^R = \begin{bmatrix} \Omega_{11} & \Omega_{12} \\ \Omega_{21} & \Omega_{22} \end{bmatrix} \quad (6)$$

$$\begin{bmatrix} \Delta x^* \\ \Delta u^* \end{bmatrix} = \begin{bmatrix} \Omega_{12} & \Delta y_d \\ \Omega_{22} & \Delta y_d \end{bmatrix} \quad (7)$$

The matrices  $\phi$  and  $\Gamma$  are the discrete equivalents of the linearized aircraft model matrices,  $F$  and  $G$ , as shown in Table 1. The matrices  $H$  and  $D$  transform the aircraft states and controls to the commanded output,  $\Delta y$ , as follows

$$\Delta y = H \Delta x + D \Delta u$$

The vectors  $\Delta x^*$  and  $\Delta u^*$  are the nominal perturbations which must be added to current nominal states and controls of the aircraft,  $x_o$  and  $u_o$  when a perturbation in the command vector,  $\Delta y_d$ , is requested by the pilot.

In Eq. 6, superscript R denotes the right inverse. The right inverse solves Eq. 5 when the number of commands,  $\ell$ , is less than the number of controls  $m$ . The right inverse used in this report is computed using the weighted pseudoinverse,

$$\begin{bmatrix} (\Phi-I) & \Gamma \\ H & D \end{bmatrix}^R = Q_s^{-1} \begin{bmatrix} (\Phi-I) & \Gamma \\ H & D \end{bmatrix}^T \left( \begin{bmatrix} (\Phi-I) & \Gamma \\ H & D \end{bmatrix} Q_s^{-1} \begin{bmatrix} (\Phi-I) & \Gamma \\ H & D \end{bmatrix}^T \right)^{-1} \quad (8)$$

Singular value decomposition is used in the computations in Eq. 8 for improved numerical accuracy. Section 2.2 discusses values chosen for the pseudoinverse weighting matrix,  $Q_s$  used in Eq. 8.

The Type 0 gains are related to the Type 1 gains as shown in Table 2.  $K_1$  and  $K_2$  are determined from a Riccati equation solution and  $C_1$  and  $C_2$  are computed as follows:

$$\begin{bmatrix} C_1 & \Delta t C_2 \end{bmatrix} = \begin{bmatrix} \Delta t K_1 & \Delta t K_2 \end{bmatrix} \begin{bmatrix} (\Phi-I) & \Gamma \\ H & D \end{bmatrix}^R \quad (9)$$

The values for  $Q_s$  used to obtain  $\Omega_{12}$  and  $\Omega_{22}$  do not have to be the same as the values in  $Q_s$  used to obtain  $C_1$  and  $C_2$  in Eq. 9. The design in this report uses different values for  $Q_s$  in Eq. 6 and Eq. 9 for reasons discussed in the following sections.

There are usually an infinite number of solutions to Eq. 5 when  $\ell < m$ ; the pseudoinverse shown in Eq. 9 represents the weighted least squares solution. If Eq. 7 is substituted into Eq. 5 the equality is true but if Eq. 9 is substituted for  $C_1$  and  $C_2$  in the equation in Table 2, equality usually

does not hold for  $l < m$ . If the number of controls equals the number of commands then equality holds in Eq. 5 and in Table 2. In the aircraft control design in this report, the number of commands,  $l$ , is less than the number of controls,  $m$ . References 2 and 3 are earlier continuous-time discussions of the command/control requirements for the digital ACM controller used here and these references describe reasons why treating all aircraft controls independently is a desirable feature. These reasons are as follows:

- By varying the weights in  $Q_s$  in Eq. 8 it is possible to decrease control steady-state positions while increasing aircraft final state values. The result is to increase the range of the aircraft states that can be commanded as discussed in Section 2.2.
- For maximum performance maneuvers it is possible to favorably saturate one control while leaving the other aircraft controls operational. The result is to increase performance without causing aircraft departures and is demonstrated in Chapter 3.
- When the number of commands and controls are equal, the aircraft develops a finite set of transmission zeroes (Ref. 13) which play an important part in tracking theory (Refs. 14 and 12). These transmission zeroes cannot be changed by state feedback. Degraded handling qualities occur if any transmission zeroes are in the right-half complex plane (i.e., non-minimum phase). When the number of controls is greater than the number of commands, the plant still has zeroes but they can be changed by adjusting  $Q_s$  in Eq. 8. In particular, right-half plane zeroes can be favorably moved into the left-half (minimum phase) complex plane as discussed in Section 2.4.

- If the number of commands is less than number of the controls, the number of closed-loop modes that must be stabilized is reduced when converting from the Type 0 to the Type 1 control law. Extra design freedom exists because some of the closed-loop modes shift during the transformation if  $Q_s$  in Eq. 8 is changed. If  $Q_s$  is chosen appropriately the shifts are all favorable as discussed in Section 2.4.

The Type 0 controller shown in Eqs. 2 through 4 is considerably more complex to implement than the Type 1 controller in Eq. 1. Other disadvantages of the Type 0 controller are discussed in the following sections.

## 2.2 PSEUDOINVERSE WEIGHTING MATRIX FOR FIGHTER AIRCRAFT APPLICATIONS

This section presents the design of the pseudoinverse weighting matrix,  $Q_s$ , used in Eq. 8 for specification of the Type 0 DFCS feedforward matrices. Unity weighting is used for the continuous-time Type 0 design in Ref. 3 and it will be shown that this is not necessarily the best choice.

The states, controls, and commands for the aircraft are

$$\Delta \underline{x}^T = [\Delta q \ \Delta w \ \Delta v \ \Delta r \ \Delta p]$$

$$\Delta \underline{u}^T = [\delta_s \ \delta_{mf} \ \delta_{sp} \ \delta_{ds} \ \delta_r]$$

$$\Delta \underline{y}_d^T = [\Delta a_n \ \Delta \beta \ \Delta p_w]$$

Three inputs, normal acceleration,  $\Delta a_n$ , sideslip,  $\Delta \beta$ , and wind axis roll rate,  $\Delta p_w$ , are to command five controls: stabilator,



$\Delta\delta_s$ , main flaps,  $\Delta\delta_{mf}$ , spoilers,  $\Delta\delta_{sp}$ , differential stabilizers,  $\Delta\delta_{ds}$  and rudder,  $\Delta\delta_r$ . The DFCS design is nearly the same as in Ref. 3, except it is to be done in discrete time, and, for reasons discussed in the next paragraph,  $\Delta u$  is not included in the state vector.

The state  $\Delta u$  is dropped from the control design state vector because the discrete and continuous time Type 0 DFCS designs yield a very poor  $\Delta a_n$  step response with  $\Delta u$  included. The Type 0 DFCS at design point 2 in Ref. 3, Table 14, has a closed-loop eigenvalue with a time constant of 19.3 sec. This slow time constant disappears from the Type 1 eigenvalues as shown in Ref. 3. The slow closed-loop eigenvalue is one half of a phugoid complex pair and the eigenvector has a large  $\Delta u$  contribution (Ref. 3, Table 15). The slow eigenvalue is removed from the Type 1 eigenvalues by using very large gains on  $\Delta u$  (Ref. 3, Figs. 56 and 58). When the Type 0  $\Delta a_n$  step response is simulated, there is a contribution to  $\Delta a_n$  from the change in  $\Delta u$  in the  $H\Delta x + D\Delta u$  observation vector. Since the Type 0  $\Delta u$  response has a 19.3 sec time constant, the Type 0  $\Delta a_n$  response also contains the slow response. It is intriguing that the Type 0 to Type 1 transformation automatically compensated for the poor  $\Delta u$  response and indicated superior  $\Delta a_n$  command simulations. The Type 0  $\Delta a_n$  response was not attempted in Ref. 3 and the  $\Delta u$  problem was not identified until the digital Type 0 DFCS was simulated. When  $\Delta u$  is removed from the state vector, the speed response of the aircraft becomes open loop subject to any throttle activity of the pilot. (In ACM the pilot usually uses full throttle.) Within the time frame of interest for a  $\Delta a_n$  step response the open-loop,  $\Delta u$  response is close to zero and does not have a significant effect on performance.

The purpose of the pseudoinverse weighting matrix,  $Q_s$ , in Eq. 8 is to trade off steady state values of the aircraft states against steady state values of aircraft control position needed to satisfy the command requirements. If more weight is placed on the controls in  $Q_s$ , the effect is to increase the values of the states that are not commanded by  $\Delta y_d$  while at the same time decreasing the values of the controls needed to meet the command requirements. The net result is to increase the effective operating range of the aircraft states before control saturation is encountered, a very desirable situation.

A pseudoinverse weighting matrix which has the desired weighting pattern uses unity weighting for velocity states,  $v$  and  $w$ , in fps, unity weighting for angular rates,  $p$ ,  $q$ , and  $r$  in degrees, and a multiple of the inverse of the total amount of individual control travel for the control position weights.

$$Q_s = \begin{bmatrix} 1 & & & & 0 \\ & \ddots & & & \\ & & 1_n & & \\ & & & \frac{a}{\Delta \delta_{1_{\max}}} & \\ & & & & \ddots \\ 0 & & & & & \frac{a}{\Delta \delta_{m_{\max}}} \end{bmatrix} \quad (10)$$

The control weighting pattern causes controls with the least amount of travel to have the most weight. Table 3 shows the changes in the elements in  $\Omega_{22}$  and  $\Omega_{12}$  caused by changing the value of  $a$  in Eq. 10 between 1 and 2000.

TABLE 3  
EFFECTS OF CHANGING THE PSEUDOINVERSE WEIGHTING MATRIX  
ON QUAD PARTITION INVERSE ELEMENTS

T-1794

$\Omega_{22}$ or $\Omega_{12}$ ELEMENT	UNITS	INVERSE*	PSEUDOINVERSE-CONTROL WEIGHTS				
		UNITY	$\frac{2}{\text{MAX}}$	UNITY	$\frac{20}{\text{MAX}}$	$\frac{200}{\text{MAX}}$	$\frac{2000}{\text{MAX}}$
$\Delta \delta_s / \Delta a_{nc}$	deg/fps <sup>2</sup>	-0.118	-0.375	-0.321	-0.253	-0.118	-0.0659
$\Delta \delta_{mf} / \Delta a_{nc}$	deg/fps <sup>2</sup>	-	0.703	0.557	0.369	0.005	-0.141
$\Delta \delta_{sp} / \Delta \beta_c$	deg/deg	-	-1.06	-0.226	-0.982	-0.982	-0.981
$\Delta \delta_{ds} / \Delta \beta_c$	deg/deg	-1.22	-1.04	-1.18	-1.05	-1.05	-1.05
$\Delta \delta_x / \Delta \beta_c$	deg/deg	1.11	1.10	1.11	1.10	1.10	1.10
$\Delta \delta_{sp} / \Delta p_{wc}$	deg/deg/sec	-	-0.117	-0.0252	-0.116	-0.116	-0.116
$\Delta \delta_{ds} / \Delta p_{wc}$	deg/deg/sec	-0.150	-0.129	-0.145	-0.129	-0.129	-0.129
$\Delta \delta_x / \Delta p_{wc}$	deg/deg/sec	-0.00174	-0.00339	-0.00209	-0.00338	-0.00338	-0.00339
$\Delta q / \Delta a_{nc}$	deg/deg/fps <sup>2</sup>	0.0976	0.0963	0.0966	0.0969	0.0976	0.0979
$\Delta w / \Delta a_{nc}$	fps/fps <sup>2</sup>	1.49	0.0135	0.321	0.714	1.48	1.79
$\Delta v / \Delta p_{wc}$	fps/deg/sec	0.0	0.0	0.0	0.0	0.0	0.0
$\Delta x / \Delta p_{wc}$	deg/sec/deg/sec	0.169	0.169	0.169	0.169	0.169	0.169
$\Delta p / \Delta p_{wc}$	deg/sec/deg/sec	0.986	0.986	0.986	0.986	0.986	0.986
$\Delta v / \Delta \beta_c$	fps/deg	10.47	10.47	10.47	10.47	10.47	10.47
$\Delta x / \Delta \beta_c$	deg/sec/deg	-0.0684	-0.0664	-0.0679	-0.0666	-0.0666	-0.0665
$\Delta p / \Delta \beta_c$	deg/sec/deg	0.100	0.100	0.100	0.100	0.100	0.0984

\* $\Delta \delta_{mf}$  and  $\Delta \delta_{sp}$  are removed from the controls to construct the inverse.

The flight condition used in Table 3 is trimmed straight flight with a forward velocity, pitch rate and angle of attack of 183 m/s (600 fps), 5 deg/sec, and 10 deg, respectively, (design point 1 in Ref. 2). Three important observations can be made: 1) lateral states and control positions change little with increasing pseudoinverse control weights, 2) the longitudinal states trade off  $\Delta w$  with control position, and 3) considerable deviations in the maneuver flap steady state value can occur even though maneuver flap has the least amount of control travel before saturation (10 deg).

The above observations lead to the conclusion that the weighting matrix should be chosen based on the relationship between stabilator and maneuver flap. Figure 2 shows  $\Delta\delta_s/\Delta a_{nc}$  and  $\Delta\delta_{mf}/\Delta a_{nc}$  variations at 183 m/s (600 fps) with increasing angle of attack and pitch rate flight conditions. Below 20 deg  $\alpha_o$ ,  $\Delta\delta_{mf}$  has a small contribution in aiding  $\Delta\delta_s$ , but beyond 20 deg  $\alpha_o$ ,  $\Delta\delta_{mf}$  significantly increases the effective operating range of the aircraft to higher angles of attack before  $\Delta\delta_s$  saturates. The weighting parameter 100/MAX (2.5, 10, 1.85, 4.16, 1.66 along the control diagonal in  $Q_s$ ) produces the desired result. It provides a ratio below  $\frac{1}{2}$  for  $\Delta\delta_{mf}/\Delta\delta_s$  when  $\alpha_o$  is less than 20 deg. Above 27 deg  $\alpha_o$  100/MAX weighting causes  $\Delta\delta_{mf}$  to saturate favorably in order to satisfy an increase of  $9.8 \text{ m/s}^2$  (1g)  $\Delta a_n$  command.

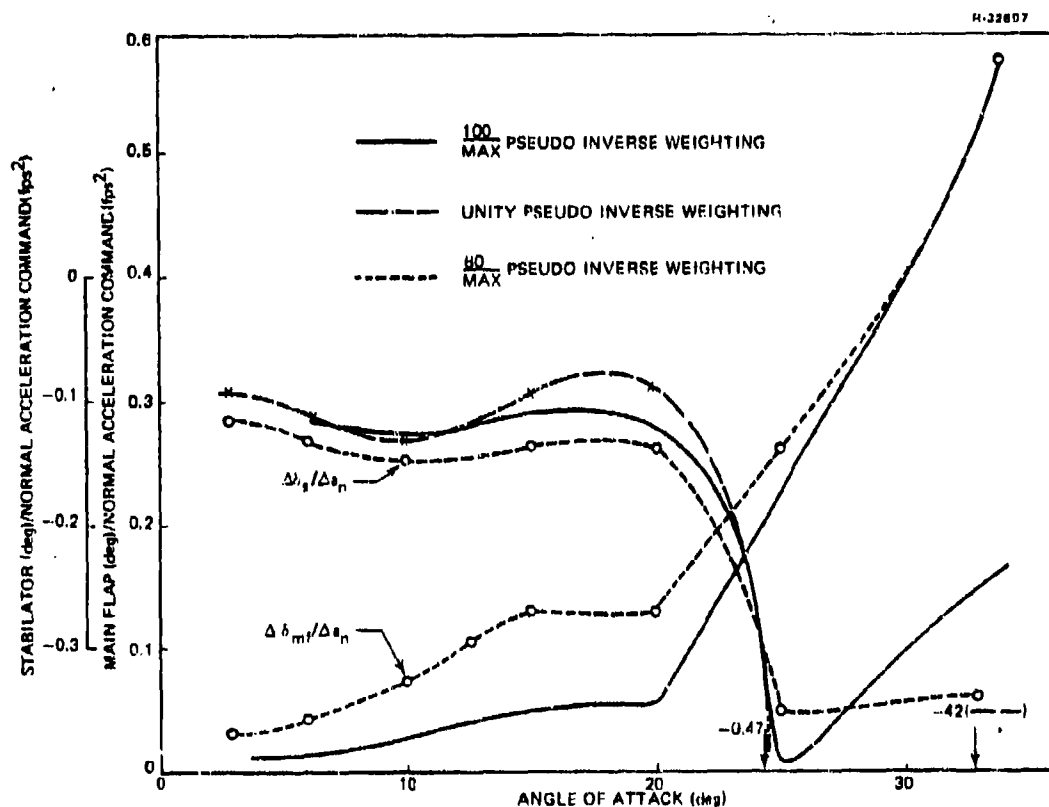


Figure 2 Effects of Changing Flight Condition on Quad Partition Inverse Elements

### 2.3 SYNTHESIS OF CONTROLLERS USING CONTINUOUS-TIME SPECIFICATIONS

This section presents the synthesis of the Type 0 and Type 1 digital control law design at one flight condition. One design approach for digital flight control systems is to design an analog system and then discretize it. The result often leads to a high sample rate system which places significant requirements on the flight computer used to implement the design. One reason this practice continues is that a large body of information and experience exists for continuous-time designs including MIL-F-8785B (Ref. 15). The continuous-time design in Ref. 3 could have been emulated digitally to produce a discrete-time controller.

Examples of analog designs implemented digitally using the Tustin approximation are shown in Ref. 16 for the space shuttle (25 Hz and 12.5 Hz sampling time) and in Ref. 17 for a fighter aircraft (80 Hz and 40 Hz sampling time). It is clear, however, that improved performance and reduced computer requirements can be obtained using a direct digital design at lower sampling rates which take better advantage of digital system characteristics.

The approach used in this section to obtain a direct digital design which at the same time retains continuous-time features is the sampled-data regulator discussed in Ref. 18. The sampled-data regulator transforms a continuous-time system and cost function to their equivalent discrete-time representation as shown in Table 1. The discrete-time design gives a stable discrete-time closed-loop system with eigenvalues inside

the unit circle. This section shows that transforming the closed-loop discrete-time system back to continuous-time gives an equivalent closed-loop continuous-time system that can be used to evaluate the digital design using continuous-time specifications. Also shown are the cost function weighting elements and the flight conditions used for point design. In point design, which is the basis for all the designs discussed in Ref. 1 to 7, a number of linear time-invariant aircraft models are determined at a set of trimmed flight conditions which span the flight regime of interest. The control law gains are found at each flight condition. The gains are regressed against a set of nonlinear functions of the major flight variables and the resulting gain schedules are suitable for onboard implementation.

The flight conditions used for point design span a large range of trimmed values of velocity, angle of attack, and roll rate about the velocity vector. Thirty flight conditions are used with velocity either 122, 183, or 244 m/s, wind-axis roll rate either 0, 50, or 100 deg/sec, and angle of attack varying between 0 and 33 deg. Nonzero sideslip conditions are not included since sideslip is usually commanded to be zero. Figure 3 shows the flight conditions in a three dimensional configuration.

The sampling rate for the DFCS is chosen to be 20 samples/sec. Results in Ref. 19 and 20 indicate that a direct digital design can go as low as 10 samples/sec and still provide adequate performance with unmodeled body bending modes and turbulence in the loop. The higher sampling rate in the DFCS serves to reduce pilot awareness of the control surface steps and to keep the control surface phase lag from exceeding 30 deg (Ref. 15).

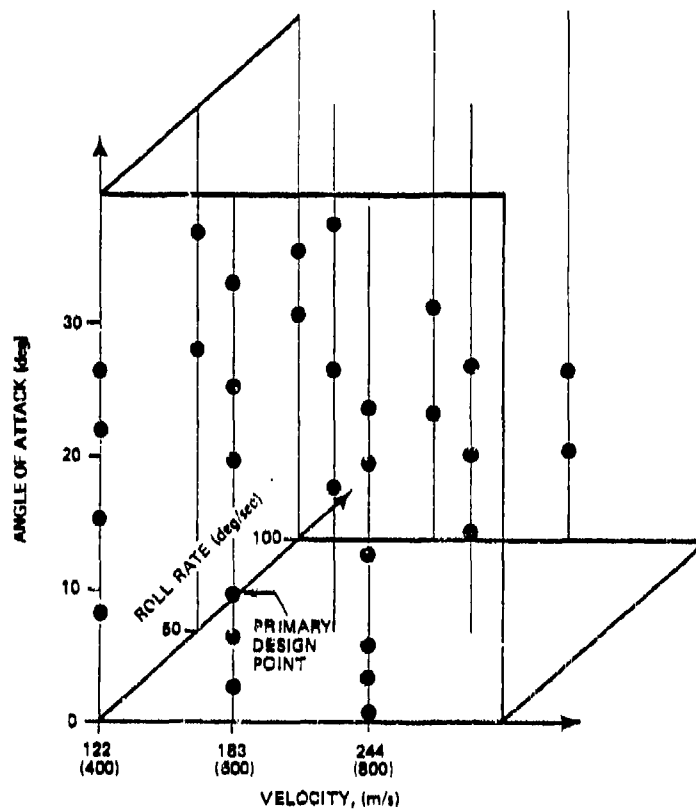


Figure 3 Flight Conditions for DFCS Point Design

At each flight condition, closed-loop eigenvalues and step-response simulation (i.e., the eigenvectors) of the linearized system are used to evaluate the design. Closed-loop eigenvalues should meet the requirements in MIL-F-8785B for Category A, Level 1 flight of a Class IV aircraft. Step response transients should fall within envelopes which are known to generate good pilot ratings as shown in Refs. 10 and 17. The closed-loop system for the Type 0 DFCS is

$$\begin{bmatrix} \Delta \underline{x} \\ \Delta \underline{u} \end{bmatrix}_{k+1} = \begin{bmatrix} \Phi & \Gamma \\ -\Delta t K_1 & -\Delta t K_2 \end{bmatrix} \begin{bmatrix} \Delta \underline{x} \\ \Delta \underline{u} \end{bmatrix}_k + \begin{bmatrix} 0 \\ (\Delta t K_1 \Omega_{12} + \Delta t K_2 \Omega_{22}) \Delta \underline{y}_d \end{bmatrix} \quad (11)$$

while the closed-loop system for the Type 1 DFCS in position form using perturbation variables and an integrator state,  $\Delta\xi$ , is

$$\begin{bmatrix} \Delta\mathbf{x} \\ \Delta\xi \end{bmatrix}_{k+1} = \begin{bmatrix} \Phi - \Gamma C_1 & -\Gamma C_2 \\ \Delta t H - \Delta t D C_1 & I - \Delta t D C_2 \end{bmatrix} \begin{bmatrix} \Delta\mathbf{x} \\ \Delta\xi \end{bmatrix}_k + \begin{bmatrix} 0 \\ -\Delta t \Delta y_{d,k+1} \end{bmatrix} \quad (12)$$

If the number of commands and controls are equal, the eigenvalues of the two closed-loop systems are equal and the feed-forward gains are unique. If the number of commands is less than the number of controls (the situation for the design here) then the eigenvalues between the two differently dimensioned closed-loop-systems cannot be all equal but are closely aligned depending on the weighting matrix in the pseudoinverse identified in Eq. 9. For reasons which are discussed in the next section, unity weighting ( $Q_s = I$ ) is used in Eq. 9.

The closed-loop eigenvalues and eigenvectors are adjusted by iterating on Q and R, the quadratic cost function weights. Although emulating the continuous-time design in Ref. 3 is considered a poor practice, the continuous-time cost function weighting elements can be used directly in the sampled-data regulator digital design. Continued refinement of performance, however, caused the choice of Q and R to differ from those in Ref. 3. The change in the cost function weighting elements is shown in Table 4. The primary changes are a decrease in  $\Delta w$ ,  $\Delta a_n$  and  $\Delta v$  weighting, and an increase in  $\Delta p_w$  and control position weighting. The effect on the closed-loop system is to decrease the short period natural frequency and the stability-axis roll rate rise time, while increasing the normal acceleration and sideslip rise times. These effects improve the command performance.



TABLE 4  
DFCS WEIGHTS AT DESIGN POINT 1

T-3117

MATRIX	MATRIX TYPE	MATRIX ELEMENT	MAXIMUM MEAN VALUE IN REF. 2	MAXIMUM MEAN VALUE HERE
Q	State Position	Axial Velocity, $\Delta u$	12.2 m/s (40 fps)	Not used
		Lateral Velocity, $\Delta v$	3.05 m/s (10 fps)	6.1 m/s (20 fps)
		Normal Velocity, $\Delta w$	3.66 m/s (12 fps)	7.6 m/s (25 fps)
		Body Angular Rates	20 deg/sec	20 deg/sec
Q	State Rate	Lateral Acceleration, $\Delta \dot{v}$	3.66 m/s <sup>2</sup> (12 fps <sup>2</sup> )	3.0 m/s <sup>2</sup> (10 fps <sup>2</sup> )
		Normal Acceleration, $\Delta \dot{w}$	1.53 m/s <sup>2</sup> (5 fps <sup>2</sup> )	6.1 m/s <sup>2</sup> (20 fps <sup>2</sup> )
Q	Pilot Command	Stability-Axis Normal Acceleration Command, $\Delta a_n$	0.533 m/s <sup>2</sup> (1.75 fps <sup>2</sup> )	0.92 m/s <sup>2</sup> (3.0 fps <sup>2</sup> )
		Sideslip	Sideslip Command, $\beta_s$	0.9 deg
		Stability-Axis Roll Rate Command, $\Delta p_w$	2.5 deg/sec	2.0 deg/sec
Q	Control Position	Stabilator Deflection, $\Delta \delta_s$	10 deg	5 deg
		Maneuver Flap Deflection, $\Delta \delta_{mf}$	5 deg	1.25 deg
		Spoiler Deflection, $\Delta \delta_{ds}$	27 deg	3.375 deg
		Differential Stabilator Deflection, $\Delta \delta_{ds}$	6 deg	3.0 deg
		Rudder Deflection, $\Delta \delta_r$	15 deg	7.5 deg
R	Control Rate	Stabilator Rate, $\Delta \dot{\delta}_s$	3 deg/sec	3 deg/sec
		Maneuver Flap Rate, $\Delta \dot{\delta}_{mf}$	4 deg/sec	4 deg/sec
		Spoiler Rate, $\Delta \dot{\delta}_{sp}$	4 deg/sec	4 deg/sec
		Differential Stabilator Rate, $\Delta \dot{\delta}_{ds}$	3 deg/sec	3 deg/sec
		Rudder Rate, $\Delta \dot{\delta}_r$	4 deg/sec	4 deg/sec

The closed-loop eigenvalues for the DFCS using Eqs. 11 and 12 all fall within the unit circle. It is reasonable to presume that if the continuous plant is converted to an equivalent discrete system using a matrix exponential in Table 1, then a discrete system can be converted to an equivalent continuous system using the natural logarithm of a matrix. If  $\Phi_{CL}$  is either of the closed-loop system matrices in Eqs. 11 and 12, then

$$F_{CL} = \frac{1}{\Delta t} \ln \Phi_{CL} = \frac{1}{\Delta t} \left[ (\Phi_{CL} - I) - \frac{1}{2} (\Phi_{CL} - I)^2 + \frac{1}{3} (\Phi_{CL} - I)^3 - \dots \right]$$

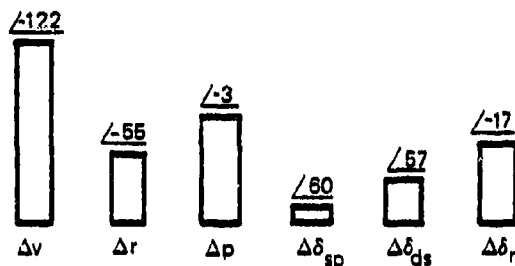
is the equivalent continuous system. The sequence for the logarithm of a matrix converges if the eigenvalues of  $\Phi_{CL}$  are in the open right half complex plane and the magnitude of the eigenvalues are less than or equal to two.

At the nominal design flight conditions ( $V = 183$  m/s (600 fps),  $\alpha = 9$  deg,  $p_w = 0$ ), Table 5 shows a comparison between eigenvalues of the different closed-loop systems in Eqs. 11 and 12 for the same Q and R. The continuous-time closed-loop eigenvalues determined by minimizing the continuous-time cost function in Table 1 and the mapped discrete-time eigenvalues are almost identical. Furthermore, changing the sampling time to a larger but not unreasonable sampling time has little effect on the mapped eigenvalue locations, particularly in the Type 0 system which does not involve using the pseudoinverse to compute the feedback gains. A comparison between Dutch roll mode eigenvectors in Figure 4 shows the eigenvectors are also almost identical. It is concluded that evaluating the digital design using the mapped eigenvalues is a useful procedure for evaluating a digital system's performance using continuous-time specifications.

TABLE 5  
COMPARISON BETWEEN CONTINUOUS-TIME AND MAPPED  
DISCRETE-TIME CLOSED-LOOP SYSTEM EIGENVALUES

T-3118

DYNAMIC MODE	CLOSED-LOOP CHARACTERISTICS CONTINUOUS DISCRETE TIME TYPE 0			UNITY PSEUDOINVERSE WEIGHTING CLOSED-LOOP CHARACTERISTICS CONTINUOUS DISCRETE TIME TYPE 1		
	Natural Frequency, Rad/Sec	Damping Ratio	Time Constant, Sec	Natural Frequency, Rad/Sec	Damping Ratio	Time Constant Sec
Short Period	4.19	0.662	--	5.32	0.735	--
Roll Command	4.34	0.686	--	4.34	0.686	--
Dutch Roll	3.46	0.658	--	3.46	0.658	--
Normal Acceleration Command	--	--	0.320	--	--	0.363
Longitudinal Control	--	--	0.400	--	--	--
Lateral Control	--	--	0.849	--	--	--
Sideslip Command	--	--	0.975	--	--	0.974
SAMPLING TIME = 0.05 sec						
DYNAMIC MODE	CLOSED-LOOP CHARACTERISTICS DISCRETE TIME TYPE 0			UNITY PSEUDOINVERSE WEIGHTING CLOSED-LOOP CHARACTERISTICS DISCRETE TIME TYPE 1		
	Natural Frequency, Rad/Sec	Damping Ratio	Time Constant, Sec	Natural Frequency, Rad/Sec	Damping Ratio	Time Constant Sec
Short Period	4.21	0.665	--	5.54	0.715	--
Roll Command	4.34	0.682	--	4.34	0.682	--
Dutch Roll	3.46	0.656	--	3.46	0.655	--
Normal Acceleration Command	--	--	0.322	--	--	0.368
Longitudinal Control	--	--	0.400	--	--	--
Lateral Control	--	--	0.849	--	--	--
Sideslip Command	--	--	0.978	--	--	0.977
SAMPLING TIME = 0.1 sec.						
DYNAMIC MODE	CLOSED-LOOP CHARACTERISTICS DISCRETE TIME TYPE 0			UNITY PSEUDOINVERSE WEIGHTING CLOSED-LOOP CHARACTERISTICS DISCRETE TIME TYPE 1		
	Natural Frequency, Rad/Sec	Damping Ratio	Time Constant, Sec	Natural Frequency, Rad/Sec	Damping Ratio	Time Constant Sec
Short Period	4.24	0.666	--	5.75	0.684	--
Roll Command	4.34	0.671	--	4.34	0.671	--
Dutch Roll	3.46	0.653	--	3.46	0.653	--
Normal Acceleration Command	--	--	0.324	--	--	0.371
Longitudinal Control	--	--	0.402	--	--	--
Lateral Control	--	--	0.848	--	--	--
Sideslip Command	--	--	0.984	--	--	0.983



CLOSED-LOOP CONTINUOUS TIME TYPE O

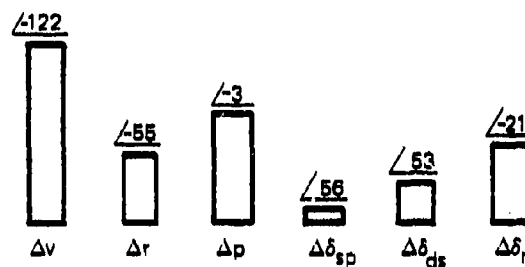
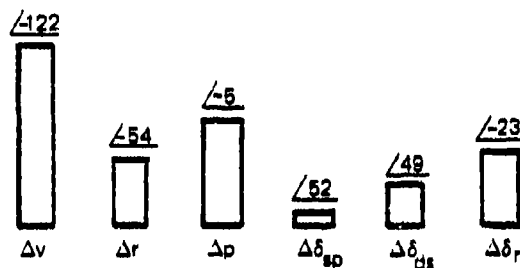
CLOSED-LOOP DISCRETE-TIME TYPE O,  $\Delta t = 0.05$  SECCLOSED-LOOP DISCRETE-TIME O,  $\Delta t = 0.1$  SEC

Figure 4 Comparison Between Continuous-Time and Mapped Discrete-Time Closed-Loop System Eigenvectors for the Dutch Roll Mode

Using MIL-F-8785B the desirable range of short period natural mode frequency at the nominal flight conditions under discussion is 0.9 rad/sec to 6.8 rad/sec with a damping ratio between 0.35 and 1.3. Minimum Dutch roll natural frequency,  $\omega_{nd}$ , and damping ratio,  $\xi_d$ , requirements are 0.19 for  $\xi_d$ , 0.35 for  $\xi_d \omega_{nd}$ , and 1.0 rad/sec for  $\omega_{nd}$ . The roll mode time constant should be less than 1.0 sec. All of these requirements are met by the mapped eigenvalues of the DFCS at the nominal flight condition as shown in Table 5.

#### 2.4 COMPARISON OF DISCRETE DFCS TYPE 0 AND TYPE 1 RESPONSE

Type 0 and Type 1 discrete DFCS design step responses are presented in this section. The flight condition for the reference aircraft is the same as the one used for eigenvalue analysis in Section 2.3. The discrete state time histories are interpolated to provide the approximate continuous-time simulation. The discrete control time histories are stair-cased in the figures and indicate the step commands the reference aircraft actuators receive from the control law. The control laws are simulated using the incremental form shown in Eqs. 1 and 2.

Experiments with large pseudoinverse weighting elements for the states in going from the Type 0 to the Type 1 DFCS have shown significant and in some cases unstable eigenvalues changes. Care must be taken in using non-unity pseudoinverse weighting matrices when transforming from the Type 0 to the Type 1 control design. Keep in mind that the pseudoinverse used in Eq. 6 to find  $\Omega_{12}$  and  $\Omega_{22}$  and the pseudoinverse used in Eq. 9 to find  $C_1$  and  $C_2$  are similar but have completely different effects on the control law. The former affects steady state conditions while the latter affects closed-loop eigenvalues.

To compare the effect of eigenvalue and step response changes caused by the pseudoinverse weighting matrix, three cases are considered. In all three cases the weighting on the states is unity while the control weightings are unity, 100/MAX (2.5, 10.0, 1.85, 4.16, 1.66), and 1000/MAX (25.0, 100.0, 18.5, 41.6, 16.6). The resulting steady state control positions are

$$\begin{bmatrix} \Delta\delta_s^* \\ \Delta\delta_{mf}^* \\ \Delta\delta_{sp}^* \\ \Delta\delta_{ds}^* \\ \Delta\delta_r^* \end{bmatrix} = \begin{bmatrix} -0.321 & 0.0 & 0.0 \\ 0.557 & 0.0 & 0.0 \\ 0.0 & -0.226 & -0.0258 \\ 0.0 & -1.18 & -0.145 \\ 0.0 & 1.11 & -0.00209 \end{bmatrix} \begin{bmatrix} \Delta a_{nc} \\ \Delta\beta_c \\ \Delta p_{wc} \end{bmatrix} \quad (13)$$

for unity weighting,

$$\begin{bmatrix} \Delta\delta_s^* \\ \Delta\delta_{mf}^* \\ \Delta\delta_{sp}^* \\ \Delta\delta_{ds}^* \\ \Delta\delta_r^* \end{bmatrix} = \begin{bmatrix} -0.127 & 0.0 & 0.0 \\ 0.0272 & 0.0 & 0.0 \\ 0.0 & -0.960 & -0.116 \\ 0.0 & -1.052 & -0.129 \\ 0.0 & 1.10 & -0.00338 \end{bmatrix} \begin{bmatrix} \Delta a_{nc} \\ \Delta\beta_c \\ \Delta p_{wc} \end{bmatrix} \quad (14)$$

for 100/MAX control weighting and

$$\begin{bmatrix} \Delta\delta_s^* \\ \Delta\delta_{mf}^* \\ \Delta\delta_{sp}^* \\ \Delta\delta_{ds}^* \\ \Delta\delta_r^* \end{bmatrix} = \begin{bmatrix} -0.117 & 0.0 & 0.0 \\ 0.00236 & 0.0 & 0.0 \\ 0.0 & -0.960 & -0.116 \\ 0.0 & -1.052 & -0.129 \\ 0.0 & 1.10 & -0.00338 \end{bmatrix} \begin{bmatrix} \Delta a_{nc} \\ \Delta\beta_c \\ \Delta p_{wc} \end{bmatrix} \quad (15)$$

for 1000/MAX control weighting. The primary effect is to decrease the main flaps steady state position and to increase the spoiler steady state position.

The effect of increasing the control position weighting in the pseudoinverse matrix on the closed-loop Type 1 mapped discrete eigenvalues is shown in Table 6. The only significant effect occurs in the longitudinal dynamics where the short period natural frequency and damping ratio decrease to smaller but acceptable values.

TABLE 6  
COMPARISON OF TYPE 1 DISCRETE CLOSED-LOOP  
EIGENVALUES AT DESIGN POINT 1 FOR DIFFERENT  
PSEUDOINVERSE WEIGHTING MATRICES

T-1933

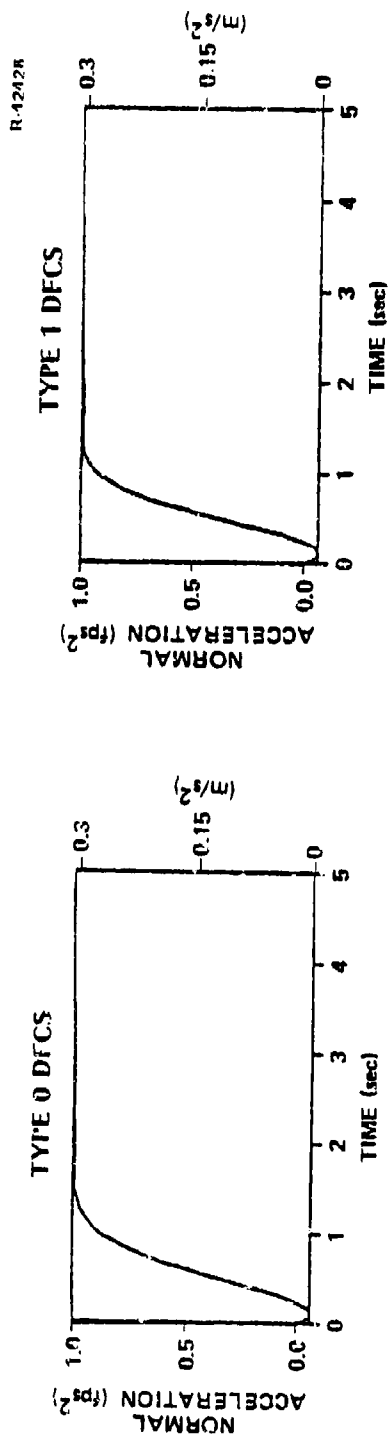
PSEUDOINVERSE WEIGHTING MATRIX	SHORT PERIOD	DUTCH ROLL	ROLL COMMAND	NORMAL ACCELER- ATION COMMAND	SIDESLIP COMMAND
Unity for States and Controls					
Natural Frequency, Rad/Sec	5.54	3.46	4.34	—	—
Damping Ratio	0.715	0.656	0.682	—	—
Time Constant, Sec	—	—	—	0.368	0.977
Unity for States 100/MAX for Controls					
Natural Frequency, Rad/Sec	4.59	3.46	4.34	—	—
Damping Ratio	0.591	0.655	0.683	—	—
Time Constant, Sec	—	—	—	0.384	0.977
Unity for States 1000/MAX for Controls					
Natural Frequency, Rad/Sec	4.53	3.46	4.34	—	—
Damping Ratio	0.585	0.655	0.683	—	—
Time Constant, Sec	—	—	—	0.385	0.977

Since changing the pseudoinverse weighting matrix primarily affects only the longitudinal dynamics, further investigations will concentrate on  $\Delta a_n$  step responses shown in Fig. 5. Figure 6 shows the corresponding control time histories. The interesting results are the Type 1 control steady state positions in Fig. 6 and the initial negative movement of  $\Delta a_n$  in Fig. 5. Unlike the Type 0 control steady state position, the Type 1 control steady state positions do not agree with Eqs. 14 and 15. The Type 0 control law compares the states and controls with  $\Omega_{12}\Delta y_d$  and  $\Omega_{22}\Delta y_d$ , respectively. Since  $\Omega_{12}$  and  $\Omega_{22}$  are exactly "matched" to the plant, the Type 0 control law drives the command errors,  $\Delta x - \Omega_{12}\Delta y_d$  and  $\Delta u - \Omega_{22}\Delta y_d$  to zero. On the other hand, the Type 1 control law only compares  $\Delta y$  to  $\Delta y_d$  and drives the command error  $\Delta y - \Delta y_d$  to zero.

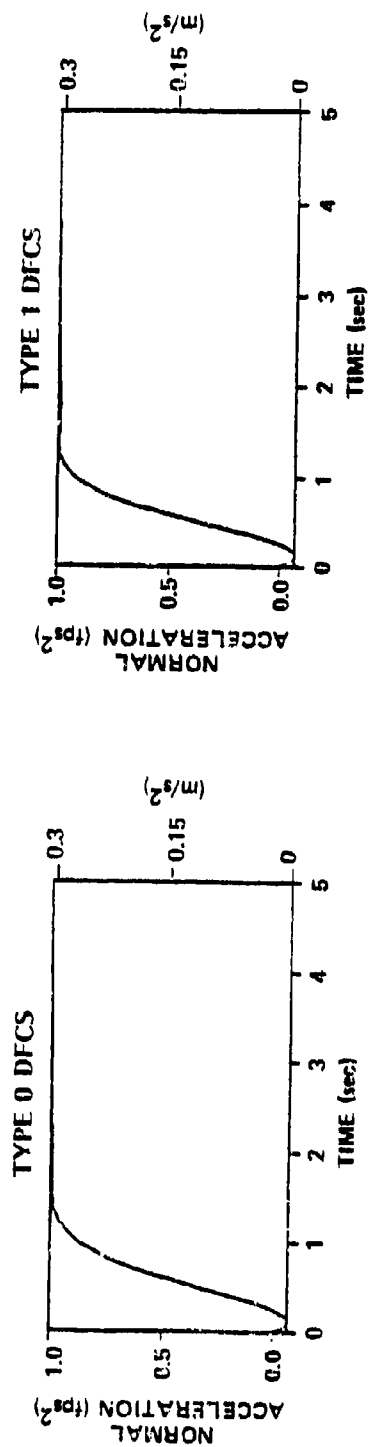
The Type 1 control law does not have a reference that would enable it to choose among the number of control steady state positions for  $\Delta \delta_s$  and  $\Delta \delta_{mf}$  which drives  $\Delta a_n$  to  $\Delta a_{nc}$ . The steady state values for two controls accommodating only one  $\Delta a_n$  command error simultaneously, depend on elements in  $C_1$  and  $C_2$  and on the past trajectory of the plant states and controls. The ambiguity of the Type 1 control steady state positions for  $\Delta a_n$  is, of course, completely eliminated when the additional control,  $\Delta \delta_{mf}$ , is fixed.

When stabilators are deflected to generate an upward normal acceleration, the initial pitching of the aircraft can cause the normal acceleration response to dip before arriving at the proper value as shown in Fig. 5. Dynamically, the equations of motion have a zero in the right half plane. By suitably adjusting  $Q_s$  in Eq. 8 and by changing the control response it is possible to shift the zero because of the extra design freedom caused by maneuver flap (Ref. 13). Figure 7 shows the more favorable normal acceleration response caused by using



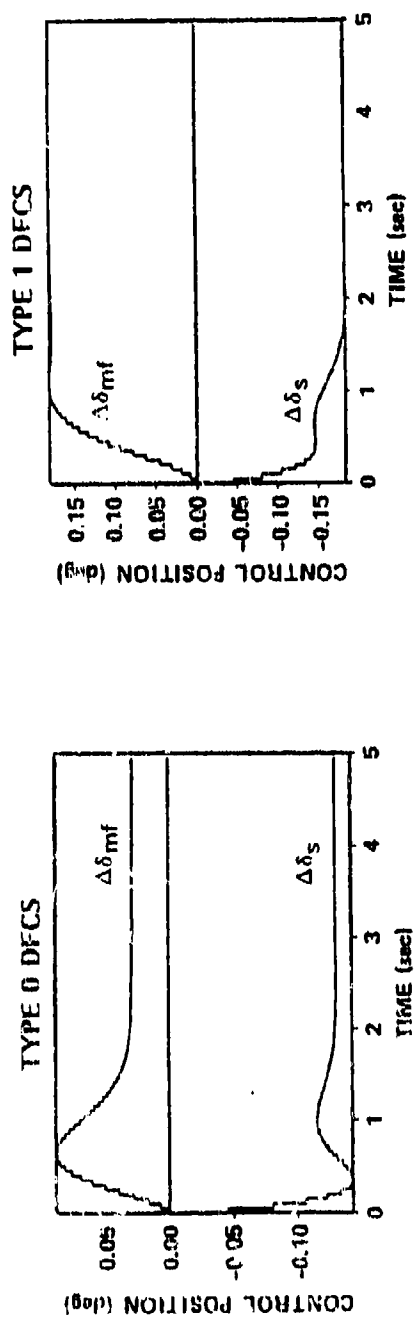


a) Pseudoinverse Control Weighting = 100/Max

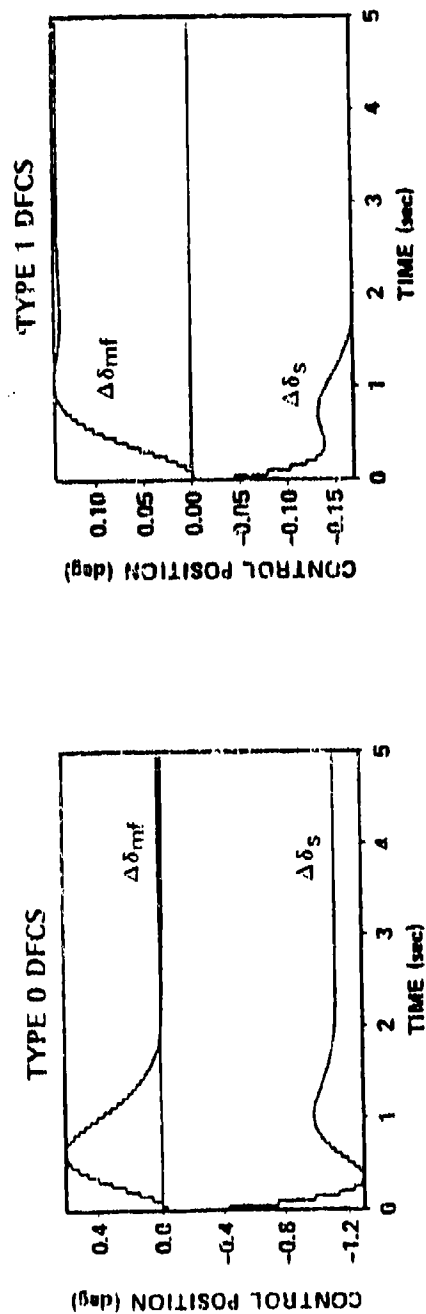


b) Pseudoinverse Control Weighting = 1000/Max

Figure 5 Normal Acceleration Step Responses At Design Point 1



a) Pseudoinverse Control Weighting = 100/Max



b) Pseudoinverse Control Weighting = 1000/Max

Figure 6 Control Movements for Normal Acceleration Step Responses

unity pseudoinverse weighting. The right half plane zero has been shifted to the stable left half plane, and the normal acceleration response has been "quickened" by the maneuver flap.

Summarizing the results thus far, the Type 1 discrete control law changes closed-loop eigenvalue locations for changes in the quad partition matrix pseudoinverse weighting matrix, while the Type 0 control law closed-loop eigenvalues do not change. Different pseudoinverse weighting matrices do not significantly change the effective operating range of the Type 1 control law but can desirably change the operating range of the Type 0 control law. Based on these observations, the Type 1 discrete control law is designed with unity pseudoinverse weighting as is done in Ref. 3 for the continuous time case. Unity pseudoinverse weighting provides good closed-loop eigenvalue locations in transforming from the Type 0 to Type 1 DFCS as demonstrated in Tables 5 and 6. The discrete time Type 0 DFCS will use  $\Omega_{12}$  and  $\Omega_{22}$  generated using unity pseudo inverse state weighting and 100/MAX control weighting. This weighting scheme delays the saturation of maneuver flap until very large  $\Delta a_n$  commands are requested, increasing the normal operational range of the Type 0 discrete DFCS. Note however that, as will be shown at the end of this section, favorably saturating maneuver flap does not decrease the operational range of the Type 1 DFCS.

The discrete DFCS Type 0 and Type 1 design step responses is presented in Figs. 7 to 12. Each of the three commands are individually stepped to unity and the perturbation state and control responses are plotted. Overlaid on the normal acceleration step response in Figs. 7 and 10 are the Category II boundaries for the  $C^*$  response taken from Ref. 17.  $C^*$  and  $a_n$  are not equally comparable but the boundary does

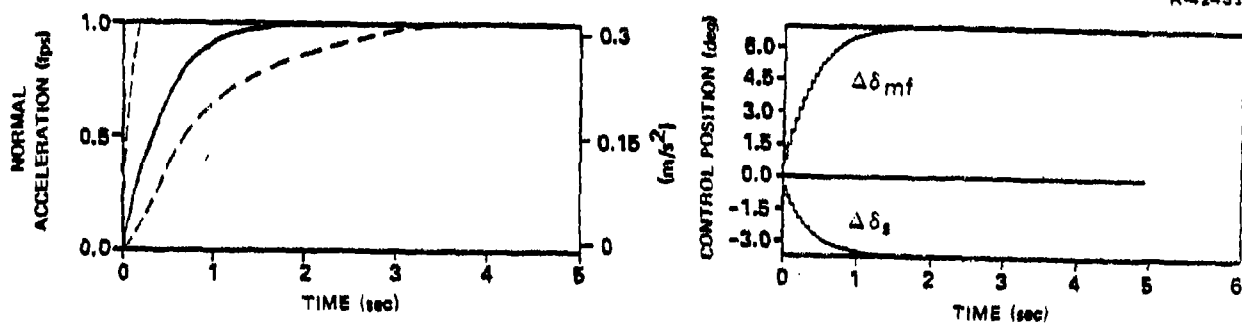


Figure 7 Type 1 DFCS  $\Delta a_n$  Step Response

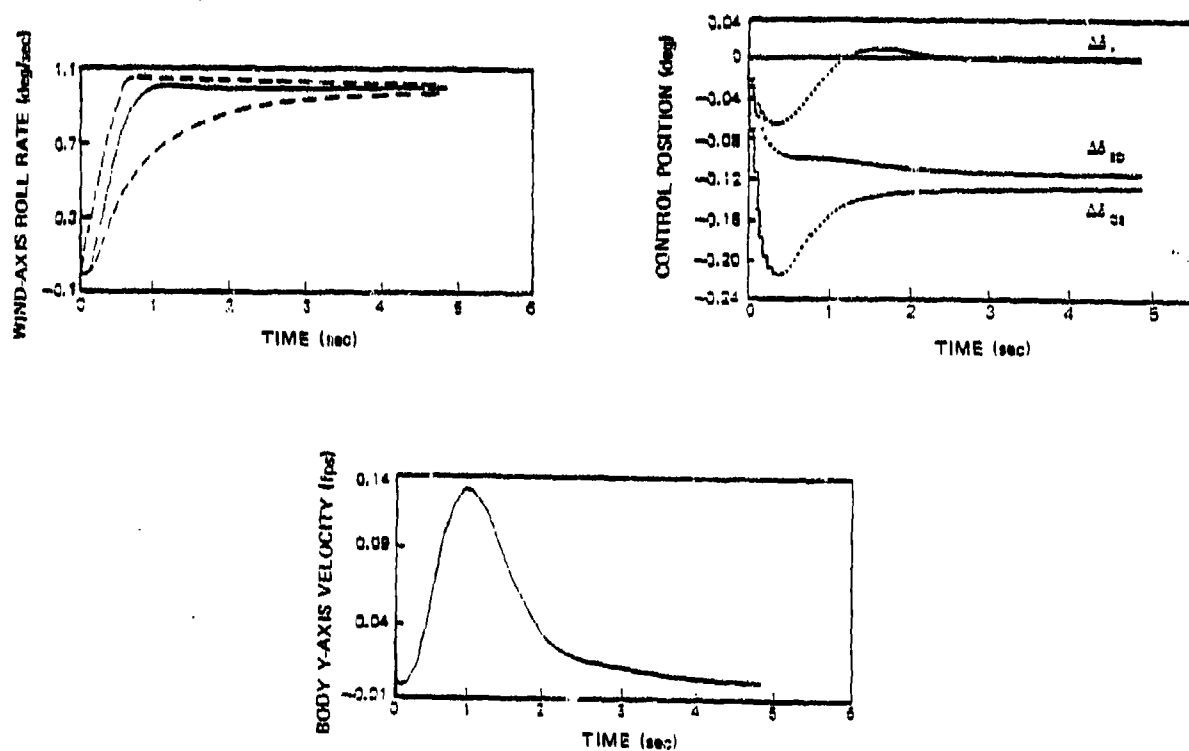


Figure 8 Type 1 DFCS  $\Delta p_w$  Step Response

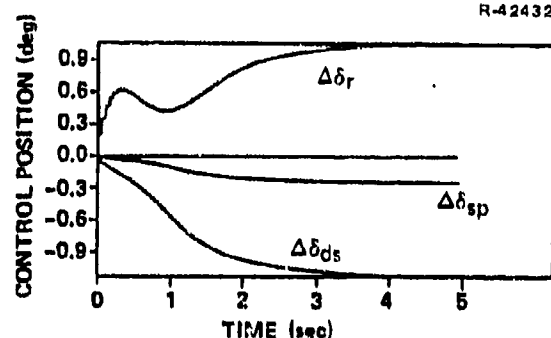
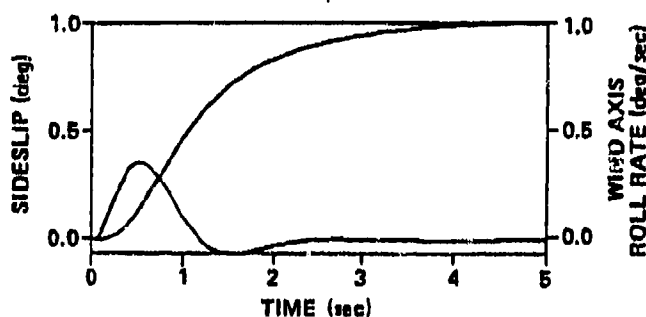


Figure 9 Type 1 DFCS  $\Delta\beta$  Step Response

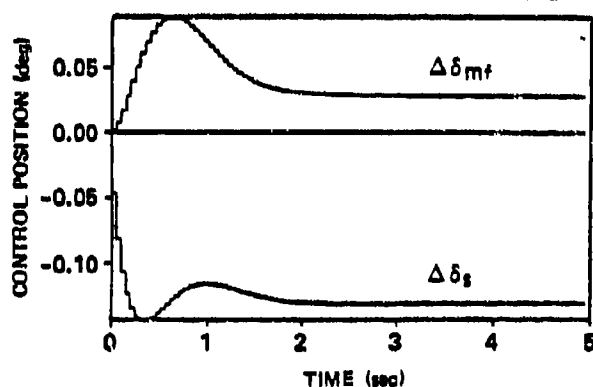
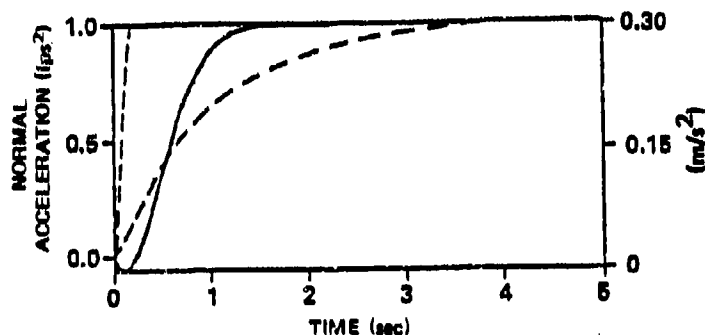


Figure 10 Type 0 DFCS  $\Delta a_n$  Step Response

give an indication of the approximate performance of the DFCS transients. Overlaid on the wind axis roll rate transient in Figs. 8 and 11 is the Category II boundary for the roll rate response also taken from Ref. 17. Again  $p$  and  $p_w$  are not equally comparable but the  $p_w$  transient falls well within the envelope. No step response transient envelope is available for sideslip. Sideslip response in Figs. 8 and 11 during a roll rate step response is reduced until the deviation falls within the limits specified in Ref. 15.

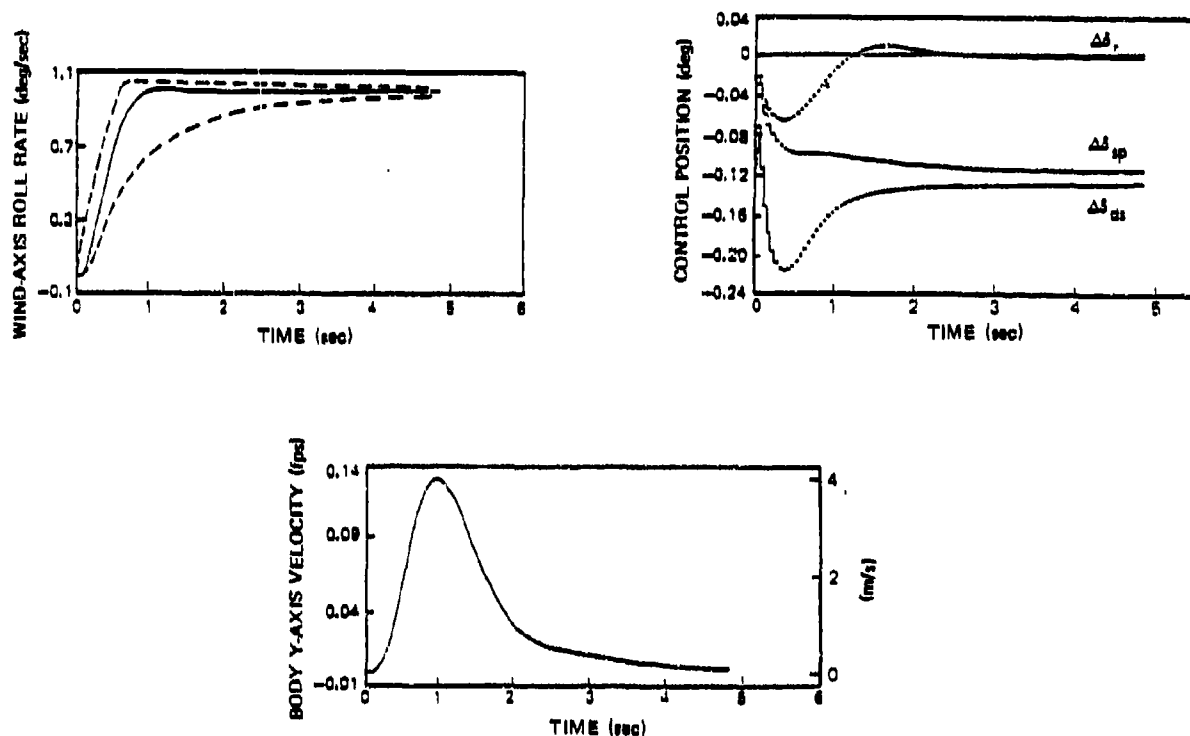


Figure 11 Type 0 DFCS  $\Delta p_w$  Step Response

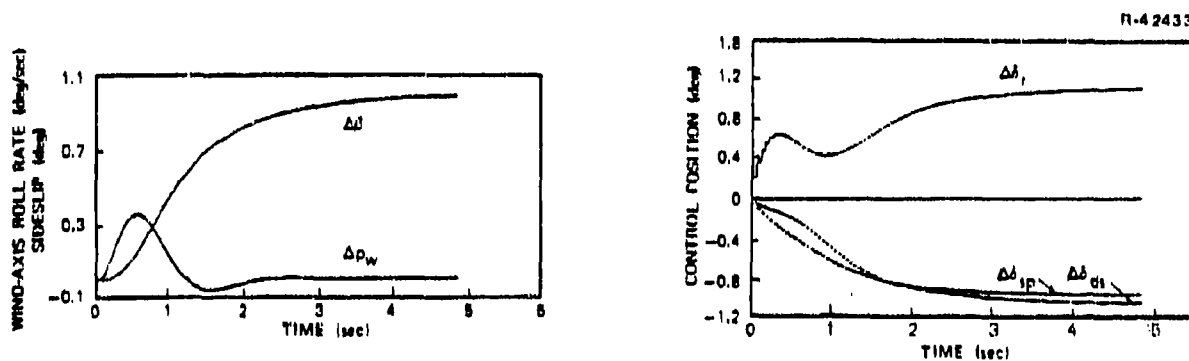


Figure 12 Type 0 DFCS  $\Delta \beta$  Step Response

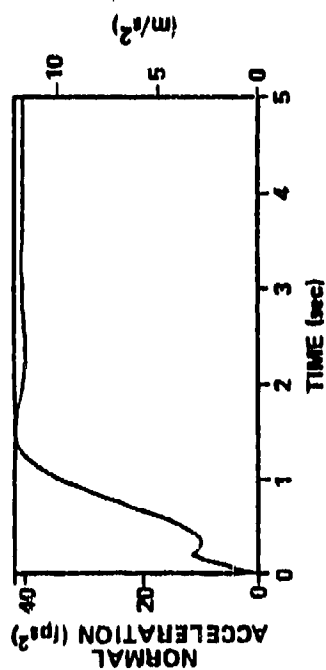
The Type 0 DFCS does not perform as well as the Type 1 DFCS for the  $\Delta a_n$  response. The use of unity pseudoinverse weighting for the Type 1 DFCS speeds up the response using large control movements without compromising the effective

operating range of the aircraft. In the Type 0 DFCS, a trade-off is being made between small control movements and speed of response. The steady state values for  $\Delta\delta_{mf}$  and  $\Delta\delta_s$  for a  $0.305 \text{ m/s}^2$  ( $1 \text{ fps}^2$ )  $\Delta a_n$  command using the Type 1 DFCS are  $0.710 \text{ deg}$  and  $-0.377 \text{ deg}$ , respectively, as shown in Fig. 7. The corresponding Type 0 DFCS steady state values are  $-0.321$  for  $\Delta\delta_s$  and  $0.557$  for  $\Delta\delta_{mf}$  in Fig. 10. It would appear that a  $\Delta a_n$  command above  $4.3 \text{ m/s}^2$  ( $\sim 1/2 \text{ g}$ ) would saturate maneuver flap rendering the Type 1 and Type 0 control laws inoperative for  $\Delta a_n$  commands above  $4.3 \text{ m/s}^2$  ( $1/2 \text{ g}$ ). This interpretation is entirely incorrect for the discrete Type 1 DFCS.

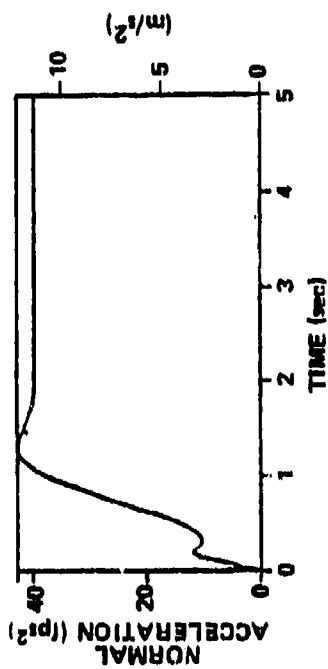
When a  $\Delta a_n$  command above  $4.3 \text{ m/s}^2$  ( $1/2 \text{ g}$ ) occurs, the Type 1 control law rapidly saturates maneuver flaps at  $10 \text{ deg}$  of travel. The Type 1 DFCS reduces to the situation where there is one control,  $\Delta\delta_s$ , which is to be commanded by the control law to meet the one requirement of forcing  $\Delta a_n$  to  $\Delta a_{nc}$ . The capability of the discrete Type 1 DFCS to handle control saturation through control reset is a unique feature of the incremental form and is discussed in previous paragraphs. As long as one longitudinal control is not saturated, the Type 1 control law will continually try to zero the command error with the unsaturated control surface. The Type 1 control law fully exploits all the capabilities of the aircraft and will accommodate the command until all available controls saturate.

A similar reset mechanism is also incorporated in the Type 0 control law. The Type 0 control law, however, does not have the integral property and is unable to automatically change control strategy. A demonstration of the Type 0 and Type 1 control law  $\Delta a_n$  response for a normal acceleration command of  $12.2 \text{ m/s}$  ( $1.25 \text{ g}$ ) is shown in Fig. 13. The Type 0 control law has a steady state error while the Type 1 control law does not. The Type 1 maneuver flap response unsaturates because stabilator

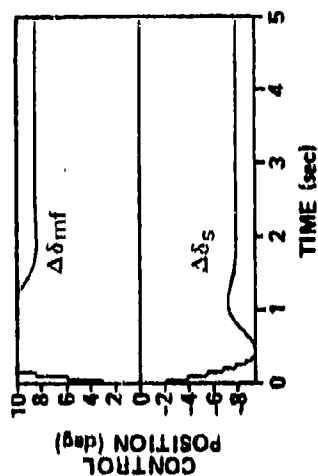
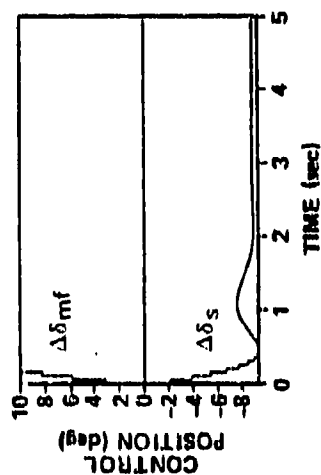
TYPE 0 RESPONSE  
UNITY PSEUDOINVERSE WEIGHTING



TYPE 1 RESPONSE  
UNITY PSEUDOINVERSE WEIGHTING



a) Normal Acceleration Response



b) Control Response

Figure 13 Effects of a Normal Acceleration Command Which Saturates Maneuver Flap



position compensates for the saturation and at the same time the command error changes sign because  $\Delta a_n$  overshoots the command. The resulting sign change in the maneuver flap incremental command,  $\Delta v_k$ , causes the control position for  $\Delta \delta_{mf}$  to reenter operational status. The Type 0 control law compares the maneuver flap position with  $\Omega_{22} \Delta y_d$ . The Type 0 command error does not change sign and maneuver flaps remains saturated. Similar behavior in the nonlinear simulations are shown in Chapter 3.

## 2.5 DESIGN PERFORMANCE AT THIRTY FLIGHT CONDITIONS

The design results for the entire range of flight conditions are presented in this section. The remaining twenty-nine point designs are performed with the cost function weighting elements shown in Table 4 for the primary design held essentially constant. The closed-loop mapped eigenvalues for the Type 1 and Type 0 DFCS are shown in Tables 7 and 8, respectively. The rise time, overshoot, and settling time for each command at each flight condition for the Type 1 DFCS is shown in Table 9.

The rise time is the time it takes the response to reach 90 percent of the commanded value. The overshoot is the maximum peak of the response expressed as a percentage of the command. The settling time is the time required for the response to settle within 5 percent of the commanded value. The step response characteristics in Table 9 show little overshoot and acceptable rise times with behavior much like those in Figs. 7 to 12.

There is some eigenvalue variation in transforming from the Type 0 (Table 8) to the Type 1 (Table 7) DFCS but the

TABLE 7  
TYPE 1 DFCS MAPPED CLOSED-LOOP EIGENVALUES FOR THE CONTROL SWEEP

T-3109

MANEUVER CONDITIONS			SHORT PERIOD		NORMAL ACCEL- ERATION COMMAND	ROLL COMMAND		DITCH ROLL		SIDESLIP COMMAND
$V_0$ m/s (fps)	$\alpha_0$ deg	$P_0$ deg/sec	$\omega$ rad/sec	$t$ sec	$\gamma$ sec	$\omega$ rad/sec	$t$ sec	$\omega$ rad/sec	$t$ sec	$\gamma$ sec
122 (400)	8.1	0.0	3.34	0.779	0.842	2.92	0.747	2.09	0.553	0.804
	15.3	0.0	3.28	0.814	0.492	2.96	0.606	2.03	0.668	0.826
	22.0	0.0	3.15	0.516	0.395	2.49	0.810	1.73	0.866	0.707
	26.7	0.0	2.96	0.558	0.363	2.37	0.757	1.45	0.842	0.759
183 (600)	2.36	0.0	5.71	0.677	0.411	4.53	0.786	3.49	0.591	0.982
	6.11	0.0	5.54	0.683	0.433	4.47	0.763	3.46	0.610	0.980
	9.78	0.0	5.54	0.715	0.368	4.34	0.682	3.46	0.655	0.977
	19.4	0.0	5.38	0.797	0.294	5.05	0.536	2.91	0.763	0.955
244 (800)	25.0	0.0	5.02	0.553	0.244	3.88	0.752	2.47	0.808	0.967
	33.4	0.0	4.11	0.597	0.232	3.43	0.685	2.22	0.858	1.38
	1.02	0.0	8.74	0.682	0.276	6.04	0.784	5.31	0.620	1.17
	3.4	0.0	8.45	0.672	0.275	6.02	0.779	5.27	0.622	1.17
	5.97	0.0	8.19	0.679	0.291	5.92	0.754	5.24	0.643	1.16
	12.5	0.0	7.07	0.759	0.223	6.40	0.624	4.66	0.715	1.14
	19.3	0.0	7.47	0.817	0.184	7.23	0.557	4.02	0.759	1.12
	23.4	0.0	7.31	0.573	0.151	5.46	0.794	3.55	0.786	1.13

TABLE 7  
TYPE 1 DFCS CLOSED-LOOP EIGENVALUES FOR  
THE CONTROL SWEEP (CONTINUED)

T-3110

MANEUVER CONDITIONS			SHORT PERIOD		NORMAL ACCEL- ERATION COMMAND	ROLL COMMAND		DUTCH ROLL		SIDESLIP COMMAND
$V$ $m/sec$ (fps)	$n$ $deg$	$F_w$ $deg/sec$	$\omega$ $rad/sec$	$\zeta$	$\tau$ sec	$\omega$ $rad/sec$	$\zeta$	$\omega$ $rad/sec$	$\zeta$	$\tau$ sec
122 (400)	21.1	50.0	3.13	0.432	0.383	2.58	0.730	2.02	0.875	0.816
	29.7	50.0	2.78	0.528	0.364	2.61	0.731	1.61	0.971	0.633
	17.0	100.0	3.74	0.359	2.84 <sup>±</sup>	3.21	0.667	1.27	0.959	0.966 <sup>±</sup>
133 (600)	21.6	100.0	3.54	0.350	0.358	3.07	0.638	1.31	0.988	0.485
	10.4	50.0	5.32	0.525	0.367	5.20	0.807	3.35	0.692	0.952
	19.0	50.0	5.13	0.520	0.307	5.15	0.791	3.17	0.778	0.955
266 (800)	30.9	50.0	4.11	0.578	0.265	3.99	0.637	2.08	0.890	1.16
	9.6	100.0	5.89	0.597	0.472	5.09	0.779	3.57	0.763	0.917
	17.6	100.0	5.43	0.496	0.376	6.75	0.718	3.94	0.905	0.926
	7.1	50.0	8.34	0.651	0.279	6.06	0.743	5.20	0.680	1.15
	22.8	50.0	7.22	0.560	0.220	7.29	0.796	4.68	0.709	1.15
	19.1	50.0	7.30	0.547	0.187	7.30	0.814	4.19	0.759	1.13
	6.78	100.0	8.36	0.594	0.306	6.68	0.768	5.30	0.696	1.14
	12.1	100.0	7.12	0.569	0.266	6.42	0.711	5.24	0.808	1.14

<sup>±</sup>COMPLEX ROOT ( $\sigma_n$ ,  $\zeta$ )

TABLE 8  
TYPE 0 DFCS MAPPED CLOSED-LOOP EIGENVALUES FOR THE CONTROL SWEEP

T-3111

MANEUVER CONDITIONS			SHORT PERIOD		NORMAL ACCEL- ERATION COMMAND	LONGI- TUDINAL CONTROL	ROLL COMMAND		DITCH ROLL		SIDESLIP COMMAND	SPOTLER
$V_0$ m/s (fps)	$\alpha$ deg	$P_0$ deg/sec	$\omega$ rad/sec	$\zeta$	$\tau$ sec	$\tau$ sec	$\omega$ rad/sec	$\zeta$	$\omega$ rad/sec	$\zeta$	$\tau$ sec	$\tau$ sec
122 (400)	8.1	0.0	2.92	0.747	0.862	0.314	2.38	0.579	2.09	0.553	0.835	0.638
	15.3	0.0	2.96	0.606	0.844	0.292	2.23	0.637	2.03	0.668	0.824	0.657
	22.0	0.0	3.15	0.516	0.788	0.281	2.02	0.535	1.72	0.807	0.843	1.005
	26.7	0.0	2.96	0.558	0.759	0.283	2.03	0.500	1.45	0.842	0.847	1.08
183 (600)	2.76	0.0	4.68	0.642	0.390	0.334	4.54	0.786	3.50	0.591	0.983	0.869
	6.11	0.0	4.47	0.763	0.383	0.354	4.41	0.642	3.46	0.610	0.978	0.863
	9.78	0.0	4.21	0.665	0.406	0.322	4.34	0.682	3.46	0.656	0.984	0.868
	19.4	0.0	5.05	0.536	0.479	0.267	3.83	0.776	2.91	0.763	0.955	0.844
244 (800)	25.0	0.0	5.02	0.553	0.869	0.208	3.17	0.627	2.47	0.808	0.976	0.847
	31.4	0.0	4.12	0.597	1.51	0.228	3.18	0.597	2.22	0.858	1.38	0.847
	1.02	0.0	7.29	0.679	0.392	0.252	6.04	0.784	5.31	0.619	1.17	0.866
	3.45	0.0	7.14	0.664	0.384	0.269	6.01	0.779	5.28	0.622	1.17	0.869
	5.97	0.0	6.77	0.671	0.370	0.274	5.93	0.754	5.24	0.643	1.16	0.869
	12.5	0.0	6.40	0.624	0.561	0.207	5.63	0.764	4.66	0.715	1.14	0.847
	19.3	0.0	7.23	0.557	0.497	0.166	5.70	0.842	4.03	0.759	1.12	0.844
	23.4	0.0	7.31	0.573	0.724	0.136	4.43	0.741	3.65	0.786	1.13	0.844

TABLE 8  
TYPE 0 DFCS MAPPED CLOSED-LOOP EIGENVALUES  
FOR THE CONTROL SWEEP (CONTINUED)

T-3112

MANEUVER CONDITIONS			SHORT PERIOD		NORMAL ACCELERATION COMMAND	LONGITUDINAL CONTROL	ROLL COMMAND		DITCH ROLL		SIDESLIP COMMAND	SPOILER
$V_0$ m/ (fps)	$\alpha$ deg	$P_0$ deg/sec	$\omega$ rad/sec	$\zeta$	$\tau$ sec	$\tau$ sec	$\omega$ rad/sec	$\zeta$	$\omega$ rad/sec	$\zeta$	$\tau$ sec	$\tau$ sec
122 (400)	22.1	50.0	3.32	0.410	0.843	0.280	2.51	0.634	1.52	0.794	1.15 <sup>±</sup>	0.991 <sup>±</sup>
	29.7	50.0	2.65	0.462	0.730	0.290	2.45	0.689	1.28	0.911	1.19	0.844
	17.9	100.0	3.71	0.336	0.562	0.283	3.22	0.646	1.31	0.931	0.877	0.847
	21.4	100.0	3.56	0.333	1.07 <sup>±</sup>	0.275	3.02	0.603	1.34	0.987	0.828 <sup>±</sup>	0.844
183 (600)	10.4	50.0	5.13	0.467	0.667	0.310	4.61	0.839	3.24	0.683	0.980	0.847
	19.0	50.0	5.09	0.514	0.474	0.244	3.98	0.704	2.81	0.848	0.961	0.847
	30.9	50.0	4.30	0.649	1.32	0.231	3.56	0.486	1.98	0.879	1.16	0.844
	9.6	100.0	5.69	0.445	0.535	0.339	4.69	0.805	3.34	0.758	0.952	0.847
244 (800)	17.6	100.0	5.29	0.472	0.459	0.276	4.57	0.670	2.63	0.972	0.943	0.847
	7.1	50.0	7.10	0.608	0.365	0.271	6.03	0.766	5.10	0.689	1.16	0.857
	12.8	50.0	7.03	0.524	0.445	0.208	6.34	0.833	4.69	0.705	1.15	0.844
	19.1	50.0	7.28	0.545	0.500	0.166	5.45	0.817	4.25	0.788	1.13	0.844
	6.78	100.0	7.73	0.521	0.415	0.103	6.48	0.822	5.15	0.696	1.16	0.855
	12.1	100.0	6.89	0.534	0.490	0.219	5.97	0.688	4.39	0.873	1.14	0.847

<sup>±</sup>COMPLEX ROOT ( $\omega_n$ ,  $\zeta$ )

TABLE 9  
STEP RESPONSE CHARACTERISTICS FOR THE TYPE 1 DFCS SWEEP

T-3113

HANDOVER CONDITIONS			NORMAL ACCELERATION COMMAND			SIDESLIP COMMAND			STABILITY-AXIS ROLL RATE COMMAND		
$V_0$ m/s (fps)	$\alpha_0$ deg	$P_0$ deg/sec	RISE TIME, sec	OVER- SHOOT, percent	SETTLING TIME sec	RISE TIME, sec	OVER- SHOOT, percent	SETTLING TIME, sec	RISE TIME sec	OVER- SHOOT, percent	SETTLING TIME sec
122 (400)	8.1	0.0	1.90	-	2.65	2.10	-	2.60	1.00	1.50	1.10
	15.3	0.0	1.30	-	1.70	2.20	-	2.55	1.05	0.90	1.20
	22.0	0.0	1.55	-	1.95	2.60	-	2.95	1.35	1.18	1.60
	26.7	0.0	1.55	-	1.95	2.50	-	3.15	1.70	1.20	1.90
183 (600)	2.76	0.0	1.00	-	1.25	2.55	-	3.20	0.65	1.80	0.70
	6.11	0.0	1.65	-	1.35	2.55	-	3.20	0.65	1.80	0.70
	9.78	0.0	1.00	-	1.30	2.55	-	3.20	0.75	1.60	0.80
	19.4	0.0	0.75	-	0.95	2.55	-	3.15	0.80	1.55	0.90
244 (800)	25.0	0.0	0.90	0.12	1.10	2.55	-	3.20	1.05	1.66	1.15
	33.4	0.0	1.00	2.0	1.15	3.45	-	4.40	1.30	1.38	1.45
	1.02	0.0	0.65	-	0.85	2.90	-	3.70	0.50	1.90	0.55
	3.45	0.0	0.65	-	0.85	2.90	-	3.70	0.50	1.92	0.55
	5.97	0.0	0.70	-	0.90	2.90	-	3.70	0.50	2.00	0.55
	12.5	0.0	0.55	-	0.75	2.85	-	3.65	0.50	2.25	0.55
	19.3	0.0	0.50	-	0.65	2.80	-	3.55	0.60	2.02	0.70
	23.4	0.0	0.55	-	0.70	2.80	-	3.60	0.70	2.03	0.80

TABLE 9  
STEP RESPONSE CHARACTERISTICS FOR THE TYPE 1 DFCS SWEEP  
(CONTINUED)

T-3144

MANEUVER CONDITIONS			NORMAL ACCELERATION COMMAND			SIDESLIP COMMAND			STABILITY-AXIS POLA. RATE COMMAND		
$V_a$ m/s (fps)	$\alpha_a$ deg	$P_a$ deg/sec	RISE TIME, sec	OVER- SHOOT, PERCENT	SETTLING TIME, sec	RISE TIME, sec	OVER- SHOOT, PERCENT	SETTLING TIME, sec	RISE TIME, sec	OVER- SHOOT, PERCENT	SETTLING TIME sec
122 (400)	21.1	50.0	1.15	-	1.65	2.2	-	2.85	1.25	1.3	1.4
	29.7	50.0	1.25	1.6	1.65	2.7	-	3.30	1.60	2.3	1.75
	17.0	100.0	0.95	-	1.10	2.5	-	2.95	1.05	-	1.25
	21.4	100.0	1.0	-	1.20	2.35	-	2.95	1.15	-	1.30
183 (600)	19.4	50.0	0.85	-	1.10	2.5	-	3.15	0.65	1.6	0.70
	19.0	50.0	0.75	-	0.95	2.5	-	3.15	0.80	1.6	0.85
	30.9	50.0	0.90	0.70	1.10	3.1	-	3.90	1.35	0.87	1.50
	9.6	100.0	0.85	-	1.10	2.65	-	3.10	0.65	0.22	0.70
244 (800)	17.6	100.0	0.70	-	0.85	2.50	-	3.15	0.70	1.00	0.80
	7.1	50.0	0.85	-	0.95	2.9	-	3.70	0.50	2.32	0.55
	12.8	50.0	0.55	-	0.70	2.85	-	3.65	0.55	1.97	0.60
	19.1	50.0	0.50	-	0.60	2.80	-	3.55	0.60	2.10	0.70
	6.78	100.0	0.70	-	0.90	2.85	-	3.65	0.50	1.61	0.55
	12.1	100.0	0.55	-	0.70	2.85	-	3.65	0.50	2.52	0.55

general trend is to improve the eigenvalue location. The largest eigenvalue change in transforming from the Type 0 to the Type 1 DFCS is the normal acceleration command mode which becomes faster (i.e., more stable). The short period mode exhibits the required increase in natural frequency with increased dynamic pressure. When the aircraft is rolling ( $p_w \neq 0.0$ ) the short period damping ratios all decrease in Table 7 and 8. On the other hand the Dutch roll damping improves when rolling. Except for two flight conditions ( $V_o = 122$  m/s,  $\alpha_o = 17$  deg, and  $\alpha_o = 21.4$  deg,  $p_{wo} = 100$  deg/sec) all closed-loop eigenvalues remain with the requirements specified by MIL-F-8785B. These two flight conditions are considered to be extreme and the transgression is minor (short period damping ratio = 0.33 instead of 0.35).

## 2.6 EFFECTS OF GAIN SCHEDULING

After the optimal point designs are complete, the resulting thirty sets of gains are regressed against functions of the trimmed flight conditions in order to find highly correlated relationships. Four function sets are found to be highly correlated and are used for gain scheduling. They are

$$\text{Gain} = a_1 \alpha + \frac{a_2 280}{\alpha^2 - 30\alpha + 280} + a_3 a_n v^2 + a_4 \quad (\text{Schedule 1})$$

$$\text{Gain} = a_1 v^2 + a_2 \alpha + a_3 a_n + a_4 \quad (\text{Schedule 2}) \quad (16)$$

$$\text{Gain} = a_1 p_w v^2 + a_2 p_w \alpha + a_3 p_w a_n + a_4$$

$$\text{Gain} = a_1 p_w \alpha + \frac{a_2 p_w 280}{\alpha^2 - 30\alpha + 280} + a_3 p_w a_n v^2 + a_4$$



where  $a_1$  to  $a_3$  are the regression coefficients and  $a_4$  is the regression constant. These gain schedules are derived from flight conditions at one altitude (6,100 m, 20,000 ft) but the major effects of altitude can be incorporated by replacing the  $v^2$  terms with  $\frac{1}{2} \rho_\infty v^2$ . The term  $\rho_\infty$  is the local air density. Schedule 1 and Schedule 2 are for the primary longitudinal and lateral-directional gains while the latter two sets are for the cross-coupling gains that are non-zero when  $p_w$  is non-zero. Each gain is scheduled using the function set that yields the highest correlation coefficient.

The Type 0 DFCS described by Eqs. 2 to 4 requires 80 gains to be scheduled. The Type 1 DFCS described by Eq. 1 requires the scheduling of only 40 gains. The scheduled gains generally have correlation coefficients,  $\rho$ , greater than 0.8 with the optimal gains. The effect of the gain schedule on closed-loop eigenvalues is shown in Figs. 14 and 15 for a sweep in angle of attack. The Type 1 DFCS gain schedule design remains within the requirements of MIL-F-8785B throughout the angle of attack sweep. The Type 0 DFCS, however, has a problem with the sideslip command mode as shown in Fig. 15. Near 16 deg  $\alpha_0$  the closed-loop mode briefly goes unstable using schedule 1.

From previous work in Refs. 1 and 3, it is known that the fighter aircraft under consideration has control reversals occurring in the lateral-directional axis near 16 deg  $\alpha_0$ . An important part of this study is to determine if the gain schedule constructed here can accurately capture control gain sign changes. In summary the Type 1 gain schedules performed very well while the initial Type 0 gain schedules had difficulties.

The instability of the  $\Delta\beta$  command mode in Fig. 15 can be traced to two gains which are plotted in Fig. 16b; the  $\Delta v$

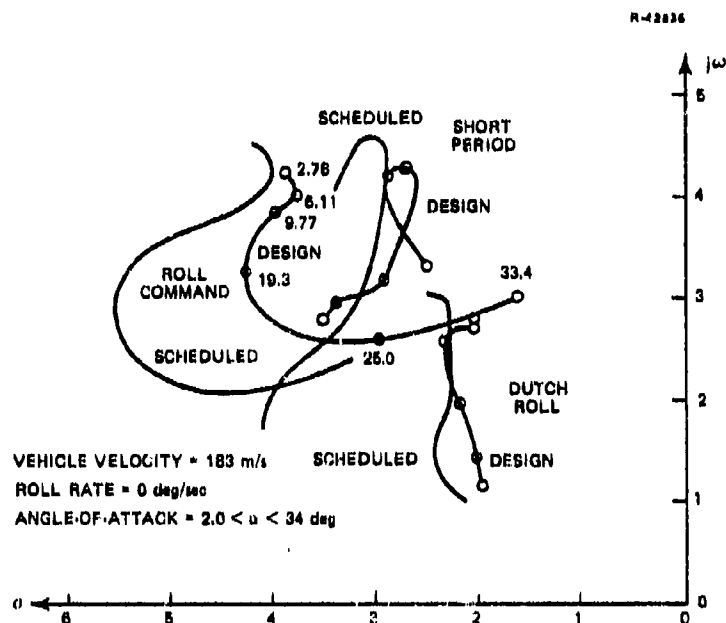
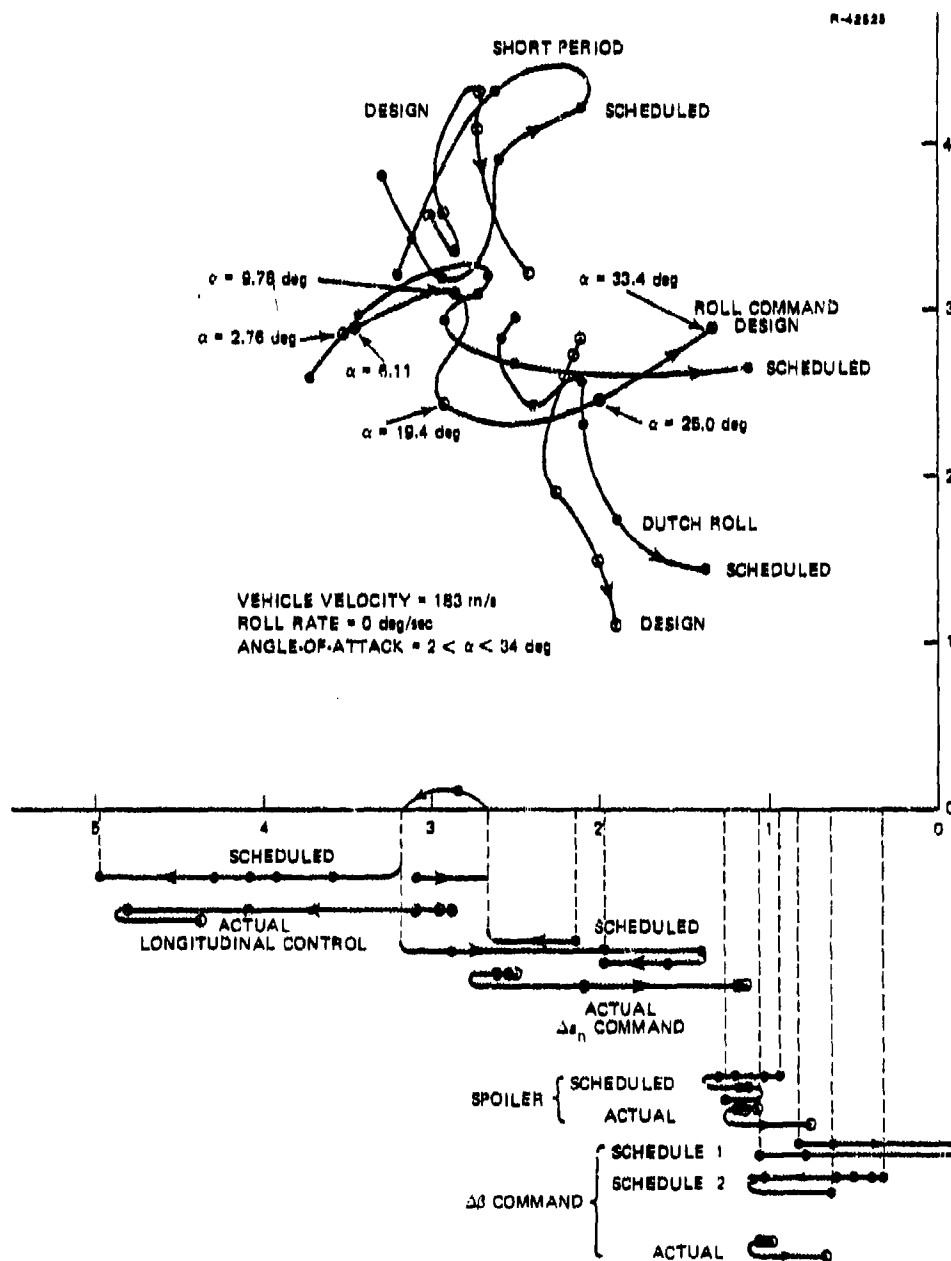


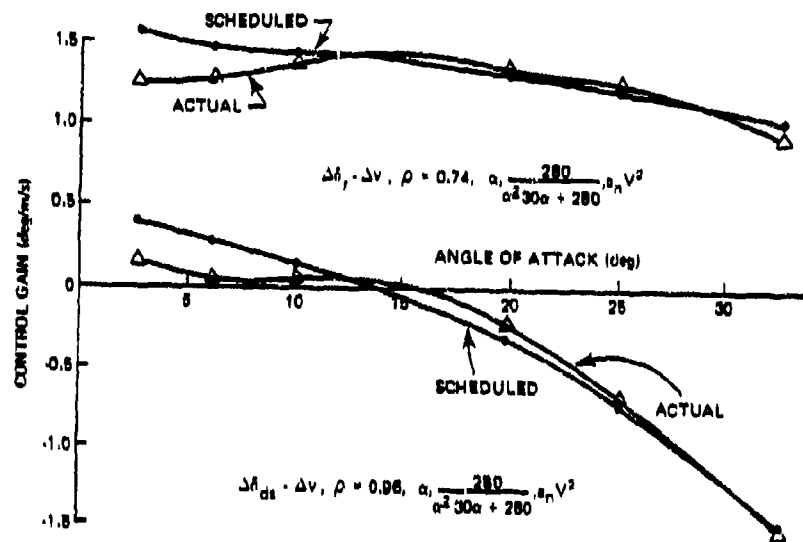
Figure 14 Effects of the Gain Schedule on Closed-Loop Type 1 DFCS Mapped Eigenvalues

to  $\Delta\delta_r$  gain and the  $\Delta v$  to  $\Delta\delta_{ds}$  gain. Schedule 1 has the highest correlation with these two gains and was originally implemented. Schedule 1 closely matches the gains except near 16 deg  $\alpha_o$ . Schedule 2 is a different gain schedule shown in Eq. 16 and has lower correlation with the optimal gain. Schedule 2, however, maintains, stability as shown in Fig. 15.

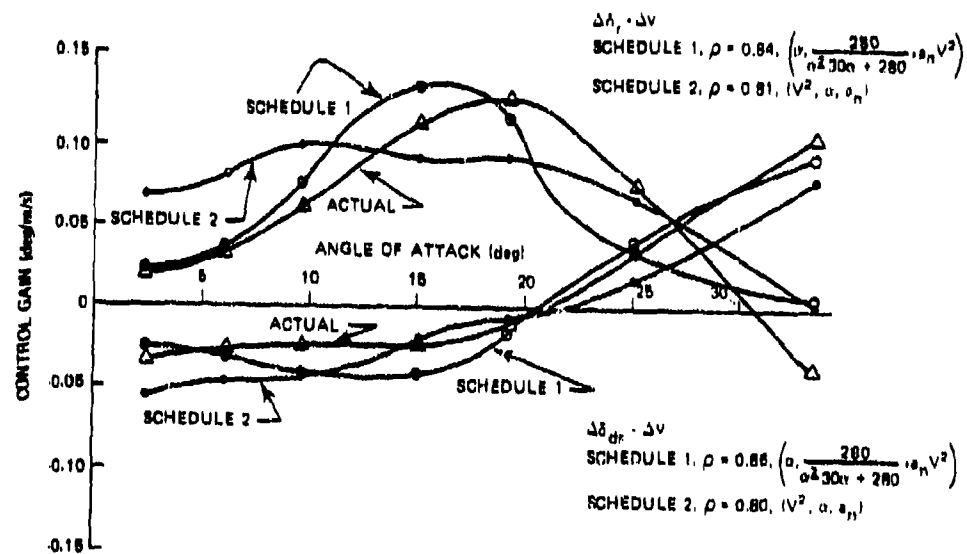
Examples of Type 1 scheduled gains are shown in Figs. 16a and Fig. 17. The scheduled gains closely match the optimal gains particularly near 16 deg  $\alpha_o$ . The  $\Delta w$  to  $\Delta\delta_s$  gain in Fig. 17 and the  $\Delta v$  to  $\Delta\delta_r$  gain in Fig. 16a show the "bump" near 16 deg  $\alpha_o$  with a roll off as  $\alpha_o$  increases that the function  $280/(\alpha^2 - 30\alpha + 280)$  tries to capture. The Type 1 gain scheduled design step responses in Fig. 18 at the primary design point are essentially the same as the optimal control step responses.



F' e 15 Effects of the Gain Schedule on Closed-Loop Type 0 DFCS Mapped Eigenvalues



a) Type 1 DFCS



b) Type 0 DFCS

Figure 16 Control Gain Variation With Angle of Attack  
 $(V = 183 \text{ m/s (600 fps)}, p_{w_0} = 0 \text{ deg/sec})$

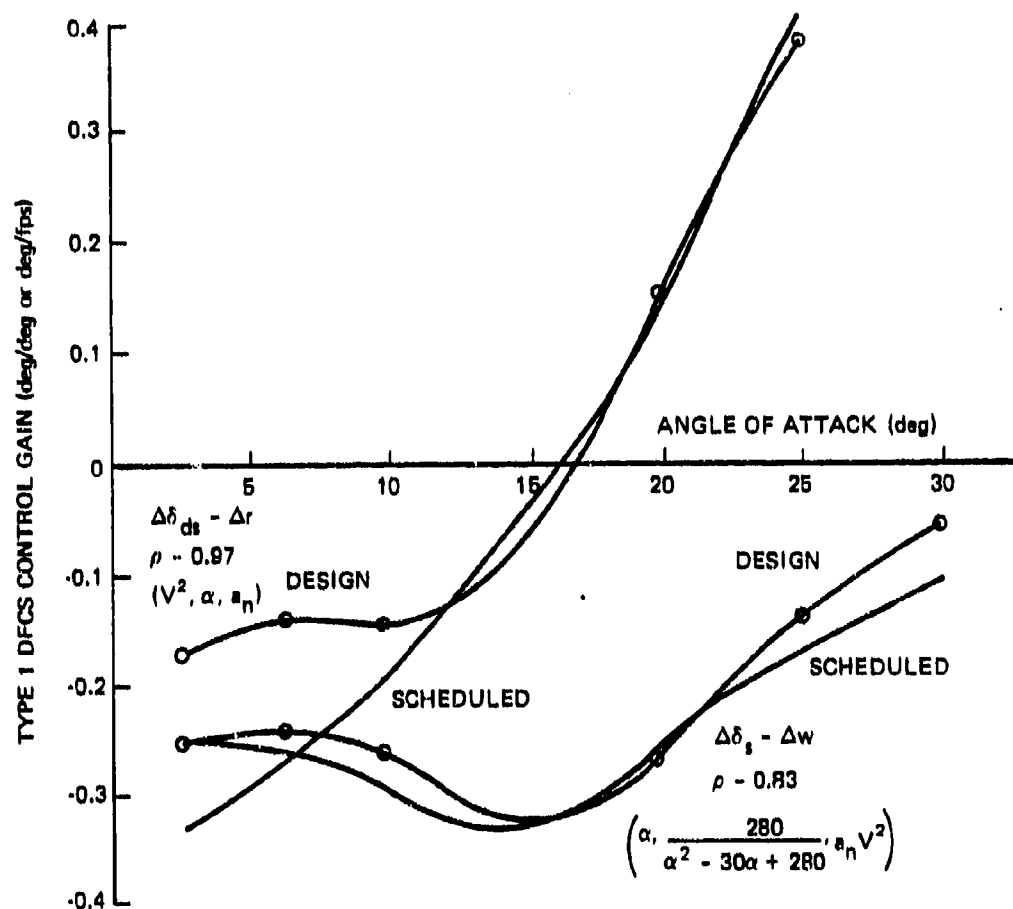


Figure 17 Control Gain Variation With Angle of Attack  
( $V = 183$  m/s (600 fps),  $p_w = 0$  deg/sec)

## 2.7 CHAPTER SUMMARY

This chapter presents the design of Type 0 and Type 1 digital control laws for a fighter aircraft. The Type 1 design is successful and is suitable for full evaluation in a nonlinear simulation as is done in Chapter 3. Numerous difficulties are encountered in simultaneously designing the Type 0 control law. It is concluded that the Type 0 control structure with the low-pass filter effect and no integral compensation is not a suitable controller for the fighter aircraft.

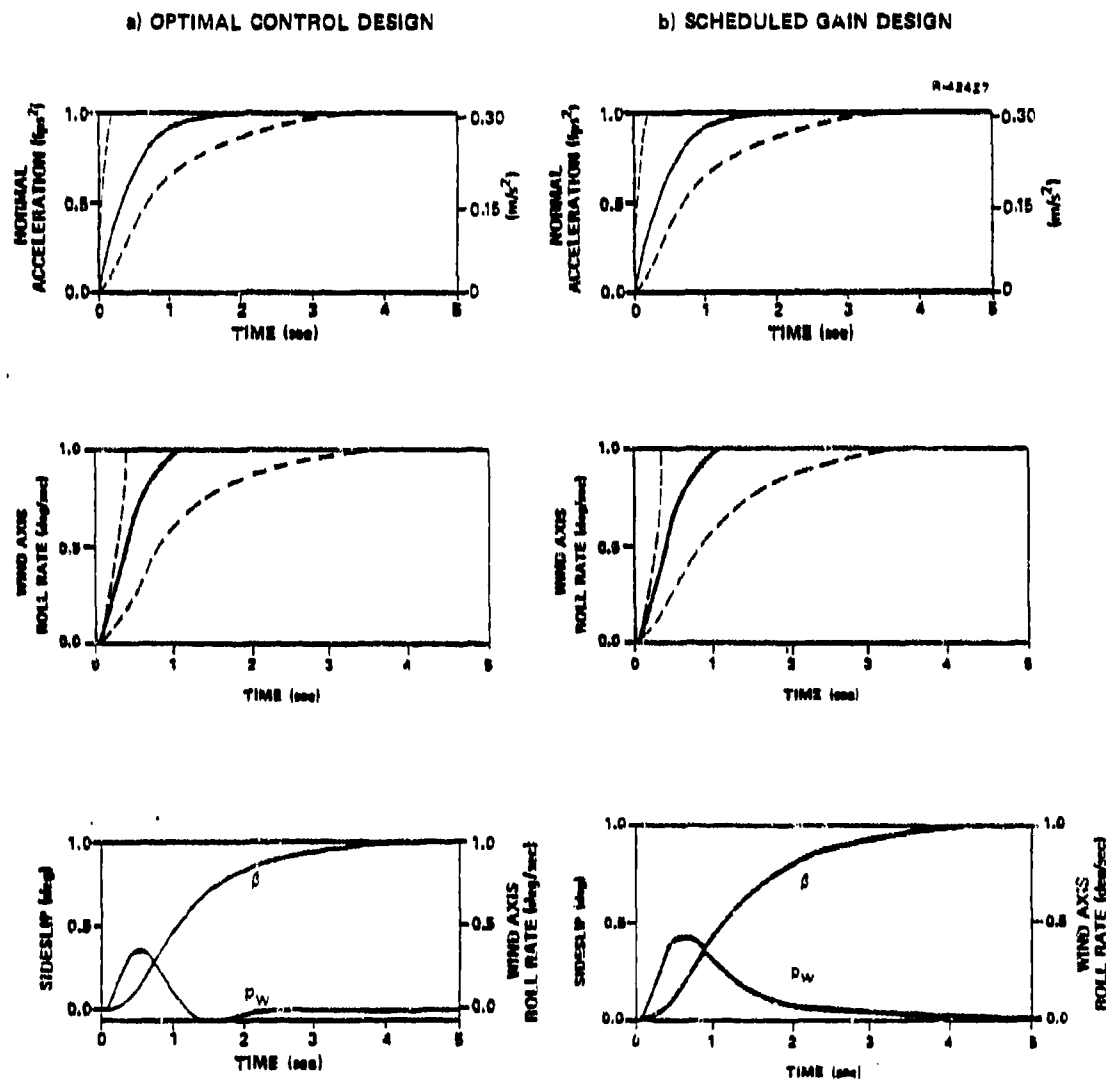


Figure 18 DFCS Step Response Performance at the Design Flight Condition

Although both the Type 0 and Type 1 laws are direct digital designs, the cost function weights and desired closed-loop eigenvalues and eigenvectors are chosen using continuous-time specifications. This is accomplished by using the sampled-data regulator and by mapping the resulting discrete closed-loop system to an equivalent continuous system using the log of a matrix.

There are four steps in the Type 1 and Type 0 DFCS designs that represent the "art" in the design procedure. Detailed discussions of each of the four steps are presented in this chapter. The first step is the choice of the pseudoinverse weighting matrix for inverting the quad partition matrix

$$\begin{bmatrix} (\Phi - I) & \Gamma \\ H & D \end{bmatrix}$$

used in calculating the steady-state feedforward matrix. The quad partition matrix is not square because three commands are driven by five controls. The pseudoinverse allows for the optimal blending of steady-state control surfaces to satisfy the command requirements. The second step is the choice of the optimal control quadratic weights subject to what constitutes a "good" design for a fighter aircraft. The third step is the choice of the pseudoinverse weighting matrix for inverting the quad partition matrix when transforming the control gains from the Type 0 to Type 1 structure. The primary objective of the third step is to reduce any adverse closed-loop eigenvalue variations caused by the transformation. A secondary objective is to place system zeroes in more desirable locations. The fourth step is the choice of the scheduling functions used in the control law gain schedules. The objective is to develop gain schedules that allow control gains to be computed as a function of flight condition for onboard implementation and

give nearly the same performance as the optimal control point design gains.

Evaluation of the gain schedule is an important part of the design because the reference aircraft is known to have an adverse yaw problem at high angles of attack. The Type 1 gain schedule effectively handles the control gain sign changes, while the initial Type 0 gain schedule demonstrates difficulties which are subsequently surmounted. A demonstration of the successful, gain scheduled Type 1 DFCS in demanding non-linear maneuvers is presented in the next chapter.



### 3. EVALUATION OF A FIGHTER AIRCRAFT DIGITAL FLIGHT CONTROL SYSTEM BY NONLINEAR SIMULATION

#### 3.1 OVERVIEW

The previous chapter describes the construction of a fighter aircraft digital flight control system (DFCS). The system is designed to produce accurate and well-damped response to commands, and it should be capable of operating over a wide range of velocity, normal acceleration, and roll rate. The control system is not sensitive to control surface actuator position limiting, as occurs in air combat maneuvering (ACM) flight. To test all of these attributes, this chapter details the construction, execution, and results of a series of experiments which compare the ACM tracking accuracy of the digital flight control system to the conventional control system presently on-board the aircraft.

The comparative tests, structured as shown in Fig. 19, are based on a simulation which is identical from experiment to experiment except for the control system structure. The same ACM tasks flown by the same pilot model are used, and the same nonlinear 6 degree-of-freedom aircraft model is used. The full authority digital flight control system is primarily compared to the conventional mechanical linkages with limited-authority analog sas. A third control system consisting of the mechanical linkages and digitally driven, limited-authority sas actuators is given limited testing. Section 3.2 discusses the details of the pilot and aircraft simulation, while Section 3.3 presents the control system models. The test results are included in Sections 3.4 through 3.6.

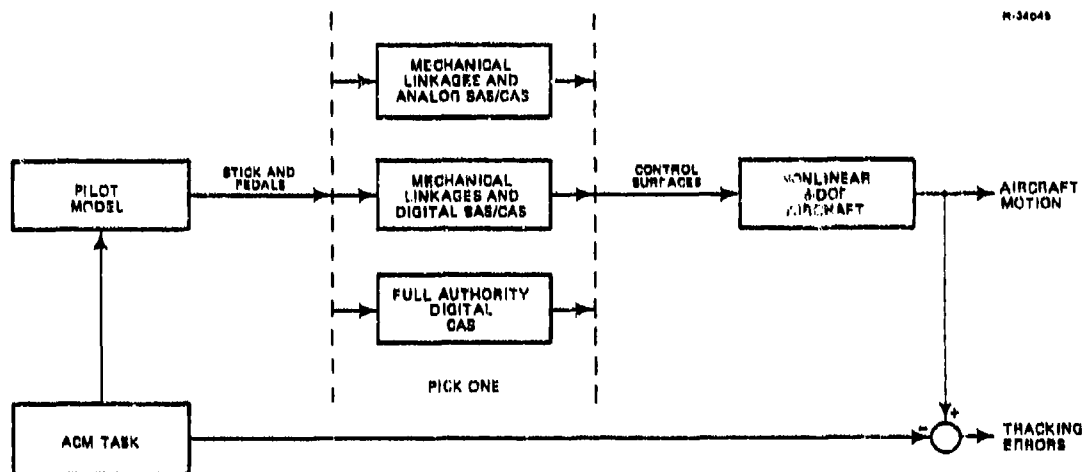


Figure 19 Test Structure

### 3.2 SIMULATION DESCRIPTION AND TEST PROCEDURE

The components of the ACM simulation are the nonlinear, 6-degree-of-freedom (DOF) aircraft simulation, the ACM pilot model, the ACM task definition, and the aircraft control system. All except the latter are discussed in this section. It is important to emphasize that in each of the experiments, only the control system is changed. This allows a direct comparison of the control system effectiveness.

#### 3.2.1 Nonlinear 6-DOF Aircraft Simulation

The aircraft dynamics are modeled by the nonlinear, 6 degree-of-freedom rigid-body equations of motion. The six kinematics equations are defined as

$$\begin{bmatrix} \dot{\underline{x}}_E \\ \dot{\underline{u}}_B \end{bmatrix} = \begin{bmatrix} H_B^E & \underline{v}_B \\ L_B^{-1} & \underline{\omega}_B \end{bmatrix} \quad (17)$$

where  $\underline{x}_E$  is the aircraft position vector,  $\underline{u}_B$  is the aircraft Euler angle vector,  $\underline{v}_B$  is the aircraft body-axis velocity vector,  $\underline{\omega}_B$  is the aircraft body-axis angular rate vector,  $H_B^E$  is the body-to-earth axis direction cosine matrix and  $L_B^{-1}$  is the body-to-Euler angular rate transformation matrix. The corresponding six dynamics equations complete the 12 rigid body state equations

$$\begin{bmatrix} \dot{\underline{v}}_B \\ \dot{\underline{\omega}}_B \end{bmatrix} = \begin{bmatrix} \underline{F}/m + H_E^B \underline{g}_E - \tilde{\omega}_B \underline{v}_B \\ I_B^{-1} \underline{M} - I_B^{-1} \tilde{\omega}_B I_B \underline{\omega}_B \end{bmatrix} \quad (18)$$

where  $\underline{F}$  and  $\underline{M}$  are the force and moment vectors due to aerodynamics and thrust effects, and  $(\sim)$  represents the cross-product equivalent operation. The aircraft mass is  $m$ , and the rotational inertia matrix is  $I_B$ . The cross product terms model the inertial couplings which are important in maneuvering flight.

The aerodynamic forces and moments are nonlinear functions of the state of motion of the aircraft and the control surface deflections. The thrust forces and moments (which are entirely within the plane of symmetry) are functions of the flight condition and throttle position. The following equations indicate the effects included in this model:

$$\underline{F} = \begin{bmatrix} q_\infty S C_x(\alpha, \beta, \bar{q}, \delta_s, \delta_{mf}, \delta_{sp}) \\ q_\infty S C_y(\alpha, \beta, \bar{p}, \bar{r}, \delta_{sp}, \delta_{ds}, \delta_r) \\ q_\infty S C_z(M, \alpha, \beta, \bar{q}, \delta_s, \delta_{mf}, \delta_{sp}) \end{bmatrix} + \begin{bmatrix} T(M, h, \delta_T) \cos \theta_T \\ 0 \\ -T(M, h, \delta_T) \sin \theta_T \end{bmatrix} \quad (19)$$

$$\underline{M} = \begin{bmatrix} q_{\infty} S b C_{\ell}(M, \alpha, \beta, \bar{p}, \bar{r}, \delta_{sp}, \delta_{ds}, \delta_r) \\ q_{\infty} S \bar{c} C_m(M, \alpha, \beta, \bar{q}, \delta_s, \delta_{mf}, \delta_{sp}, x_{cg}) \\ q_{\infty} S b C_n(\alpha, \beta, \bar{p}, \bar{r}, \delta_s, \delta_{sp}, \delta_{ds}, \delta_r, x_{cg}) \end{bmatrix} + \begin{bmatrix} 0 \\ z_T T(M, h, \delta_T) \\ 0 \end{bmatrix} \quad (20)$$

The quantities  $\theta_T$  and  $z_T$  are the thrust misalignment and moment arm, respectively. The functional relationships implied in Eqs. 19 and 20 are given primarily by tabular data, and the aircraft simulation uses an efficient linear interpolation routine to calculate the aerodynamic and thrust forces and moments at any specific state.

Control surface position limits are included in the aircraft model. First-order, rate-limited actuator models are used in preliminary testing, but are not included in most production aircraft simulations for reasons of simulation efficiency. This simplification should not have a significant impact on conclusions based on a comparison of different flight control techniques of comparable bandwidth. Table 10 lists the control channels and the displacement limits used in all the experiments reported in this chapter, along with the rate limits and actuator time constants that can be used.

### 3.2.2 ACM Pilot Model

The ACM pilot model contains an acceleration-oriented trajectory generator that describes the specific maneuver the pilot wishes to perform, and a set of piloting gains that translate the ACM trajectory into stick and rudder pedal displacements. Hence, this pilot model is a trajectory tracking pilot model. Alternatively, the ACM trajectory internal to the pilot model can be viewed as the maneuver the pilot must perform to accurately track a specific opponent's maneuver. The extension

TABLE 10  
CONTROL CHANNEL DETAILS

T-3115

CONTROL	POSITION LIMITS	RATE LIMIT	TIME CONSTANT
Throttle, $\delta_T$	0 to 2 units	0.4 unit/sec	0.5 sec
Stabilator, $\delta_s$	-30 to 10 deg	30 deg/sec	0.05 sec
Maneuver Flap, $\delta_{mf}$	0 to 10 deg	30 deg/sec	0.05 sec
Spoiler, $\delta_{sp}$	-55 to 55 deg	250 deg/sec	0.05 sec
Differential Stabilator, $\delta_{ds}$	-12 to 12 deg	30 deg/sec	0.05 sec
Rudder, $\delta_r$	-30 to 30 deg	30 deg/sec	0.05 sec

of this model to include a target model, tracking kinematics and fight dynamics is possible but unnecessarily complex for the purposes of the tests reported in this chapter

The ACM trajectory generator commands consist of the three components of earth relative acceleration expressed in wind axes ( $\dot{V}_c$ ,  $a_{yc}$ ,  $a_{nc}$ ) and the component of body angular rate along the velocity vector ( $p_{wc}$ ). Wind axes consist of an x-axis along the velocity vector and a z-axis in the body x-z plane. The roll angle about the velocity vector between the wind z-axis and the vertical plane is denoted by  $\phi_v$ , which forms one of the ACM trajectory generator states. The others are velocity magnitude ( $V$ ), flight path angle ( $\gamma$ ), and velocity heading ( $\xi$ ). The nonlinear state equations that describe the trajectory generator dynamics are given in Eq. 21.

$$\begin{bmatrix} \dot{V} \\ \dot{\phi}_v \\ \dot{\xi} \\ \dot{\gamma} \end{bmatrix} = \begin{bmatrix} \dot{V}_c \\ p_{wc} + \xi \sin \gamma \\ (1/V \cos \gamma)(a_{nc} \sin \phi_v + a_{yc} \cos \phi_v) \\ (1/V)(a_{nc} \cos \phi_v - a_{yc} \sin \phi_v) \end{bmatrix} \quad (21)$$

Note again that  $a_{nc}$  and  $a_{yc}$  are components of earth-relative acceleration, and differ from ideal accelerometer outputs in these axes by the acceleration of gravity.

The transformation of the trajectory generator outputs to stick and pedal deflections occurs by two routes, as illustrated in Fig. 20. The ACM commands themselves (accelerations and roll rate) provide pilot control deflections directly by way of the command/control pilot gain matrix. These inputs are "open-loop" in the sense that they do not depend on the actual aircraft path-following accuracy. These open-loop inputs will dominate the pilot's input over the short term and in very rapid maneuvers, such as a rolling reversal. Command/control gains for the ACM pilot model are derived primarily from the command/control steady-state  $\Omega$  matrices discussed in the previous chapter of this report. Some modifications to these gains were made based on initial simulation tests.

R-37885

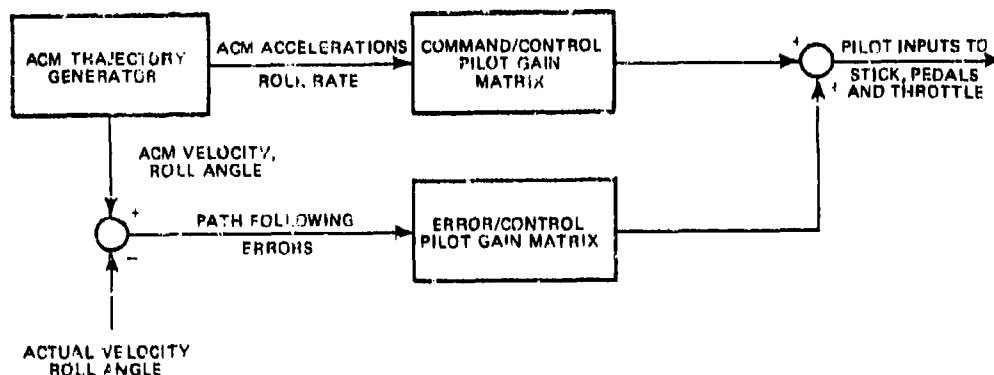


Figure 20 ACM Pilot Model

By differencing the ideal ACM velocity and roll angle  $(V, \phi_V, \xi, \gamma)_c$  with the actual aircraft values, the maneuver

errors can provide error-correcting pilot inputs (Fig. 20). In principle, velocity error drives throttle, roll error drives lateral stick, flight path angle error (transformed into aircraft axes) drives longitudinal stick and heading error (transformed into aircraft axes) can drive rudder pedal. In actual implementation in this study, since lateral acceleration (direct sideforce) is not within the capability of this airframe to any significant extent,  $a_{yc}$  is always zero, and sideslip error is used to drive rudder.

The error feedback gains are derived from the command gains by assuming a 2-sec time constant for error correction. Table 11 lists the pilot model gains for the high subsonic flight condition at which testing is performed. Note that the large throttle error gain is chosen so that the pilot model selects full afterburner early in an ACM maneuver, which minimizes energy loss. More detail concerning the rudder command gain is given in the results sections later in this chapter; the rudder input is necessary to roll the aircraft at

TABLE 11  
ACM PILOT MODEL GAINS

T-3116

CONTROL	COMMAND	ERROR	POSITION LIMIT
Throttle	4.5 units $\delta_T^*/g \dot{V}_c$	0.07 units $\delta_T/\text{fps } \Delta V$	0 to 2 units <sup>a</sup>
Longitudinal Stick	0.758 in $\delta_{lon}/g a_{nc}$	0.165 in $\delta_{lon}/\text{deg } \Delta \gamma$	-4.0 to 5.5 in, -10.2 cm to 16. cm
Lateral Stick	0.04 in $\delta_{lat}/\text{deg/sec } p_{wc}$	0.02 in $\delta_{lat}/\text{deg } \Delta \phi$	-4.5 to 4.5 in, -11.4 cm to 11.4 cm
Rudder	0.0 or 0.012 in $\delta_{ped}/\text{deg/sec } p_{wc}$	-0.1 in $\delta_{ped}/\text{deg } \Delta \beta$	-3.0 to 3.0 in, -7.6 cm to 7.6 cm

\* Throttle units 0.0: idle  
1.0: full military power  
2.0: full afterburner

high angle of attack with a conventional control system. The table also lists the pilot control deflection limits.

### 3.2.3 ACM Tracking Tasks

There are two tracking tasks used in this study, a wind-up turn and a rolling reversal. They are specified in terms of the velocity-axis accelerations and roll rates involved. Figure 21 illustrates the time history of the commanded wind-up turn. The commanded longitudinal acceleration is zero. This set of commands results in a rapid roll into a steady, high-g right turn followed, 10 sec later, by a rapid roll into a high-g left turn. The actual capabilities of the aircraft are such that this maneuver exceeds the steady turn rate at the flight condition chosen (800 fps TAS at 20,000 ft, 244 m/s at 6100 m). Hence, the aircraft will slow down in this maneuver and increasing  $\alpha$  will be required to maintain the high-g flight condition. The net effect of all this is that the bank-to-bank maneuver 10 sec into the trajectory will

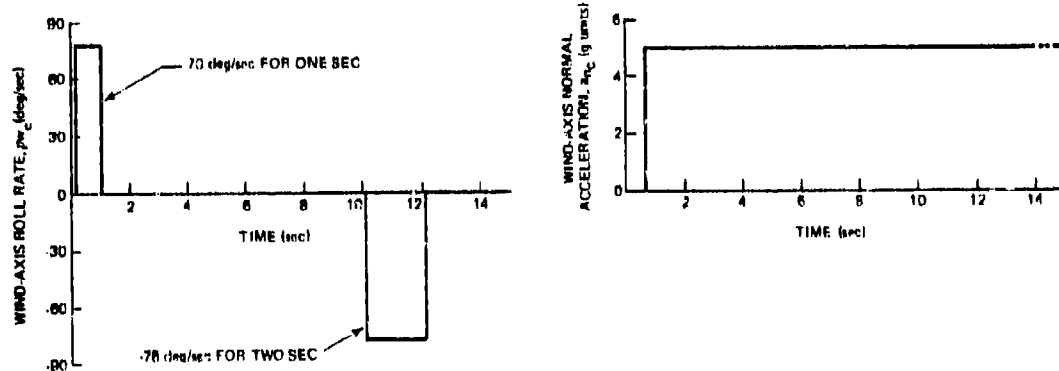


Figure 21 Wind-up Turn Trajectory Inputs



occur at high angle of attack. This maneuver is flown both by an open-loop pilot model (all error feedback gains set to zero) and a closed-loop pilot model, which includes all of the error feedback gains. The latter case is a form of target tracking. In all of these tests the roll command-to-rudder gain is zero.

The second maneuver used in these tests is described by the inputs illustrated in Fig. 22. This maneuver is called a rolling reversal, and is designed to convert ("reverse") a defensive tactical situation into an offensive one. The maneuver is a combination of high-g pull-up and 360 deg roll. The pull-up starts 1 sec before the roll. This combination results in a trajectory which rises sharply and then dives (by means of a sharp pull-up while rolling inverted) back to roughly the original trajectory. Since this is a "pre-programmed" maneuver, these tests are performed without any error feedback in the pilot model. This maneuver is so rapid that velocity changes are not as severe as in the wind-up turn. One difficulty in flying this trajectory involves the high angle-of-attack roll effectiveness of lateral stick in the conventional aircraft. It is low enough so that lateral stick alone will not lead to the completion of the maneuver. For this reason, the roll rate command-to-pedals gain is inserted in the ACM pilot model. The DFCS does not need the pedal input to follow this maneuver, as will be shown in Section 3.5.

### 3.3 CONTROL SYSTEM CANDIDATES

Three control systems are tested in the experiments reported in the following sections. Figure 19 shows that they all interconnect the pilot's control stick and pedals with the aircraft control surfaces. Throttle and engine control are not discussed further in this section, since the trajectories

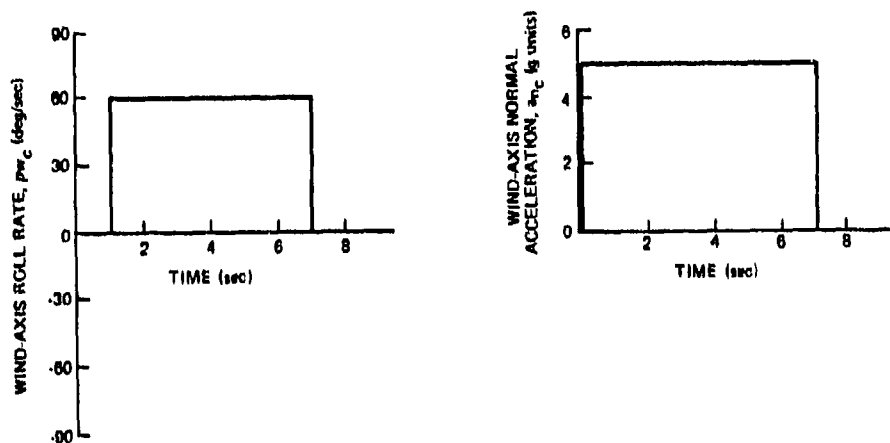


Figure 22 Rolling Reversal Trajectory Inputs

that are tested require full afterburner to minimize energy loss during the high-g maneuvers.

The conventional mechanical control system is illustrated in Fig. 23, and it consists of three separate channels. The pilot's lateral stick also drives the spoilers, and the maneuver flap is not deflected. The pitch and yaw sas actuators are limited-authority channels driven by washed-out rate feedbacks. Yaw sas also involves lateral acceleration feedback for turn coordination. The pitch sas limit is  $\pm 3$  deg stabilator, while the yaw sas limit used in this study is  $\pm 9.5$  deg rudder. The variable limit on pilot's rudder input is about  $\pm 15$  deg in the ACM flight condition.

The roll channel contains a rate feedback and a command augmentation feedforward. The pilot's differential stabilator can never be larger than  $\pm 7$  deg, but the roll cas can add up to 5 deg of differential stabilator to this. Hence,

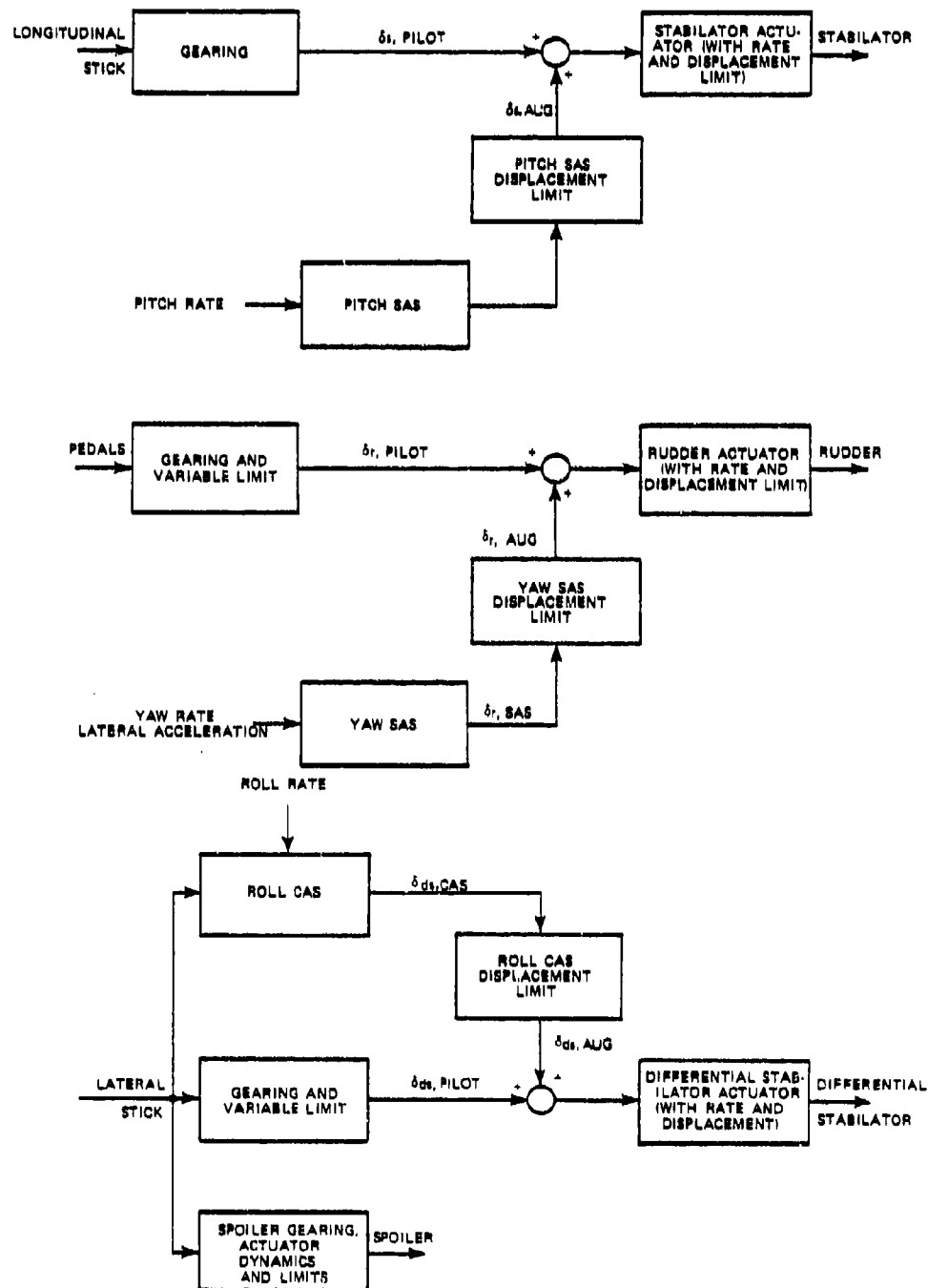


Figure 23 Conventional Control System

neither the pilot nor the cas have full differential stabilator authority, and in a case of roll cas failure or shutdown, the effective pilot roll control power (due to both the mechanical linkage and the roll cas) is reduced considerably. The roll cas signal is composed of a roll rate feedback and a lagged feedforward of pilot lateral stick. This roll command augmentation produces high effective pilot roll control power while avoiding the large roll accelerations that would result if the mechanical channel had full differential stabilator authority. Any or all of the three independent sas channels can be turned off.

The inputs to the analog sas computer consist of normal and lateral acceleration and the roll, pitch and yaw angular rates. Later modifications to the conventional control system (described in Ref. 21 but not modeled here) also use angle of attack and Mach number to schedule automatic maneuver flap and aileron-rudder interconnect. The nose probe that senses angle of attack can also sense sideslip, although this capability is not presently utilized. Another input to the sas computer is pilot lateral stick position, which drives the roll cas lag compensation. The outputs from the analog sas computer are commands to the rudder, stabilator and differential stabilator sas actuators.

Another of the flight control system candidates is the full-authority digital flight control system (DFCS), described in Chapter 2. As illustrated in Fig. 24, all control calculations occur in a digital flight computer (actually a set of parallel computers for reliability reasons) and the outputs command full-authority actuators for stabilator, maneuver flap, spoiler, differential stabilator, and rudder. The command inputs are pilot longitudinal and lateral stick position and rudder pedal position, which are interpreted in the

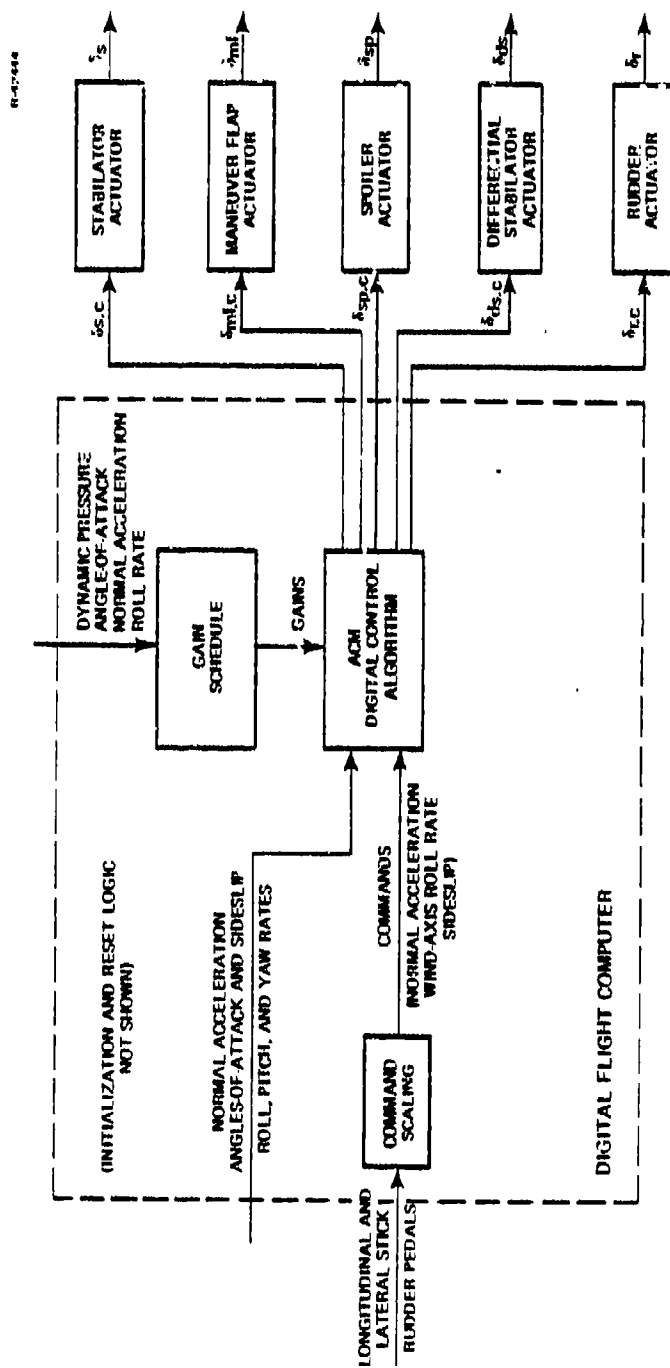
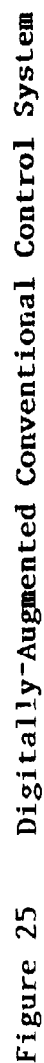


Figure 24 Digital Flight Control System

flight computer as commands of normal acceleration, roll rate about the velocity vector and sideslip. Although these pilot-control-to-command relations would be scheduled with flight condition in an actual implementation, they are fixed for the purposes of this study at 1.32g's/in, 25 deg/sec/in and -10 deg/in respectively. The inputs to the digital flight computer are similar to those available to the conventional analog sas computer in that normal acceleration, angle of attack, and roll, pitch and yaw rates are needed. Additionally, sideslip is required for the control algorithm and dynamic pressure is needed for gain scheduling. In principle, sideslip command and feedback can be eliminated in favor of lateral accelerometer feedback and lateral specific contact force command, resulting in inputs essentially identical to those used by the conventional control system.

The third control system tested in the ACM experiments is a digitally-augmented conventional control system, and it is illustrated in Fig. 25. In this control system, the conventional mechanical linkages between pilot and control surface main actuators are unchanged, and the limited-authority sas actuators are retained. The sas computer, however, is digital and contains as a subprogram the complete digital flight control system described above. The sas actuator commands are calculated by subtracting the pilot's mechanical linkage control surface command from the DFCS control surface command, much as is done in the present ARI design for the F-14A (Ref. 22). In the absence of control signal limiting effects, the main actuator command signal is identical to the DFCS actuator command signal. The value of such a control system is obvious in the context of a retrofit program, and the reliability and redundancy issues are more akin to those involved with conventional control systems. The basic question to be answered about a digitally-augmented system is whether



**Figure 25 Digitally-Augmented Conventional Control System**

the limited-authority sas channels are sufficiently powerful to improve the aircraft command response to a level approaching the full-authority DFCS.

Testing of the conventional control system and the DFCS against each other is described in the following two sections, and the performance of the digitally-augmented conventional control system is examined in Section 3.6.

### 3.4 TRAJECTORY TRACKING IN THE WIND-UP TURN

The wind-up turn maneuver implemented here involves a rapid roll into a steady right turn, followed 10 sec later by a roll to a steady left turn. Although maximum thrust is applied, the aircraft slows, which requires higher  $\alpha$  to hold the large normal acceleration. The emphasis in this test is on tracking accuracy, so a closed-loop pilot model is used. As discussed in Section 3.3.1, this pilot model attempts to null trajectory following errors by moving the stick and pedals in response to these errors. The pilot's roll rate-to-rudder gain is zero for these wind-up turn experiments.

Two control systems are tested: the conventional mechanical control system (sas off) and the full-authority DFCS. The command responses of the DFCS are illustrated by Fig. 26, which shows that the aircraft response to the step commands of  $a_n$  and  $p_w$  is rapid and does not exhibit excessive overshoot. The response settling is very good. Although the sideslip command is zero, there is a significant response during the initial roll and pull-up. The sideslip settles quickly to the steady value after the initial transient, and exhibits very little oscillation. Note that the structure of the DFCS is such (Fig. 20) that the command trajectories are proportional



to the pilot's control inputs. The normal acceleration and wind-axis roll rate command inputs come from longitudinal and lateral stick respectively, and sideslip command comes from rudder pedals. The angle-of-attack response is also included in Fig. 26 to show its rapid yet well controlled character. Note that as speed drops during the maneuver, angle of attack is increased by the DFCS to hold the commanded normal acceleration.

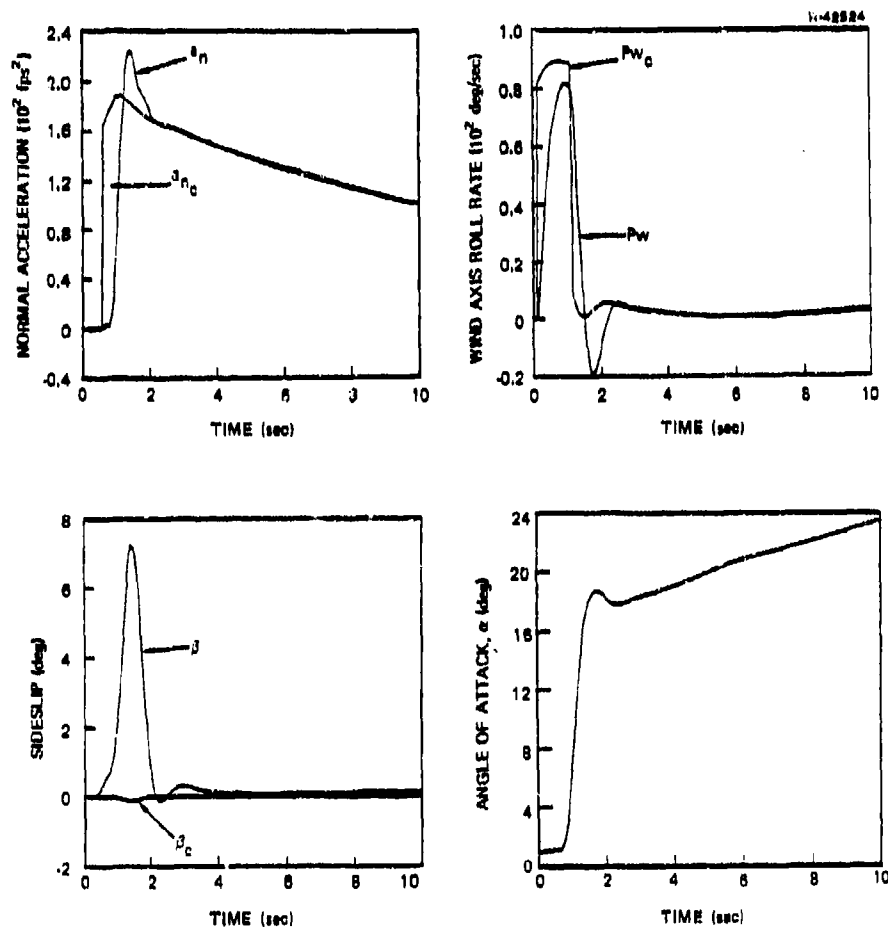


Figure 26 DFCS Command Response in the Wind-up Turn

The aircraft control surface motions that cause this response are shown in Fig. 27. The rapid stabilator and maneuver flap movement initially cause the rapid response noted above, yet both control surfaces are quickly reduced to lower values representative of the steady-state turn. Note that full maneuver flap is used to produce maneuver quickening. Later in this maneuver, the stabilator deflection is increased to achieve higher angle of attack. The controller also deflects maneuver flap to assist holding normal acceleration as speed is reduced. Hence, the DFCS includes an automatic maneuver flap feature. Differential stabilator is commanded to its limit as the aircraft rolls into the turn, and then quickly is reduced to a low value. Some motion is necessary to damp the Dutch roll oscillation, which in this aircraft involves significant roll motion (Ref. 23). Rudder motion serves to damp sideslip motion, and spoiler deflection is relatively small and hence not shown here.

The same ACM pilot model flying the same airframe in the same maneuver with a conventional mechanical control system (sas off) achieves much different results. Figure 28 compares roll angle responses. The poor Dutch roll damping of the conventionally-controlled aircraft is apparent. The sideslip response (Fig. 29) confirms this. The initial sideslip pulse is similar to that observed for the DFCS aircraft (Fig. 26), but the Dutch roll that the sideslip pulse excites lasts much longer than for the DFCS aircraft. The angle-of-attack response shown in Fig. 29 should be compared to that shown in Fig. 26; this comparison shows the low-overshoot and well-damped nature of the DFCS response. Note that the constant  $\alpha$  characteristics of the conventional control system is not necessarily a negative attribute; the conventional control system is approximately an angle-of-attack command system, and the pilot is expected to compensate for the loss of normal acceleration at a given  $\alpha$  as the speed decreases.

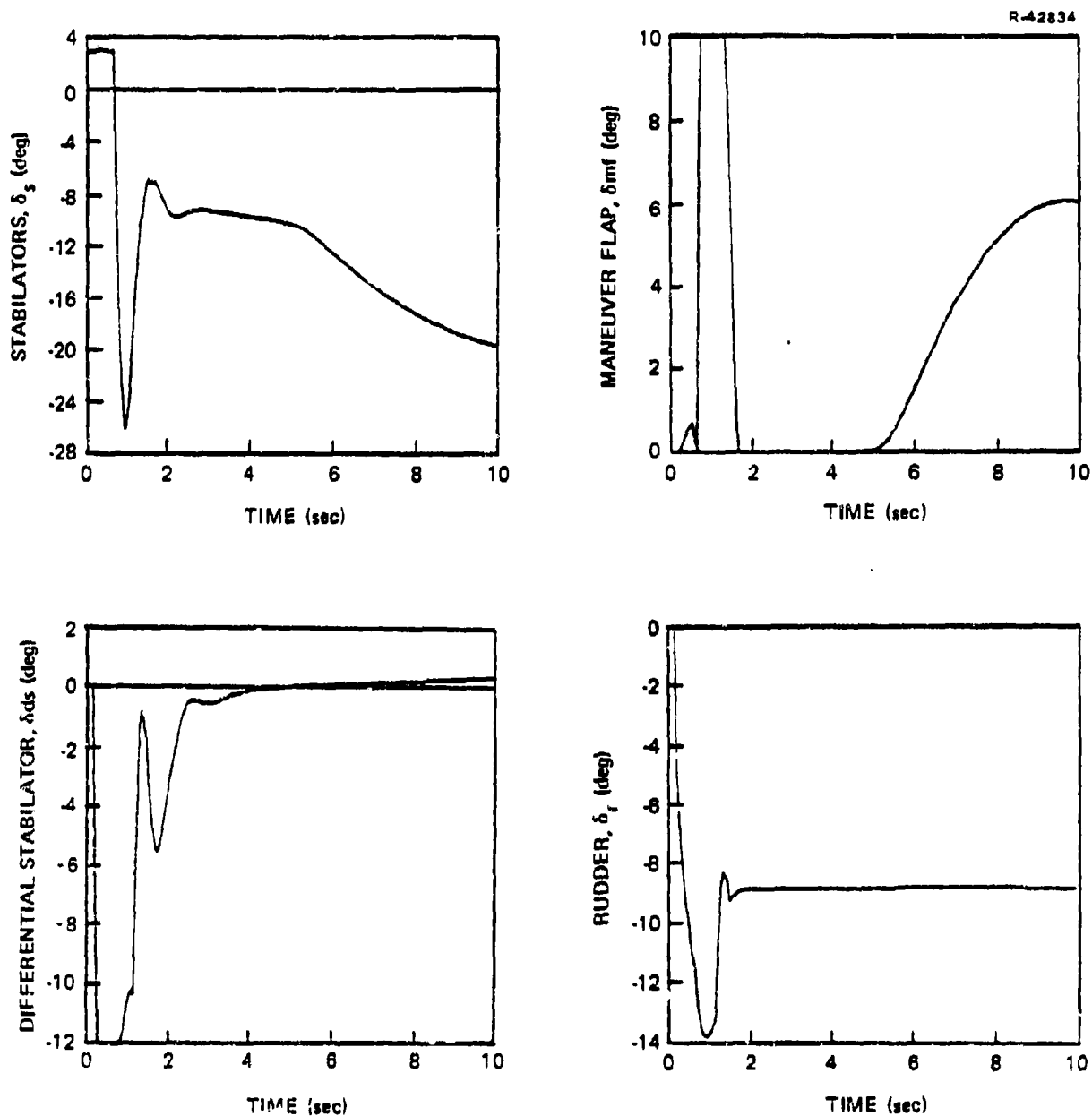


Figure 27 DFCS Control Surface Trajectories in the Wind-up Turn

The stabilator trajectories that result from the conventional control system are shown in Fig. 30, and these are proportional to the pilot model's control stick inputs. Especially apparent is the pilot model's attempt to reduce the

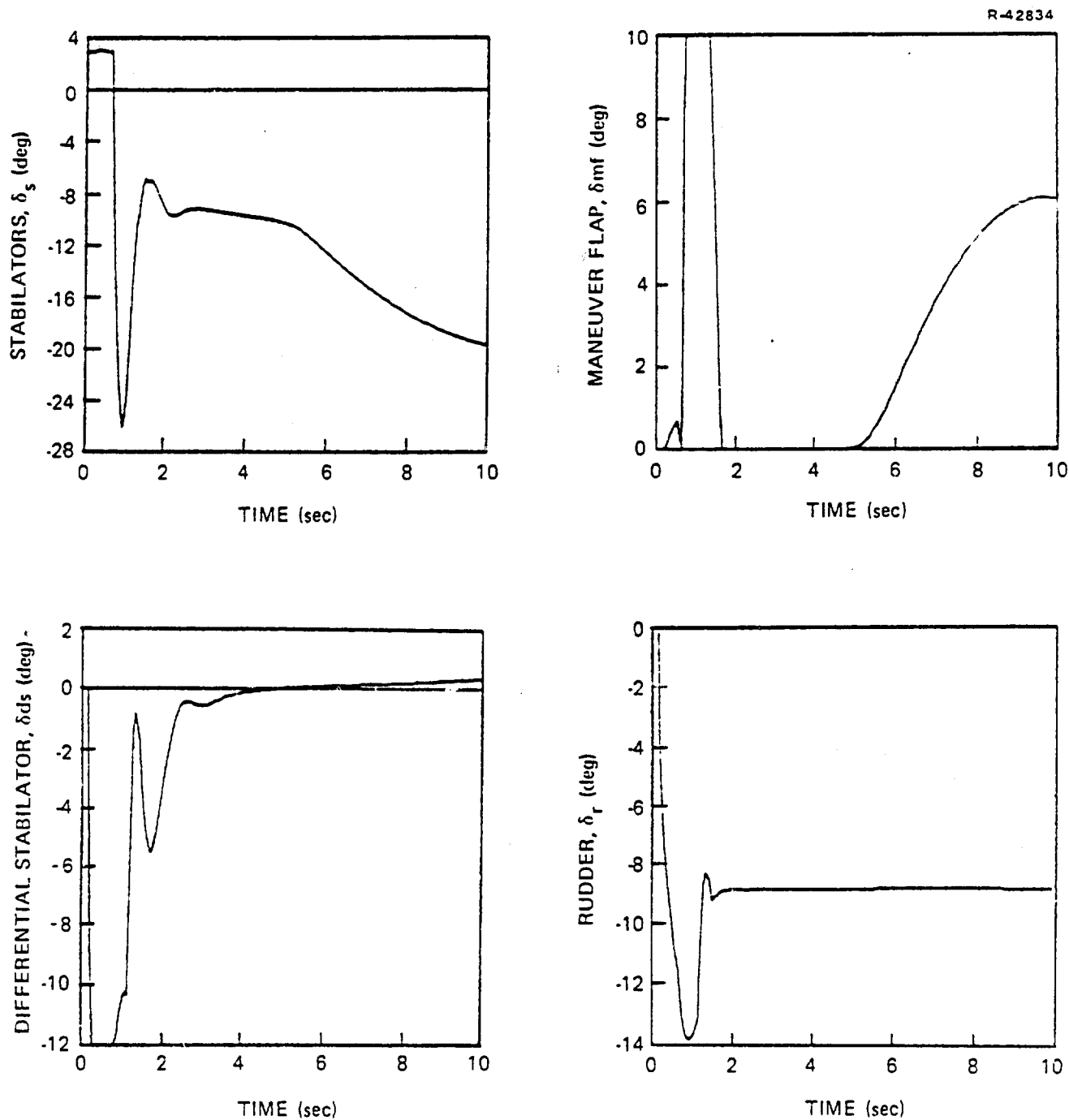
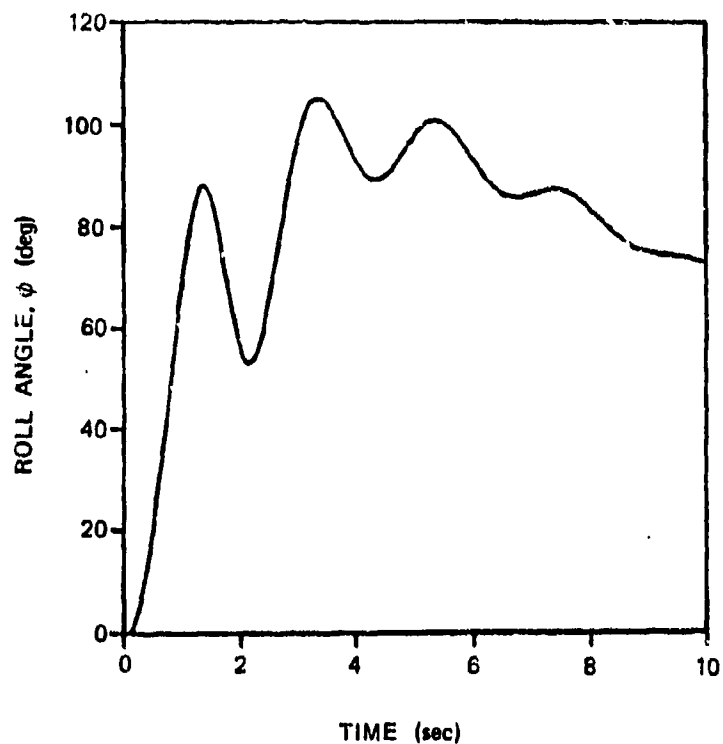
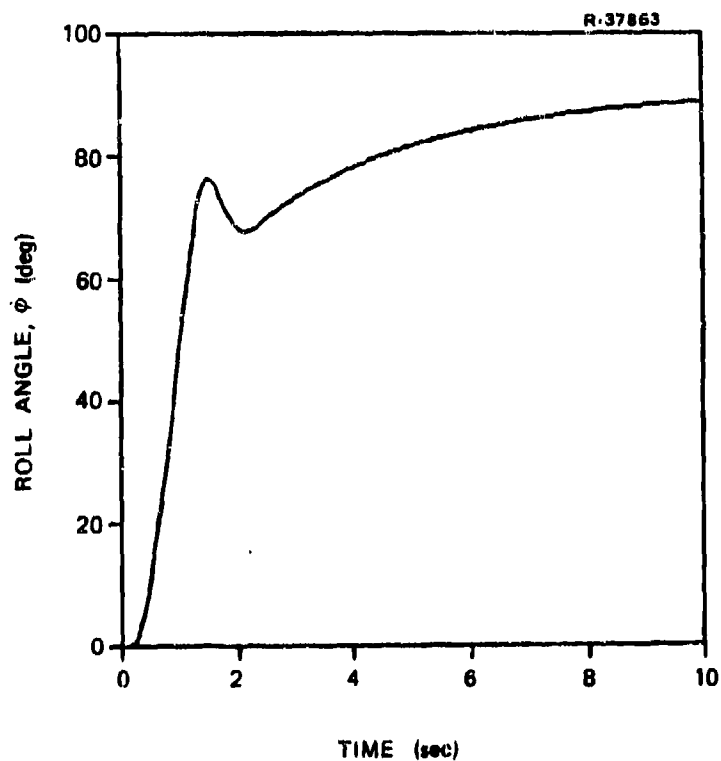


Figure 27 DFCS Control Surface Trajectories in the Wind-up Turn

The stabilator trajectories that result from the conventional control system are shown in Fig. 30, and these are proportional to the pilot model's control stick inputs. Especially apparent is the pilot model's attempt to reduce the



a) Conventional Mechanical Control System



b) Full Digital Flight Control System

Figure 28 Roll Angle Comparison for the Turn Entry

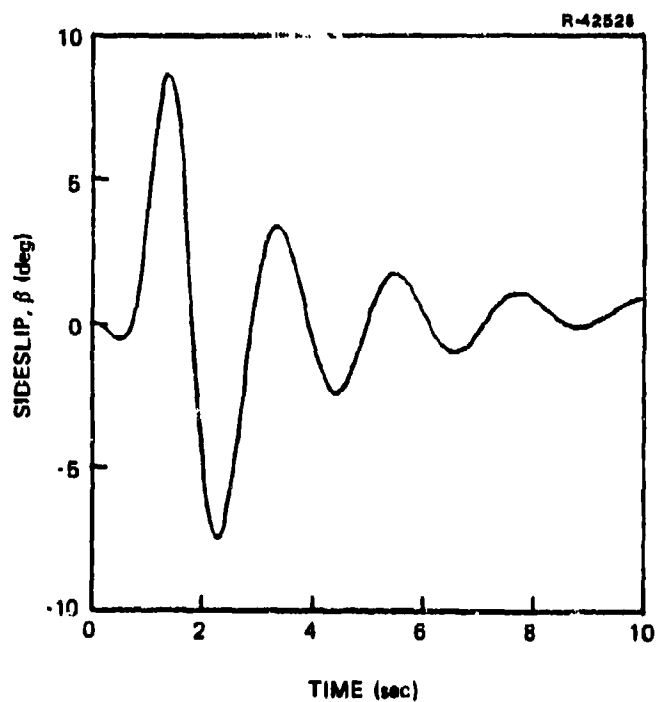
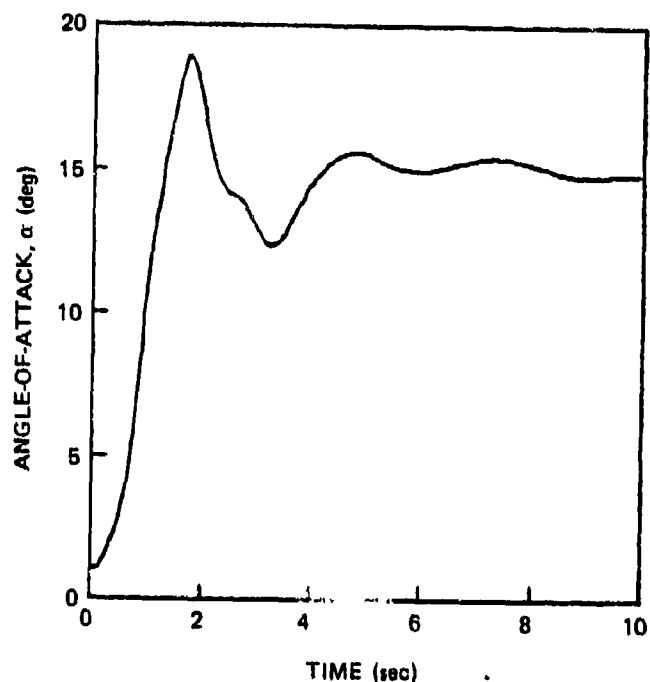


Figure 29 Aerodynamic Angle Response of the Conventional Control System (sas Off)

poorly-damped Dutch roll response by using lateral stick (differential stabilator). If this short-term compensation task can be performed automatically, the pilot could devote more attention to target tracking.

All of the previous plots deal with the turn entry and steady right turn during the first 10 sec of the trajectory. At 10.1 sec, the pilot model attempts to roll the aircraft to a left bank, and this roll input occurs at high angle of attack for both control systems. Speed has dropped from the maneuver entry speed of 0.77 Mach to 0.62 for the conventionally-controlled aircraft and speed has dropped to 0.47 Mach for the DFCS aircraft, due to its higher and more accurate normal acceleration response, which has unavoidably produced higher drag. Indeed, the DFCS aircraft reaches the aircraft pitch performance boundary soon after the left roll is initiated because stabilator goes to its aircraft-nose-up limit. The aircraft remains well controlled about the other axes, however, and even angle of attack exhibits only a mild oscillatory response around 31 deg  $\alpha$ . The roll to the left bank (Fig. 31) is sluggish due to the low velocity but occurs accurately. The mild oscillations in roll are probably due to the small uncontrolled  $\alpha$  oscillations.

The same maneuver (entered at somewhat lower angle of attack) in the conventionally-controlled aircraft results in a control-induced departure and incipient spin. Angle of attack is oscillatory and approaches 50 deg. Among the best indications of the departure are the plots shown in Fig. 32, where body yaw rate is rapidly increasing. The accompanying roll angle trajectory shows that the aircraft initially rolls left, as desired, but rapidly snap-rolls to the right through more than 360 deg. This undesired motion is caused by the pilot lateral stick input which drives differential stabilator.

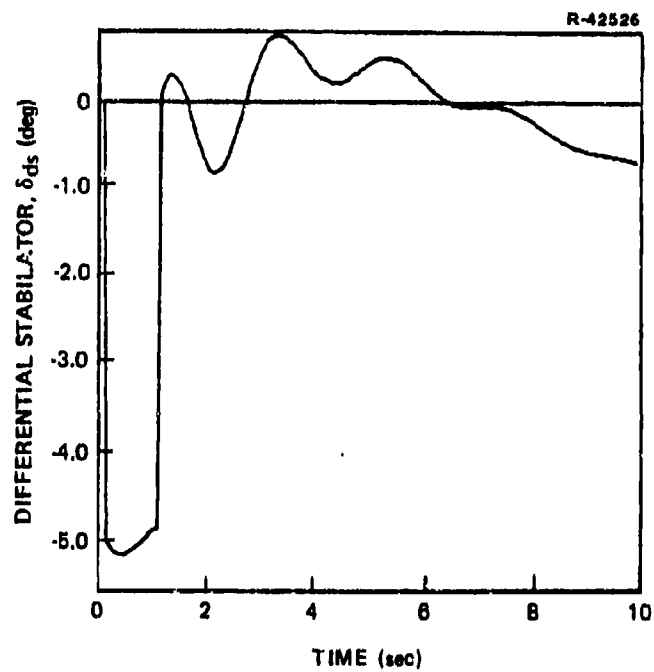
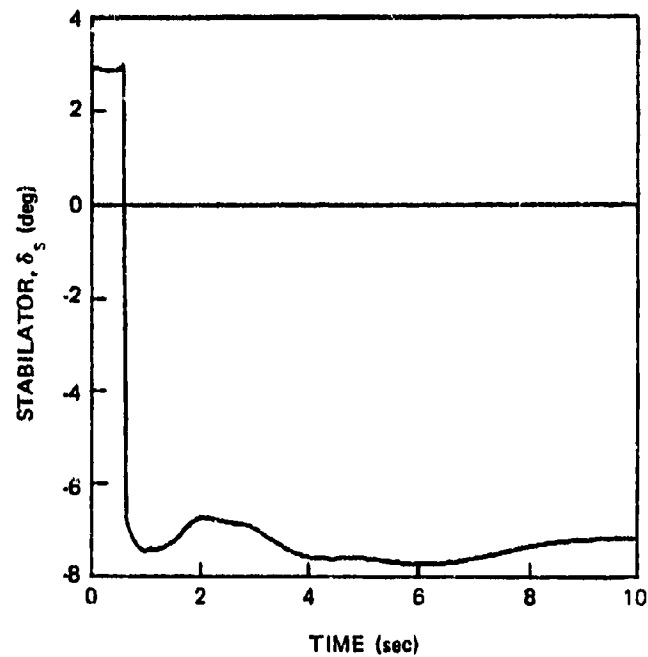


Figure 30 Stabilator Time Histories For a Conventionally-Controlled Aircraft in a Wind-up Turn



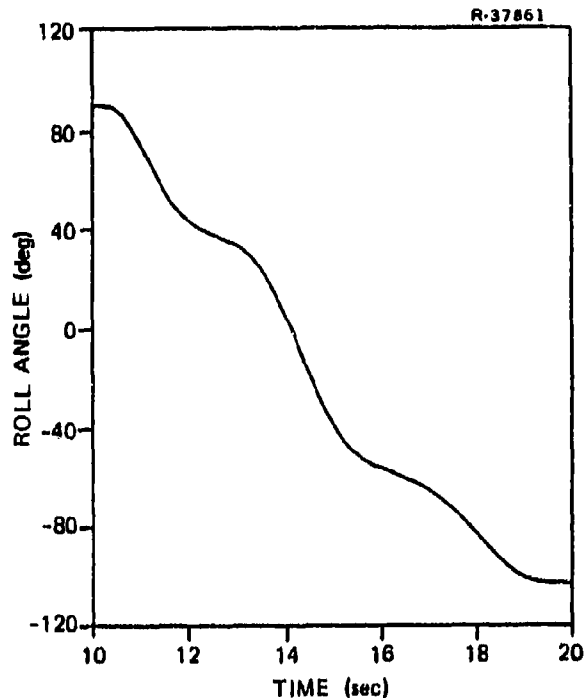


Figure 31 DFCS Aircraft in Bank-to-Bank At High Angle of Attack

At high  $\alpha$ , this produces roll and yaw moments of the opposite sign (in this case left roll moment and right yaw moment), whereas roll and yaw moments of the same sign are necessary to successfully roll about the velocity vector. The adverse yaw response causes the undesired snap roll. There is no indication at 20 sec that the pilot has recovered control of the aircraft, and altitude is being lost at 16,000 feet per minute (81 m/s).

The DFCS has enabled the pilot model to fly the aircraft right up to its performance boundary without experiencing a departure from controlled flight. Besides expanding the useful performance region, this has a significant impact on

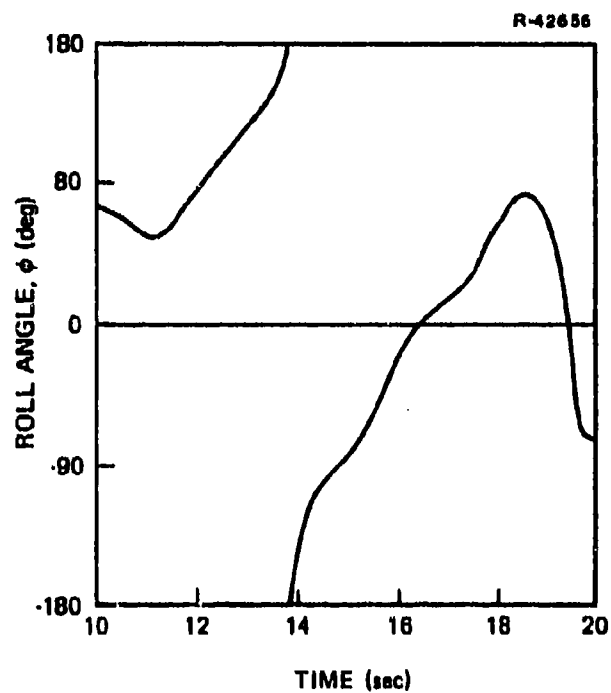
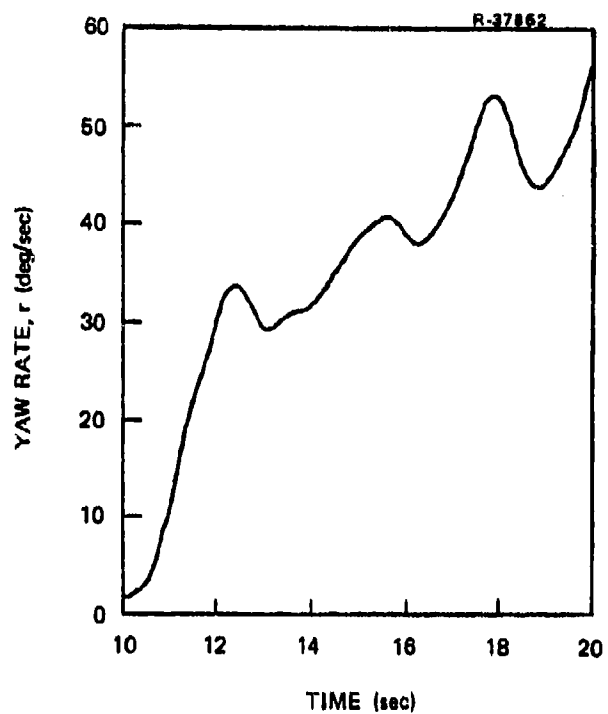


Figure 32 Control Induced Departure for Conventional Control System

pilot confidence and pilot training. With the conventional control system, the departure shown here can be avoided if the pilot learns to center lateral stick at high angles of attack. Even if the pilot could remember to do this along with his other ACM tasks, it is not clear he has sufficient information on which to change his control strategy. The DFCS assumes this task, allowing the pilot to prosecute the ACM task with improved concentration.

### 3.5 ACCURACY IN THE ROLLING REVERSAL

The rolling reversal is an air combat maneuver designed to convert ("reverse") a defensive tactical situation to an offensive one. The maneuver is a combination of a high-g pull-up accompanied by a 360 deg roll. Since it is a "pre-programmed" maneuver, these tests are performed without any error feedback in the pilot model. The maneuver is so rapid that velocity changes are not as severe as in the wind-up turn.

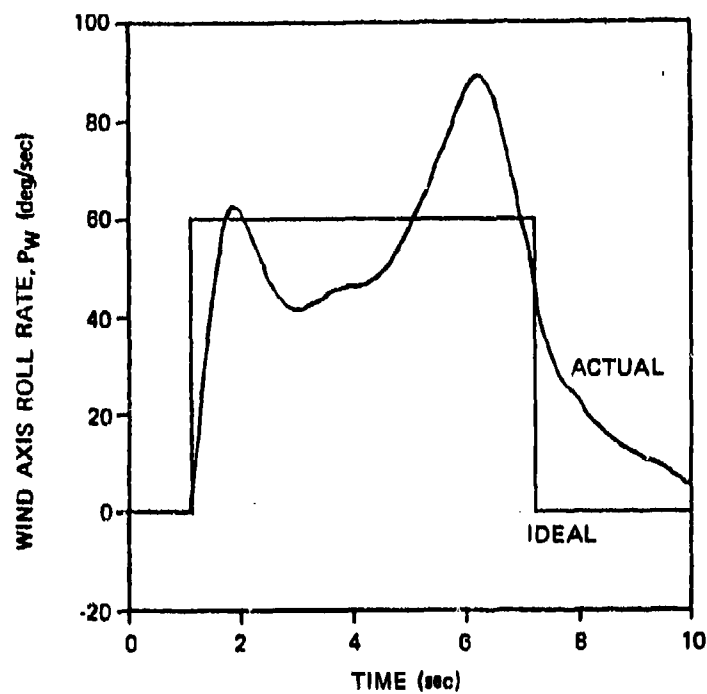
As discussed in Section 3.3.3, initial tests indicated that the conventionally-controlled aircraft cannot execute this maneuver with only lateral stick input due to the low rolling moment at high  $\alpha$ . For this reason, the roll rate command-to-pedals gain is inserted in the ACM pilot model. The DFCS does not need pedal input to follow this maneuver, and testing indicates that the only effect of the extra pedal input is a significant increase in sideslip (since pedal is the DFCS sideslip command channel). Hence, in the comparison presented here, the DFCS pilot model is simpler than the pilot model flying the conventional aircraft. In the following comparisons, the conventional aircraft has all three sas channels on.

The roll rate accuracy through the 360 deg roll is shown in Fig. 33. The conventional sas results in only a  $\pm 20$  deg/sec accuracy to the 60 deg/sec command, with a significant attitude effect apparent, i.e., the roll rate drops as the aircraft is inverted. The DFCS roll rate lies within  $\pm 4$  deg/sec of the command, even though rapid changes in the flight condition (roll rate and normal acceleration) are taking place. The end of the maneuver is much more rapid and accurate for the DFCS aircraft, whereas the conventionally-controlled aircraft roll response tails off slowly. This will produce a roll angle error which the open-loop pilot model is not set up to correct.

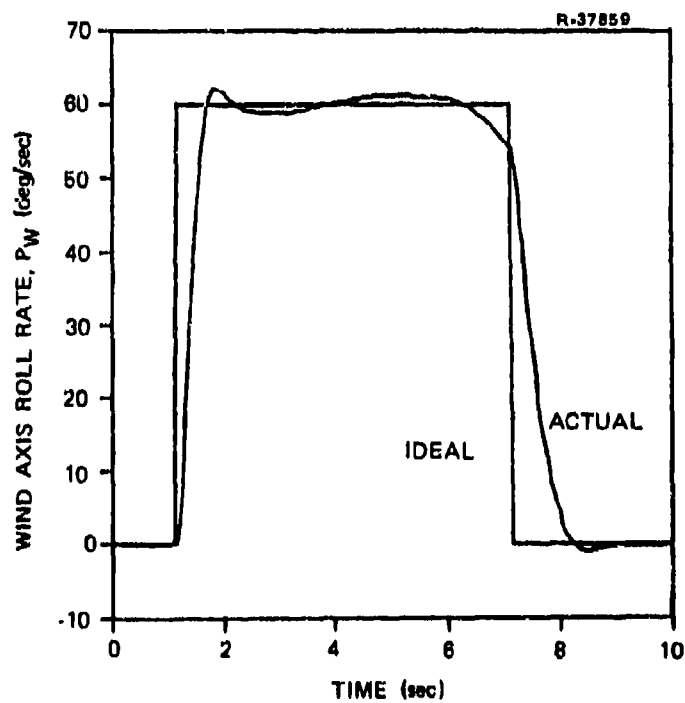
The longitudinal responses are compared in Fig. 34, which shows that the conventional sas response and the DFCS response are quite similar. The DFCS produces a somewhat more even angle-of-attack trajectory and, due to this, a much better normal acceleration response. The increase in angle-of-attack at the end of the roll compensates for the loss in velocity that has occurred during the maneuver.

Yaw rate magnitudes produced by the two control systems are comparable, although the DFCS produces much better sideslip control, as illustrated by Fig. 35. Sideslip transients are reduced to about a quarter of the value caused by the conventionally controlled aircraft. There is no significant steady-state value for the DFCS response, whereas the conventional sas allows about a 2 deg average sideslip during the 60 deg/sec roll.

The rudder deflections which produce these responses are shown in Fig. 36, where the pilot rudder input (due to the pilot model's internal roll rate-to-pedal gain) is apparent in the conventional sas trajectory. The stability augmentation system countermands the pilot input early in the roll, which

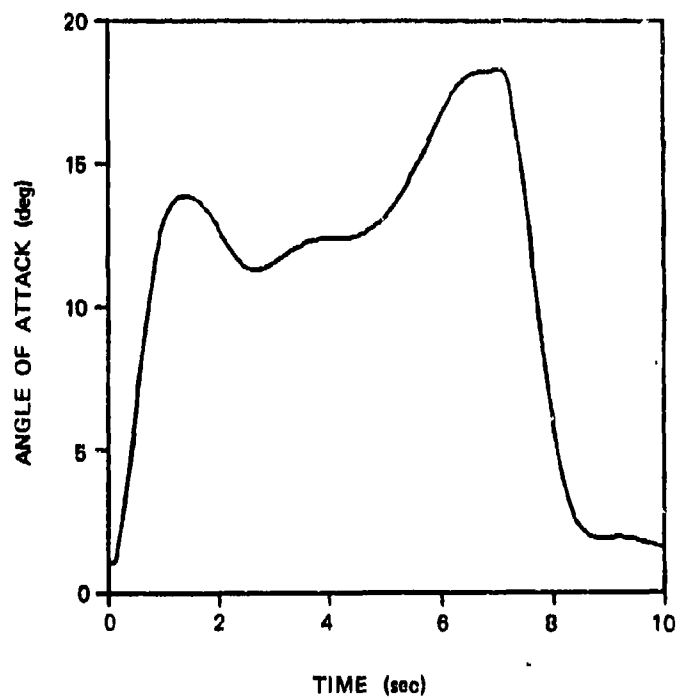


a) Conventional Sas

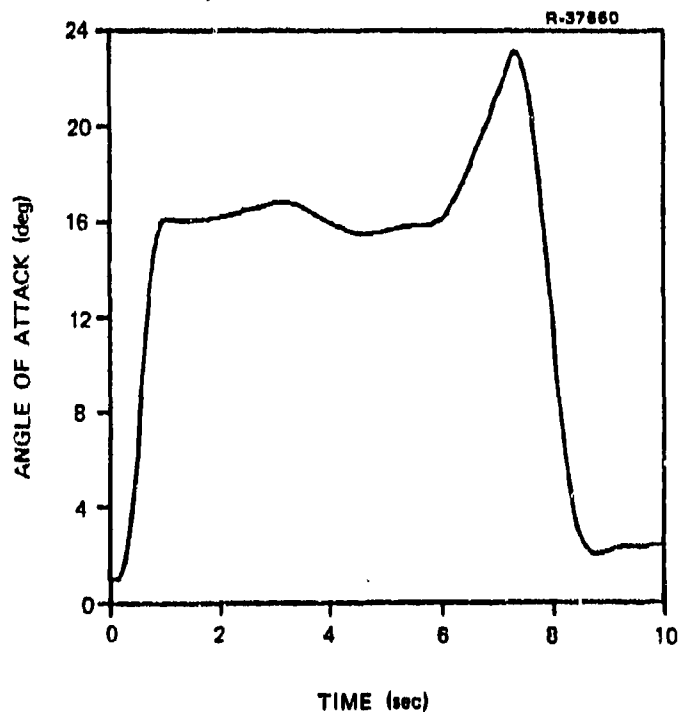


b) Full Digital Flight Control System

Figure 33 Roll Rate Accuracy in the Rolling Reversal

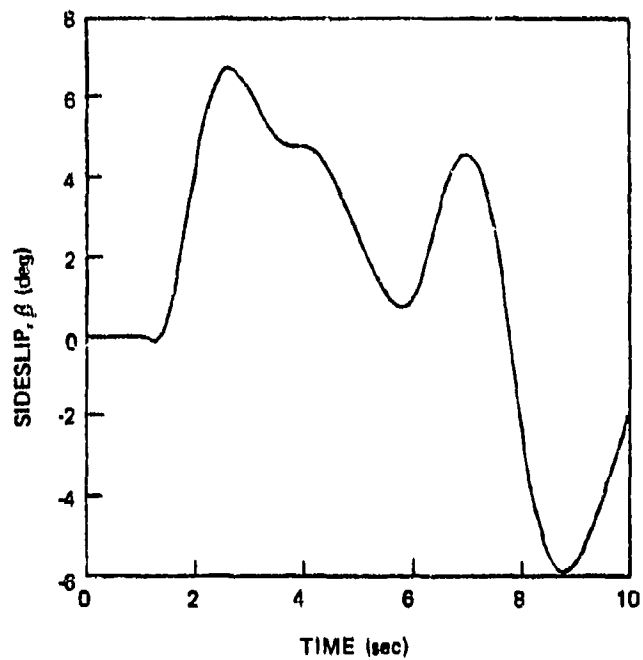


a) Conventional Sas

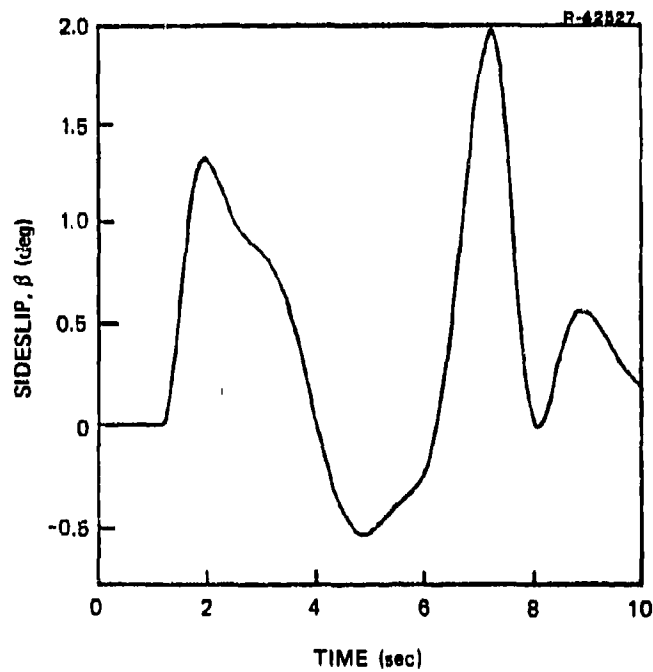


b) Full Digital Flight Control System

Figure 34 Angle of Attack Response in The Rolling Reversal

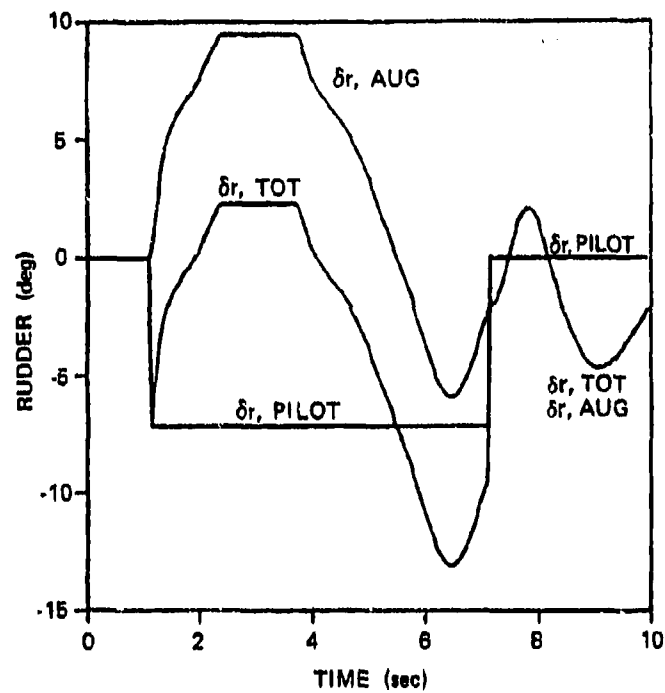


a) Conventional Control System - Sas On

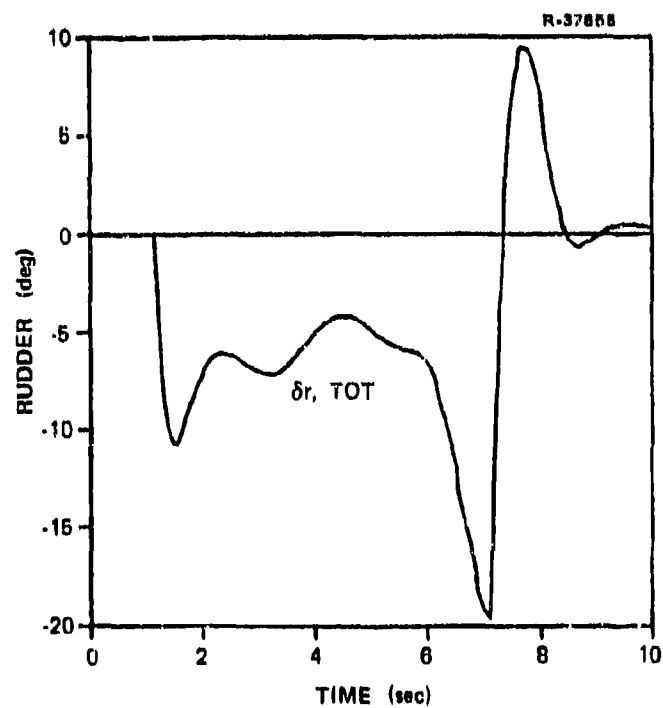


b) Digital Flight Control System

Figure 35 Sideslip in The Rolling Reversal



a) Conventional Sas



b) Full Digital Flight Control System

Figure 36 Rudder Time Histories in the Rolling Reversal



causes the total rudder deflection to be fairly small. During the latter half of the roll, the augmentation signal is reduced and assists the pilot in completing the maneuver. The DFCS rudder trace is also shown, and its similarity to the actual rudder deflection due to the pilot and conventional sas is notable. This ruder deflection produces much better sideslip control, as noted above, and is generated by the DFCS from lateral stick input only. No pilot rudder pedal input is necessary to produce proper roll response and accurate sideslip control in the DFCS aircraft.

### 3.6 DIGITALLY-AUGMENTED CONVENTIONAL CONTROL SYSTEM

During the test program, it became apparent that a promising control system modification approach could involve the retention of the conventional mechanical linkages, but with digital control of the existing, limited-authority sas actuators. Ideally, this control system would possess all of the response advantages of the full-authority DFCS but would be implementable in existing aircraft by replacing the analog sas computer with a digital one. As a preliminary test of the response of such a system, the control system implementation shown in Fig. 22 is chosen. The DFCS control laws are identical to those tested in the previous sections, and the sas actuator commands are formed by subtracting the pilot control command from the DFCS control command. Hence, for stabilator, differential stabilator, and rudder, the actual control surface deflection approximates the DFCS control command. Of course, if the difference between the pilot control signal and the DFCS control signal is greater than the sas actuator authority, this property is lost. Additionally, the DFCS maneuver flap and spoiler signals are not used; maneuver flap is held at zero and spoiler is tied to lateral stick with no bias input.

Finally, it should be noted that the DFCS control law does not include control position resets calibrated to the limited authority sas actuators.

The digitally-augmented conventional control system is tested in the rolling reversal, and hence the results are to be compared to those presented in Section 3.5. Roll rate response accuracy, shown in Fig. 37 significantly exceeds that of the aircraft with conventional sas during most of the maneuver, although it is not as good as the full-authority DFCS.

During the last 1.5 sec of the roll (5.5 sec to 7.0 sec) the roll rate drops dramatically from its commanded value of 60 deg/sec. Noting that this part of the roll occurs at high  $\alpha$  and that rudder is especially effective in rolling the airplane at high  $\alpha$ , it is concluded that the 9.5 deg rudder sas limit used in this simulation is not large enough to complete this maneuver. This is confirmed by noting that the control systems tested in Section 3.5 used 13-18 deg of rudder at this point in the maneuver (see Fig. 36). The roll rate "bounce" from 7 to 8.5 sec is due to the lack of proper DFCS control reset. It is expected that tailoring the control resets to the sas actuator limits can eliminate this "bounce" without affecting the rest of the response. Angle of attack response is similar, with accuracy better than a conventional sas but not as good as the full-authority DFCS. An undesired transient at the end of the trajectory is apparent here also. It is expected that the use of maneuver flap for longitudinal response quickening can improve the speed and accuracy of a digitally-augmented conventionally-controlled aircraft.

Sideslip response is shown in Fig. 38, where it is apparent that the initial sideslip transient is almost as well

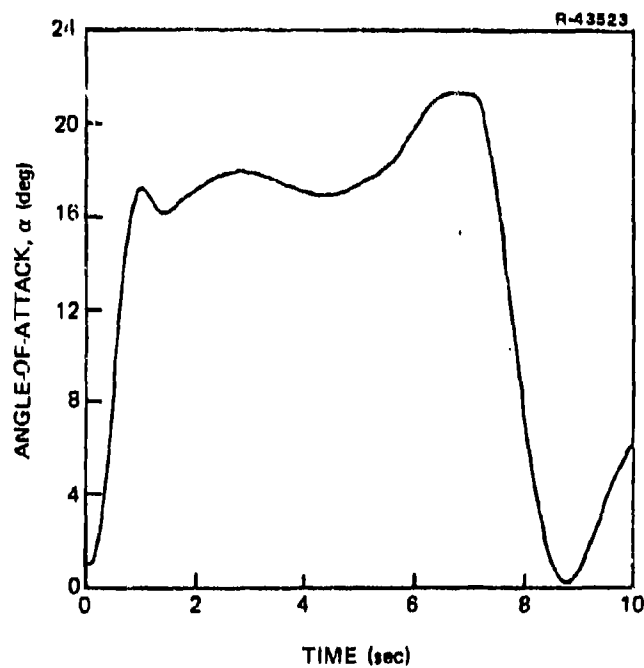
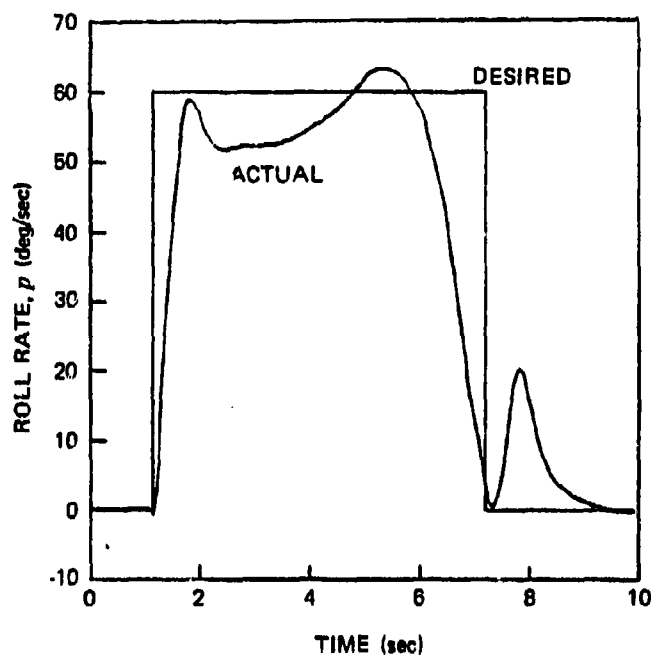


Figure 37 Digitally-Augmented Conventional Aircraft in the Rolling Reversal - Roll Rate and Angle of Attack

controlled as in the DFCS aircraft. The large spike as the aircraft stops rolling at 7 sec can possibly be reduced by proper calibration of the digital augmentation control resets. The rudder response, also shown in Fig. 38, illustrates that the 9.5 deg rudder sas limit greatly restricts the yaw channel of the digital augmentation system. The general rudder response, however, is quite similar to that achieved by the full-authority DFCS, as can be seen by comparing Fig. 36 and 38. Interestingly, the yaw sas limit on the actual aircraft has been expanded to 19.0 deg (Ref. 24) so a digitally-augmented aircraft with this larger yaw sas limit could probably match the accuracy of the DFCS quite well.

The rolling reversal trajectory is flown by the pilot model without roll rate command-to-pedal interconnect; hence, the pilot does not provide any pedal input. The rudder deflection shown in Fig. 38 is entirely due to the digital augmentation, which essentially operates as an aileron-rudder interconnect in this application.

### 3.7 CHAPTER SUMMARY

The improvements in handling qualities in the ACM regime that a DFCS offers are demonstrated in this chapter. They are accomplished by simulating both the ACM-oriented DFCS design and a conventional aircraft control system with the nonlinear 6-DOF aircraft model and the ACM pilot model. The test results specifically show that the DFCS offers a more accurate, better-controlled aircraft response along the two typical ACM trajectories simulated. In one case, the DFCS accurately controlled the aircraft right up to its performance

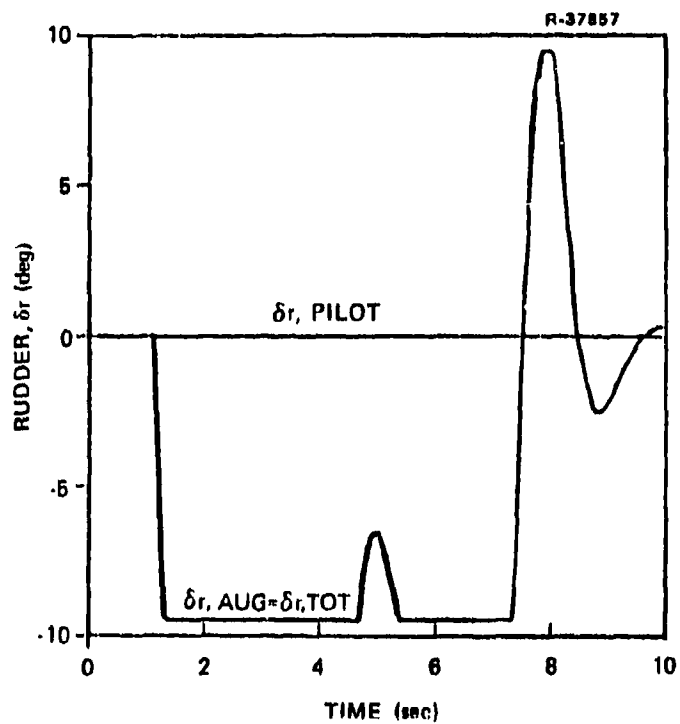
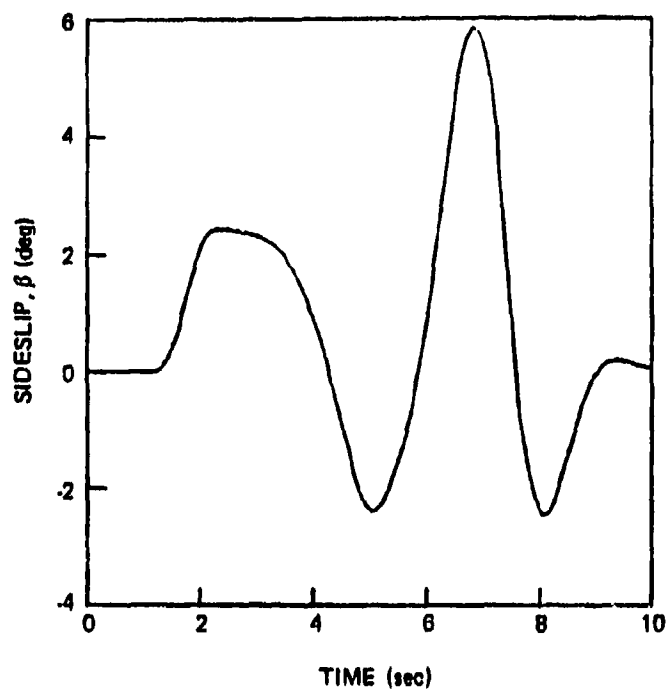


Figure 38 Digitally-Augmented Conventional Aircraft in the Rolling Reversal - Sideslip and Rudder

boundary, while the conventionally-controlled aircraft departed from controlled flight. Preliminary testing of a digital augmentation system indicates that it offers many of the same stability and control improvements as the full DFCS, while operating through existing sas channels. The DFCS design methodology demonstrated in this chapter is directly applicable to the design of command augmentation systems for advanced vehicle configurations such as highly-maneuvering and CCV aircraft.

4.

#### PILOT MODEL HYPOTHESIS TESTING

##### 4.1 INTRODUCTION

During rapid maneuvering, an aircraft's dynamic characteristics can change markedly in a matter of seconds. Hence, as the aircraft maneuvers, the pilot may be called upon to change his control strategy dramatically in order to maintain aircraft stability. Usually, the pilot has mastered the necessary procedural adaption needed to perform the maneuver and executes it with precision. On some occasions, even the skilled pilot may experience difficulty, perhaps adapting his control strategy to suit poorly chosen criteria, or possibly not adapting at all. In high-performance aircraft, this apparent lapse can cause a pilot-induced "departure", i.e., a loss of control which, if not corrected immediately, can lead to a spin and possible loss of aircraft. An example of a spin departure is shown in Fig. 32 for the case where a simple closed-loop system is chosen to resemble a pilot's outer loop control behavior; this simple pilot model does not adapt as the aircraft executes a wind-up turn. The problem of interest becomes one of determining if more complex pilot models can be used to model and understand the pilot's discretionary behavior in departure-prone maneuvering tasks.

In two previous reports, Refs. 3 and 23, the optimal control pilot model has been employed to address this problem using the F-14A fighter aircraft. The optimal control pilot model is a complex optimal control system which has been shown to capture the fundamental aspects of a human operator's control behavior (Refs. 26 and 27). The optimal control pilot

model is determined by minimizing a quadratic cost function in the presence of noise subject to a human's physical limitations and perceptions. Section 4.2 reviews the components of the optimal control pilot model used in this study.

In Ref. 23, investigations are conducted using the optimal control pilot model and F-14A along the demanding, wind-up turn maneuver previously mentioned. It is determined in Ref. 23 that if a pilot attempts to control an unstable system optimally, there are levels of system instability beyond which the pilot loses control. In many cases, a human is physically incapable of controlling systems with substantial instabilities. Reference 23 also shows that the optimal control pilot model exhibits similar difficulties and can predict when a pilot will lose control due to excessively severe aircraft instabilities.

A sequence of flight conditions are specified along a wind-up turn maneuver for the F-14A in Ref. 23 and optimal control pilot models are determined at each flight condition. The pilot models have no difficulty in stabilizing the aircraft, indicating that controlling the F-14A along a wind-up turn is within the physical capabilities of a pilot if the pilot adapts correctly to the flight condition of the aircraft. As the maneuver progresses, however, Ref. 23 demonstrates that there is a dramatic variation in the optimal piloting strategy, including in some cases, a change in sign of the pilot's stabilizing commands to the aircraft.

To determine if the pilot model control strategy required to complete a maneuver is somehow related to known pilot-aircraft control difficulties, the pilot model's control strategy is fixed in Ref. 23 at a low angle of attack flight condition (10 deg) and the aircraft dynamics are varied in sideslip,  $\beta_0$ .



and angle of attack,  $\alpha_0$ , along a wind-up turn maneuver. Varying sideslip is shown to have no effect on stability for a non-adapted pilot model; but, when the aircraft's angle of attack is increased beyond about 16 deg, closed-loop pilot-aircraft instabilities occur in the form of a lateral divergence. The onset of the instability is shown in Ref. 23 to coincide with the change in sign of the optimal adapted pilot model control gains. The pilot model results give the indication that if the pilot uses a low angle of attack control strategy in high angle of attack flight conditions, pilot control difficulties will result.

Continuing with the concept of the pilot incorrectly adapting to the aircraft's flight condition, Ref. 3 varied the pilot model's adaptation point over a number of flight conditions in a wind-up turn maneuver. Five important results about pilot-aircraft stability were obtained: (1) If the pilot is controlling the bare airframe\* using only lateral stick, the pilot-aircraft system will depart from controlled flight if the pilot remains adapted to any low  $\alpha_0$  (below 12 deg  $\alpha_0$ ) flight condition while the aircraft flight condition exceeds 16  $\alpha_0$ ; (2) If the pilot attempts to compensate for control difficulties at 16 deg  $\alpha$  and adapts by using a high  $\alpha_0$  control strategy in a low  $\alpha_0$  flight condition, the aircraft again can go unstable because of improper pilot control behavior; (3) The pilot model analysis did show, however that the pilot can compensate for control difficulties beyond 16 deg  $\alpha_0$  without adapting by using lateral stick and pedals; (4) Even if the pilot uses stick and pedals, pilot-aircraft instabilities still occur beyond 25 deg  $\alpha_0$  if the pilot model keeps a low  $\alpha_0$  control strategy; and (5) If the pilot uses only pedal to control the

---

\*The F-14A stability augmentation system (Sas) is off and an aileron-rudder interconnect system (ARI) is not operating.

lateral-directional dynamics of the aircraft, then the pilot model analysis in Ref. 3 shows the pilot-aircraft system remains stable for any mismatch between the pilot model adaptation point and the aircraft's flight condition up to the limit of angle of attack variation tested ( $30 \text{ deg } \alpha_0$ ). Of course, this does not indicate that the aircraft can be flown in ACM with only pedals, but only that stability would not be in question if only pedals are used.

All of these results concerning pilot model-aircraft stability agree with observed behavior of a human pilot flying the bare airframe F-14A aircraft based upon comparisons with piloted-simulation results and discussions with NASA Langley personnel (Ref. 28).

The conclusions just described indicate that a properly designed aileron-rudder interconnect system would probably cure the high  $\alpha$  departure problem, and allow the pilot to use a low  $\alpha$  piloting strategy at all angles of attack. An initial F-14A ARI design, which essentially eliminates pilot differential stabilator input at high  $\alpha$ , while phasing in a lateral stick-to-rudder crossfeed, is tested in Ref. 3 and 23 using the optimal control pilot model. The pilot model analysis shows that the ARI eliminates the lateral divergence instability but introduces a new and different instability characterized as a growing oscillation in the lateral modes, particularly in the sideslip angle. The piloted F-14A at high angle of attack with the ARI on has a pilot induced oscillation problem (Ref. 29) very similar to the instability predicted by the optimal control pilot model analysis.

The remarkable ability of the optimal control pilot model to predict instabilities of the actual pilot-aircraft system is qualitative rather than quantitative. Time-domain

comparisons of the predicted output of the pilot model and the measured output of the actual pilot in a tracking situation are not performed in Refs. 3 and 23. Agreement between the pilot model and actual pilot time histories is judged by examining time histories of pilot control difficulties and determining if the observed difficulties agree with the stability results computed in Refs. 3 and 23. It is the purpose of this chapter to perform a rigorous analysis of the aircraft control time history predicted by the optimal control pilot model and the measured control time history of a pilot flying the F-14A in a wind-up turn tracking task.

The method used to perform the analysis is a hypothesis testing scheme developed in Refs. 30 and 31 and briefly outlined in Section 4.3 and Appendix C. Given a set of hypothesized mathematical models used to represent a physical system, the hypothesis testing scheme can determine which model best matches the measured output of the physical system. To use the hypothesis testing approach with the optimal control pilot model, a sequence of pilot models is constructed at flight conditions along the wind-up turn maneuver. The pilot models are thereby adapted to the angle of attack of the flight conditions used for their construction. Thus, there can be a low- $\alpha_0$  control strategy pilot model and a high- $\alpha_0$  control strategy pilot model. A pilot model's control strategy is determined by the feedback gain the optimal control pilot model produces at the flight condition.

Recently, other researchers have been investigating the concept that the human's model of the system under control and the actual system model do not necessarily agree. The human's model of the system under control is termed the "internal model", (Refs. 32 to 35). Henceforth, instead of saying that the pilot model is nonadapted, the pilot model will be said to have an incorrect internal model of the aircraft

dynamics. A low- $\alpha_0$  pilot model means the internal model of the aircraft used to construct the pilot model is obtained at a low- $\alpha_0$  flight condition.

The first step in the hypothesis testing procedure is the construction of a finite set of pilot models, each with a different internal model representation of the aircraft. Then the output of each pilot model is compared with the human data to determine which model best predicts the actual pilot response. The output of the hypothesis testing scheme is the probability,  $P_{H,i}$ , that pilot model  $i$  best matches the data. The hypothesis testing scheme will determine if the pilot does not adapt to varying aircraft flight conditions by indicating only one pilot model has a high probability of matching the data.

The hypothesis testing scheme is very general and does not have to be restricted to investigating only situations where the pilot models internal model of aircraft varies. Section 4.4, for example, validates the hypothesis testing scheme using synthetic data by constructing a set of pilot models which differ from each other in key pilot model parameter values. One of the hypothesized pilot models is used to generate the data in a monte carlo simulation and the hypothesis testing scheme correctly identifies this pilot model as the one which best matches the data.

The actual piloted data used in the hypothesis testing scheme for the F-14A aircraft is obtained from NASA Langley aircraft simulation tests using their Differential Maneuvering Simulator (DMS). The DMS consists of an enclosed hemispherical screen within which a pilot sits in a cockpit mock-up. He views a computer generated display of a tracking situation on the screen. The pilot generates control commands which drive the computer model of the aircraft. The computer portrays the resulting aircraft motions on the screen as viewed by the pilot.

Section 4.5 presents time histories of the aircraft states and controls which result during the DMS tracking engagement under investigation. Section 4.6 presents the internal model representation of the tracking dynamics used in constructing the optimal control pilot models. Appendix A gives a detailed derivation of these equations of motion. Section 4.7 discusses the variables which are perceived by the pilot and modeled in the pilot model as the observations. Also given are the typical human parameters (perceptual time delay, neuromuscular time constant, etc. discussed in Section 4.3) used to construct the optimal control pilot model. The hypothesis testing results using the actual data are given in Section 4.8. The chapter is summarized in Section 4.9.

#### 4.2 OPTIMAL CONTROL PILOT MODEL WITH THE PADE APPROXIMATION

This section briefly reviews the elements of the optimal control pilot model to be used in hypothesis testing. The optimal control pilot model is based on the premise that a motivated, well-trained human controls a system optimally. To construct the pilot model, the assumptions needed to specify an optimal controller are formulated, then modified to reflect basic human characteristics and limitations. The pilot model assumptions are shown in Table 12. At chosen points along the wind-up turn maneuver under investigation, the pilot's internal model of the aircraft and target dynamics is represented as a linear, time-invariant system. The  $n$ -vector,  $\Delta \underline{x}(t)$ , represents the perturbation aircraft dynamics, aircraft sas, tracking error, and target states. The aircraft's stick inputs are represented by the  $m$ -vector,  $\Delta \underline{u}(t)$ ;  $\Gamma \Delta \underline{w}(t)$  is the pilot's internal model of white gaussian noise disturbance inputs.

TABLE 12  
PILOT MODEL ASSUMPTIONS

AIRCRAFT AND TARGET PERTURBATION STATE DYNAMICS	$\Delta \dot{\mathbf{x}}(t) = \mathbf{F} \Delta \mathbf{x}(t) + \mathbf{G} \Delta \mathbf{u}(t) + \mathbf{r}(t)$
PILOT OBSERVATIONS	$\Delta \mathbf{y}(t) = [\mathbf{H} \quad \mathbf{D}] \begin{bmatrix} \Delta \mathbf{x}(t-\tau) \\ \Delta \mathbf{u}(t-\tau) \end{bmatrix} + \Delta \mathbf{v}_y(t-\tau)$
PILOT COST FUNCTION	$J = E \left\{ \lim_{T \rightarrow \infty} \int_0^T \left( \begin{bmatrix} \Delta \mathbf{x}^T \Delta \mathbf{u}^T \end{bmatrix} \mathbf{Q}_C \begin{bmatrix} \Delta \mathbf{x} \\ \Delta \mathbf{u} \end{bmatrix} + \Delta \dot{\mathbf{u}}^T \mathbf{R}_L \Delta \dot{\mathbf{u}} \right) dt \right\}$
PILOT NEUROMUSCULAR DYNAMICS	$\Delta \dot{\mathbf{u}}(t) = -\mathbf{R}_L \Delta \mathbf{u}(t) + \Delta \mathbf{u}_c(t) + \Delta \mathbf{v}_u(t)$
PILOT NEUROMUSCULAR LAG	$\mathbf{R}_L = \begin{bmatrix} \frac{1}{\tau} & 0 & \dots & 0 \\ n_1 & & & \\ 0 & \frac{1}{\tau} & & \\ \vdots & n_2 & \ddots & \\ 0 & \dots & \dots & \frac{1}{\tau} \\ & & & n_m \end{bmatrix}$

The pilot is assumed to manipulate the aircraft controls so as to minimize the quadratic cost function shown in Table 12. The pilot minimizes the cost function using his perceptions of displayed information represented as the  $l$ -observation vector,  $\Delta \mathbf{y}(t)$ . As a physical limitation, the pilot has a perceptual time delay,  $\tau$ , which delays his observations. The pilot cannot physically observe the states perfectly, hence, a white, gaussian observation noise,  $\Delta \mathbf{v}_y(t)$  is added to the observations. The pilot manipulates the aircraft controls with his hand, hence, a neuromuscular dynamics model must be included. Weighting the control rate in the quadratic cost function causes the control solution to take the form required to model neuromuscular dynamics. The  $(m \times m)$  neuromuscular dynamics matrix,  $\mathbf{R}_L$ , in Table 12 is diagonal, with individual elements representing the inverse of human limb neuromotor time constants. The neuromotor dynamics are driven by the pilot's internal control commands,  $\Delta \mathbf{u}_c(t)$ , and by neuromotor noise represented as the white gaussian  $m$ -vector,  $\Delta \mathbf{v}_u(t)$ .

As discussed in Ref. 27, the pilot's observation noise covariance scales with the covariance of the states and controls, while the neuromotor noise scales with the covariance of the pilot's internal control commands. The covariances for  $\Delta v_y(t)$  and  $\Delta v_u(t)$  can be determined if the scaling factors  $P_{yi}$  and  $P_{ui}$  are specified, where  $P_{yi}$  is the pilot's noise-to-signal ratio for the  $i^{\text{th}}$  observation and  $P_{ui}$  is the pilot's noise-ratio for the  $i^{\text{th}}$  control.

To determine an optimal control pilot model, the following parameters discussed in the previous paragraphs and shown in Table 12 must be known for a given aircraft system:  $P_{yi}$ ,  $P_{ui}$ ,  $\tau$ ,  $R_L$ ,  $H$ ,  $D$ , and  $Q_c$ . All of these variables except  $Q_c$ ,  $H$ , and  $D$  have been measured experimentally, and typical ranges of their values can be found in the pilot model literature ( $P_{yi} = -20$  db,  $P_{ui} = -30$  db,  $\tau = 0.2$  sec,  $\tau_n = 0.1$  sec). When the pilot views motions in a display, as is the case for the DMS simulations, then the elements in  $H$  and  $D$  can be deduced from the states portrayed on the display screen. The values used for the state and control quadratic weights in  $Q_c$  remain the only unknown parameters needed to construct an optimal control pilot model. These weights model the pilot's trade-off of control effort against tracking accuracy. Three previous studies, Ref. 23, 36, and 37 aid in choosing  $Q_c$ . In Ref. 23, the pilot model's control strategy (i.e., pilot model-aircraft closed-loop eigenvalues) is shown not to be especially sensitive to the choice of  $Q_c$ . As long as reasonable values are chosen for the weighting elements, conclusions about pilot control strategy can be made with confidence. In Refs. 36 and 37, a tracking situation similar to the one developed in Section 4.5 is analyzed with the optimal control pilot model. Choices for the weighting elements in  $Q_c$  are given in Refs. 36 and 37 and are used as an aid in constructing the pilot model here.

It is also possible to use the hypothesis testing scheme to determine which quadratic cost function weighting matrix (tracking accuracy-control effort trade off) among a given set of weighting matrices best matches the actual pilot's control strategy. Section 4.5 shows hypothesis testing results for different cost function weighting matrices and serves to verify that the tracking accuracy-control effort trade-off assumed in this study closely approximates that actually practiced by the pilot.

The hypothesis testing scheme requires an analytic pilot model, hence, the pure time delay in the model is replaced by its Padé approximation. The Padé approximation allows the pilot model to be constructed as a linear, time-invariant model with the pure delay approximated by additional pilot model states. The solution to the optimal control problem posed in Table 12 with the pure time delay replaced by its Padé approximation is given in Ref. 23 and summarized in Table 13. A block diagram is shown in Fig. 39. The pilot's observations (2 in Table 13) are degraded by noise, then passed through a lead-lag network representing the Padé approximation. The resulting signal is processed by a Kalman filter (3 in Table 13) which generates a best estimate of the states, controls, and lagged observation states. The state estimates are multiplied by the feedback matrix,  $C$ , (4 in Table 13) to form the pilot's internal control command. The gain matrix,  $C$ , in the pure time delay and Padé approximation pilot models are the same. The pilot's internal control command,  $\Delta u_c(t)$  is the input to the neuromuscular dynamics model (5 in Table 13) from which the pilot's aircraft control,  $\Delta u(t)$  is generated and sent to the aircraft model's control actuators.

With the Padé approximation, the pilot model described in Table 13 and Fig. 39 can be written as



TABLE 13  
ELEMENTS OF THE PILOT-AIRCRAFT SYSTEM MODEL

T-3120

EQUATION	EQUATION PARAMETERS	RELATION TO PILOT PERFORMANCE
<p>1. Aircraft Dynamic Model Including Internal Target Model of Pilot and Tracking error dynamics:</p> $\Delta \dot{\underline{x}} = F \Delta \underline{x} + G \Delta \underline{u}$	<p><math>\Delta \underline{x}</math> Aircraft, target, and tracking error state variables</p> <p><math>\Delta \underline{u}</math> Aircraft control variables</p> <p>F Aircraft, target, and tracking error dynamics (stability derivatives and inertial coupling)</p> <p>G Aircraft control effects (sensitivity to control deflections)</p>	<p>Pilot must observe this well enough to command aircraft and to provide stability.</p> <p>Pilot must use this to command aircraft and to provide stability.</p> <p>Aircraft must be stable enough for pilot to control, subject to normal human capabilities</p> <p>Aircraft must respond to external commands in a way which the pilot can understand</p>
<p>2. Pilot's Cues:</p> $\Delta \underline{y} = H \Delta \underline{x} + D \Delta \underline{u}$ <p>Pilot's Cues Delayed by, <math>\tau</math>, using a Padé approximation</p> $\Delta \dot{\underline{z}} = -\frac{2}{\tau} \Delta \underline{z} + \Delta \underline{y} + \Delta \underline{v}_y$ $\Delta \underline{v}_E = -\Delta \underline{y} - \Delta \underline{v}_y + \frac{4}{\tau} \Delta \underline{z}$	<p>H State variable display selection and transformation</p> <p><math>\tau</math> Pilot time delay</p> <p>D Control variable display selection and transformation</p> <p><math>\Delta \underline{v}_y</math> Pilot induced zero mean gaussian noise in observations</p>	<p>Cues must be sufficient for command and stabilization.</p> <p>Noise in observation has direct effect on estimation performance of the pilot</p>
<p>3. Pilot Estimation Model with Padé Approximation:</p> $\Delta \dot{\underline{x}}_E = F_E \Delta \underline{x}_E + K(\Delta \underline{y}_E - H_E \Delta \underline{x}_E)$ $F_E = \begin{bmatrix} F & G & 0 \\ C & -R_L & 0 \\ H & D & [-\frac{2}{\tau}] \end{bmatrix}$ $H_E = \begin{bmatrix} -H & -D & [\frac{4}{\tau} \quad I] \end{bmatrix}$	<p><math>\Delta \underline{x}_E</math> State, <math>\Delta \underline{x}</math>, control, <math>\Delta \underline{u}</math> and perception-delay state, <math>\Delta \underline{z}</math>, variables estimated by pilot</p> <p><math>F_E</math> Dynamic model assumed (i.e., "learned") by the pilot including neuromuscular lags and perception time delays</p> <p>K Estimation gains which weight the difference between the pilot's observations and his prediction of pilot-aircraft response.</p> <p><math>\Delta \underline{y}_E</math> Pilot's delayed observation of motion, control, delay states</p> <p><math>H_E</math> Pilot's transformation of estimated variables to agree dimensionally with observations</p>	<p>Estimates of motion variables must be accurate enough to provide effective closed-loop control</p> <p>The better the pilot's knowledge of the aircraft and his own capabilities, the better he can cope with noisy measurements</p> <p>Less noise in the pilot's observation of cues leads to high K and more reliance on observed motions.</p> <p>Noise in observations has direct effect on estimation performance of the pilot.</p> <p>Pilot disorientation would degrade performance.</p>
<p>4. Pilot Control Model:</p> $\Delta \underline{u}_c = C \Delta \underline{x} + \Delta \underline{v}_u$	<p><math>\Delta \underline{x}</math> Subset of <math>\Delta \underline{x}_E</math> corresponding to aircraft target and tracking error motions</p> <p>C Control gains which transform pilot's estimates of aircraft motions to control actions</p> <p><math>\Delta \underline{v}_u</math> Pilot induced zero mean neuromotor gaussian noise.</p>	<p><math>\Delta \underline{x}</math> must be close to <math>\Delta \underline{x}</math> for precise, stable control.</p> <p>Pilot attempts to tradeoff aircraft motions and available control "power". Improper control strategy could degrade command response and destabilize the system.</p> <p>Reflects the fact that the pilot cannot estimate some of the states perfectly.</p>
<p>5. Pilot Neuromuscular Model:</p> $\Delta \dot{\underline{u}} = -R_L \Delta \underline{u} + \Delta \underline{u}_c$	<p><math>\Delta \underline{u}</math> Pilot model control output variables</p> <p><math>R_L</math> Neuromuscular lags</p> <p><math>\Delta \underline{u}_c</math> Pilot internal control commands</p>	<p>Aircraft control input</p> <p>Neuromuscular system smooths pilot outputs and could prevent pilot from stabilizing a fast instability.</p> <p>Result of conscious effort to provide "best" control.</p>

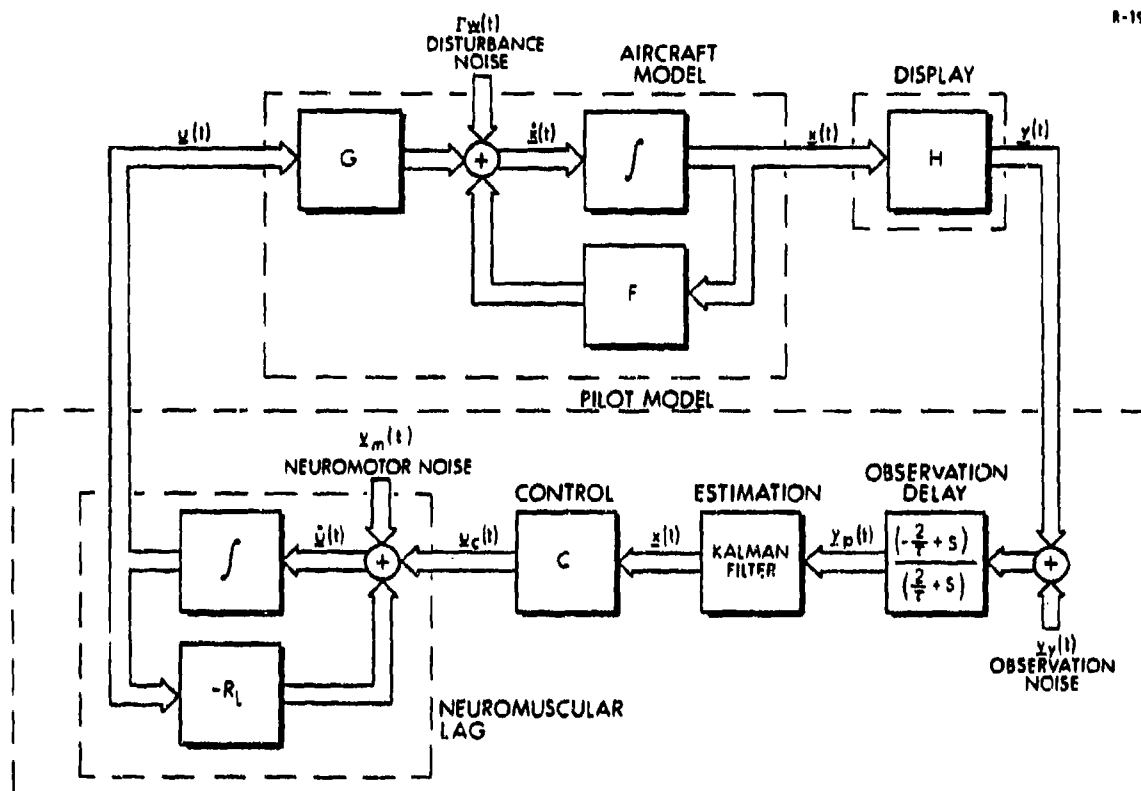


Figure 39 Block Diagram of the Pilot Model Containing the Padé Approximation to Pure Time Delay

$$\begin{bmatrix} \Delta \dot{\underline{u}} \\ \Delta \dot{\underline{\hat{x}}}_E \\ \Delta \dot{\underline{z}} \end{bmatrix} = \begin{bmatrix} -R_L & C & 0 & 0 & 0 \\ 0 & F_E - KH_E & \frac{4}{\tau} K & 0 & 0 \\ 0 & 0 & -\frac{2}{\tau} I & 0 & 0 \end{bmatrix} \begin{bmatrix} \Delta \underline{u} \\ \Delta \underline{\hat{x}}_E \\ \Delta \underline{z} \end{bmatrix} + \begin{bmatrix} 0 & \Delta \underline{v}_u \\ -K & \Delta \underline{y} + \Delta \underline{v}_y \\ 1 & \Delta \underline{v}_y \end{bmatrix} \quad (22)$$

In order to use Eq. 22 in hypothesis testing, a discrete version is necessary. Assuming that  $\Delta y$  remains constant over the sampling interval,  $\Delta t$ , Eq. 22 has the discrete representation

$$\Delta \underline{x}_{k+1} = \phi_{PM} \Delta \underline{x}_k + \Gamma_{PM} \Delta \underline{y}_k + \Gamma_W \Delta \underline{w}_k \quad (23)$$

where

$$\Phi_{PM} = e^{F_{PM}\Delta t}$$

$$\Gamma_{PM} = \int_0^{\Delta t} e^{F_{PM}t} dt K_{PM}$$

$$E \left\{ \Gamma_{W \underline{\Delta w}_k \underline{\Delta w}_k^T \Gamma_W^T \right\} = \int_0^{\Delta t} e^{F_{PM}t} Q_{PM} e^{F_{PM}^T t} dt = W_{PM}$$

$$\Delta \underline{x} = [\Delta \underline{u}^T, \Delta \hat{\underline{x}}_E^T, \Delta \underline{z}^T]^T$$

$$F_{PM} = \begin{bmatrix} -R_L & C & 0 & 0 & 0 \\ 0 & F_E - K H_E & & \frac{4}{\tau} K & \\ 0 & 0 & & -\frac{2}{\tau} K & \end{bmatrix}$$

$$Q_{PM} = \begin{bmatrix} V_u & 0 & 0 \\ 0 & K V_y K^T & -K V_y \\ 0 & -V_y K^T & V_y \end{bmatrix}$$

$$K_{PM} = \begin{bmatrix} 0 & -K^T & I^T \end{bmatrix}$$

$V_u$ ,  $V_y$  are the covariance matrices of the pilot's neuromotor noise  $\Delta \underline{v}_u$  and observation noise,  $\Delta \underline{v}_y$ , respectively. The matrix,  $K$ , is the pilot model's Kalman filter gain. The matrices  $K$  and  $C$  are determined by solving Riccati equations which depend on the pilot's internal model description of the aircraft (1 in Table 13). The pilot model is unadapted when the internal model description of the aircraft used to determine the pilot model is not the same as the mathematical model of the aircraft at the flight condition under investigation.

### 4.3 HYPOTHESIS TESTING

The hypothesis testing philosophy for investigating pilot control strategy is to construct a number of pilot models, each using an internal model of the aircraft at different points along the wind-up turn maneuver; then, determine which pilot model best represents the actual pilot control behavior. If the pilot does not adapt as the aircraft flight condition changes, then only one of the pilot models will best represent the data. If the pilot adapts then the hypothesis testing scheme will switch among the pilot models as the pilot's control strategy changes.

Mathematically, the hypothesis testing scheme is implemented by viewing each pilot model represented in Eq. 23 as a dynamic system whose input is the pilot observation vector,  $\Delta \underline{y}_k$ , with process noise,  $\Delta \underline{w}_k$ , and whose output is the pilot control vector  $\Delta \underline{u}_k$ . The measured output vector is the actual measured pilot control,

$$\Delta \underline{u}_{m,k} = [I \ 0 \ 0] \Delta \underline{x}_k + \underline{v}_k$$

$\underline{v}_k$  is a zero-mean gaussian measurement noise with covariance  $V$ . In the data from NASA Langley, the DMS measurement noise is essentially zero, but  $V$  is included here to keep the derivation general. A Kalman filter using the pilot model as the plant and the control measurements as the observation vector can be constructed as

$$\Delta \hat{\underline{x}}_k(+) = \Delta \hat{\underline{x}}_k(-) + K_H [\Delta \underline{u}_{m,k} - \Delta \hat{\underline{u}}_k(-)] \quad (24)$$

$$\Delta \hat{\underline{x}}_{k+1}(-) = \Phi_{PM} \Delta \hat{\underline{x}}_k + \Gamma_{PM} \Delta \underline{y}_k \quad (25)$$

$$K_H = P(-) \begin{bmatrix} I \\ 0 \\ 0 \end{bmatrix} \{ [I \ 0 \ 0] P(-) \begin{bmatrix} I \\ 0 \\ 0 \end{bmatrix} + V \}^{-1}$$

$$P(-) = \Phi_{PM} P(+) \Phi_{PM}^T + W_{PM}$$

$$P(+) = [I - K_H [I \ 0 \ 0]] P(-)$$

In this application, the above Kalman filter is assumed to be in steady state. If the pilot model is correct, the filter residuals

$$\Delta \underline{r}_k = [\Delta \underline{u}_{m,k} - \Delta \hat{\underline{u}}_k(-)]$$

are a zero-mean white gaussian noise sequence with covariance

$$E\{\Delta \underline{r}_k \Delta \underline{r}_k^T\} = [I \ 0 \ 0] P(-) \begin{bmatrix} I \\ 0 \\ 0 \end{bmatrix} + V = S \quad (26)$$

If the pilot model is not correct, then  $\Delta \underline{r}_k$  may not be a white gaussian noise sequence and does not satisfy Eq. 26.

In the hypothesis testing scheme, the different residuals,  $\Delta \underline{r}_k$ , for each hypothesized pilot model are compared against each other to determine which prediction,  $\Delta \hat{\underline{u}}_k(-)$ , best causes  $\Delta \underline{r}_k$  to be a white gaussian noise sequence. The mathematical details of this comparison process are presented in Appendix C and are based on work in Refs. 30 and 31. The final result is that a recursive equation can be constructed for computing the probability,  $P_{H,i}(k)$ , that pilot model  $i$  best fits the measured data. Given  $N$  pilot models there are  $N$  probabilities,  $P_{H,i}(k)$ , and the sum of the probabilities must be one. A modification is made to the hypothesis testing scheme to insure that no pilot model probability can go below  $\epsilon$ , which in this case is taken to be 0.05. This insures that if the

pilot switches control strategy, the modified scheme can change its probabilities to reflect the switch.

Care must be taken in applying the Kalman filter shown in Eqs. 24 and 25 to a situation where measured pilot data comes from an actual nonlinear pilot flight test or simulation as is the case here. The filter requires perturbation variables,  $\Delta \underline{u}_{m,k}$ , and,  $\Delta \underline{y}_k$ , but only total values,  $\underline{u}_{m,k}$ , and,  $\underline{y}_k$ , are available from the flight test. A common procedure in classical control designs, Ref. 38, is used to rectify the situation. If necessary, the measured pilot controls and observations will first be passed through a high-pass filter (sometimes known as a wash-out filter) to separate the low frequency nominal states from the high frequency perturbation states. The high-pass filter is converted to discrete-time using the bilinear transform, Ref. 39, in order to preserve its frequency domain characteristics. A value of 4 sec is used for the high-pass filter time constant.

#### 4.4 VERIFICATION WITH SYNTHETIC DATA

This section validates the pilot model hypothesis testing scheme described in the previous section with synthetic data. The synthetic data is created by a monte-carlo simulation of a pilot model for a low-order plant. The precise pilot model parameters used to create the data are known; hence it can be determined if the scheme performs correctly. Each test has three hypothesized pilot models. One pilot model is the known correct model. The other two pilot models differ from the known pilot model by varying a key pilot model parameter.

The low-order plant, Ref. 23, used to construct the pilot models has dynamics

$$\begin{bmatrix} \Delta \dot{x}_1 \\ \Delta \dot{x}_2 \end{bmatrix} = \begin{bmatrix} 0 & 1 \\ 0 & -2 \end{bmatrix} \begin{bmatrix} \Delta x_1 \\ \Delta x_2 \end{bmatrix} + \begin{bmatrix} \Delta u(t) \\ 0 \end{bmatrix} + \begin{bmatrix} 0 \\ \Delta w(t) \end{bmatrix}$$

The closed-loop pilot model feedback gain for this low-order plant is independent of  $Q_C$  in the cost function. The pilot model parameters are a time delay,  $\tau$ , of 0.1 sec, a neuromotor time constant,  $\tau_n$ , of 0.1 sec, observation noise-to-signal ratios,  $P_{y1}$ , of -20 db and a neuromotor noise-to-signal ratio,  $P_{u1}$ , of -30 db. The state  $\Delta x_1$  and its rate  $\Delta \dot{x}_1$  are assumed to be observed by the pilot model.

Four tests are performed. In all four tests, the initial condition on the state,  $\Delta x_1(0)$ , is one and all noise sources are operational. In the first test, two of the hypothesized pilot models differ from the known pilot model in the choice of the feedback gain,  $C$ . The probability time histories are shown in Fig. 40. The pilot model which has the incorrect low feedback gain is initially chosen, then the pilot model with the incorrect high feedback gain is chosen, then the true pilot model gradually increases in probability. Figure 40 is an example of what happens in hypothesis testing when the different models are very similar. The incorrect initial choices are believed to be caused by the state initial condition which asymptotically damps out after 3 seconds.

The second test uses three pilot models where two of the pilot models have incorrect values for the observation time delay. The pilot model which uses the correct time delay eventually has the highest probability as shown in Fig. 41. Note that visual observation of the predicted,  $\hat{u}_k(-)$ , and actual pilot model controls,  $u_{m,k}$ , in Figs. 40 b, c, and d cannot distinguish which hypothesized pilot model performs best.

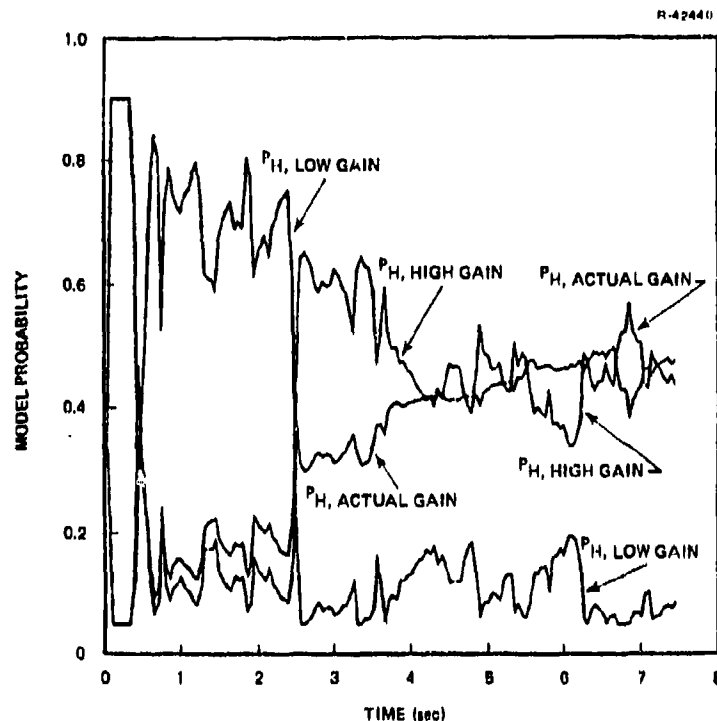
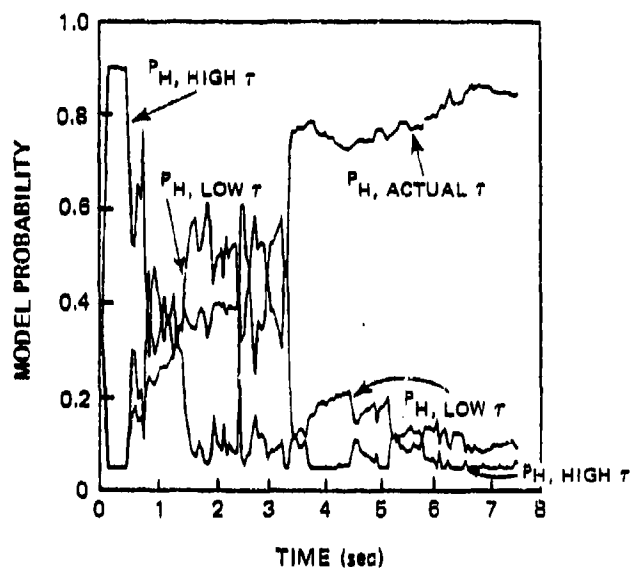


Figure 40 Pilot Model Hypothesis Testing Results For Different Feedback Gains

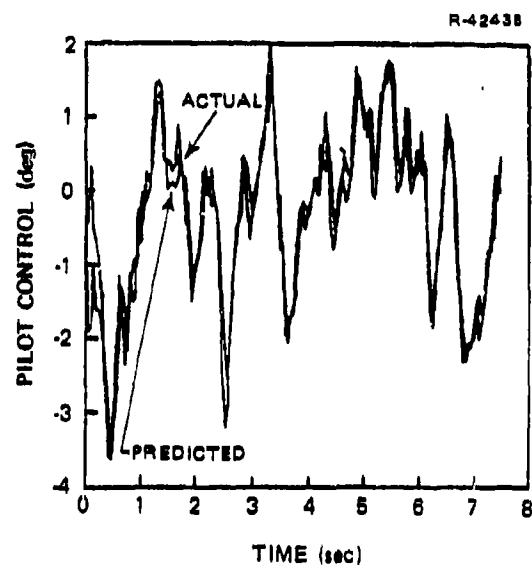
The third and fourth tests are shown in Figs. 42 and 43. In both cases, three neuromotor noise covariances are used to form three hypothesized pilot models. In both cases the pilot model with the correct neuromotor noise covariance reaches the highest probability. In Fig. 42, the pilot model's control and observation synthetic data is high-pass filtered as discussed in the previous section before the probability sequences are computed. Figures 41a and 42a are virtually identical indicating that the high-pass filtering, if necessary, should not greatly affect the results.

This section shows that the pilot model hypothesis testing scheme discussed in Section 4.3 can choose the pilot model which gives the best fit to the data. The next section presents the data from the flight test that is used for the analysis in Section 4.8.

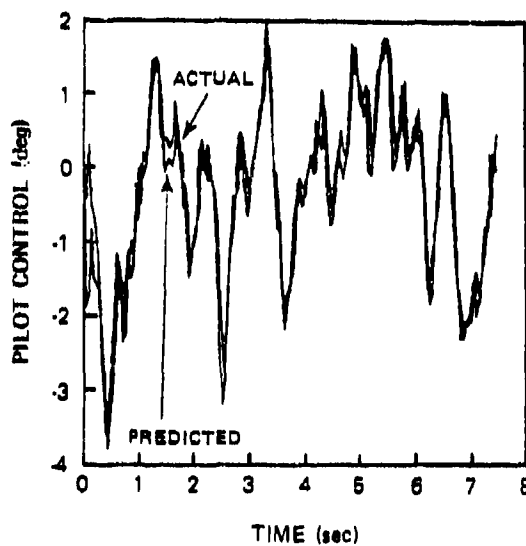




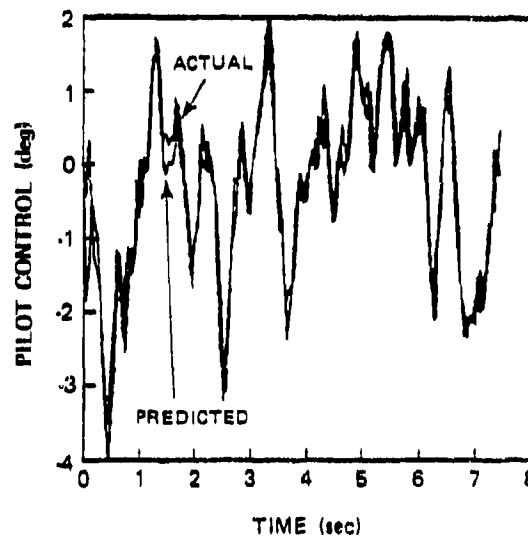
a)  $P_H$  Time Sequences



b) Actual Time Delay,  $\tau = 0.1$  sec

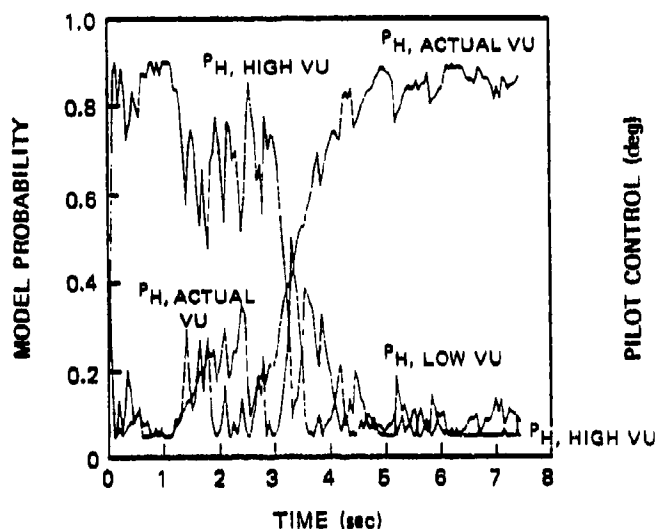
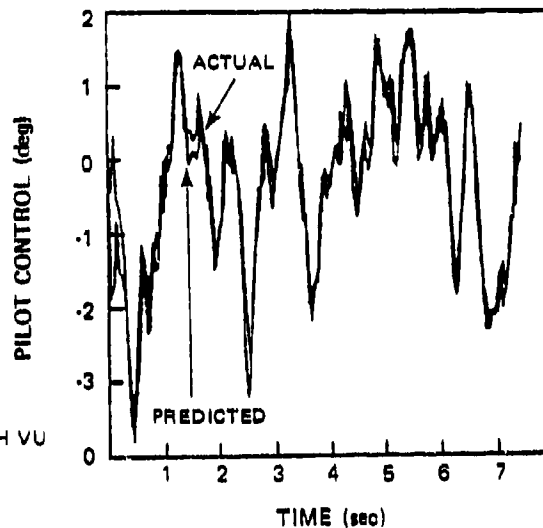


c) Low Time Delay,  $\tau = 0.05$  sec

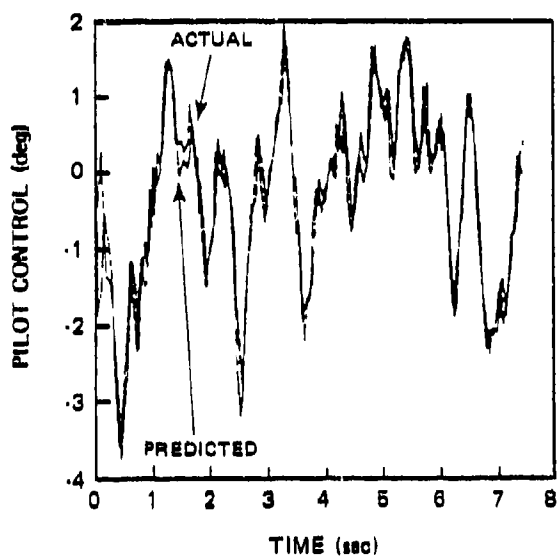


d) High Time Delay,  $\tau = 0.2$  sec

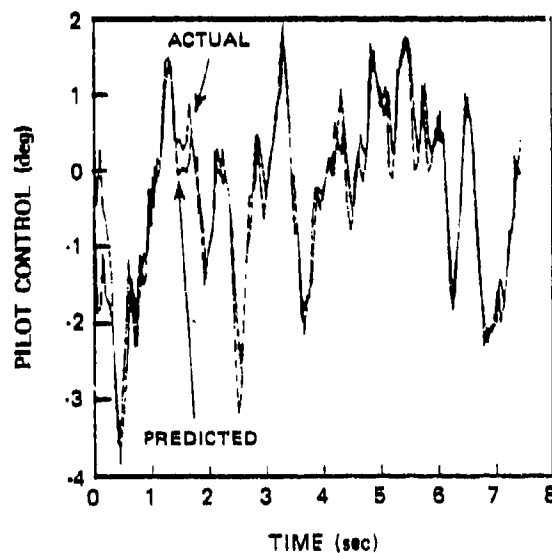
Figure 41 Pilot Model Hypothesis Testing Results For Different Time Delays

a)  $P_H$  Time Histories

b) Actual Neuromotor Noise Covariance

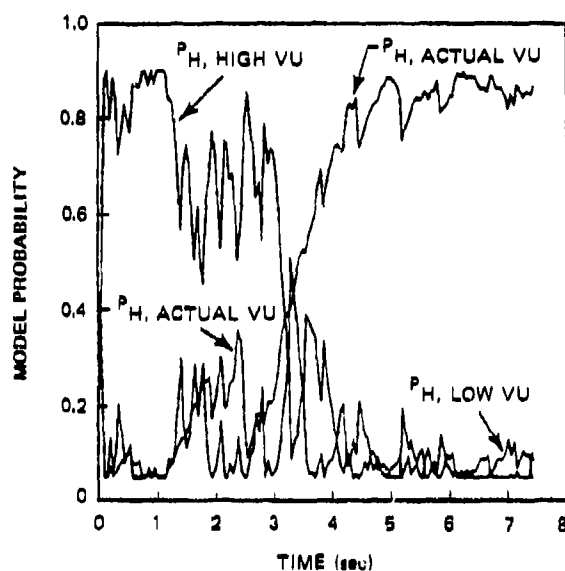
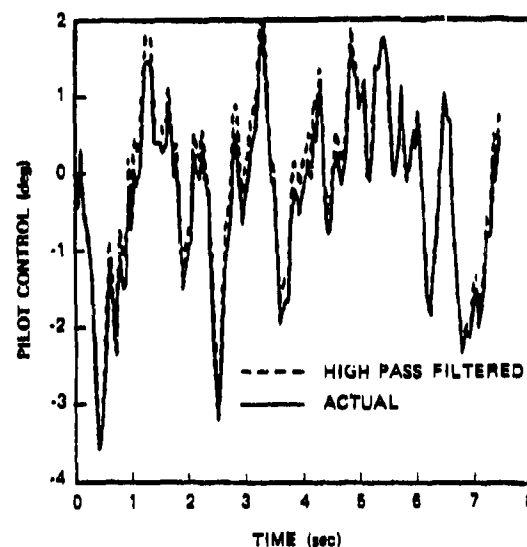


c) Low Neuromotor Noise Covariance,



d) High Neuromotor Noise Covariance

Figure 42 Pilot Model Hypothesis Testing Results For Different Neuromotor Noise

a)  $P_H$  Time Histories

b) Control Time Histories

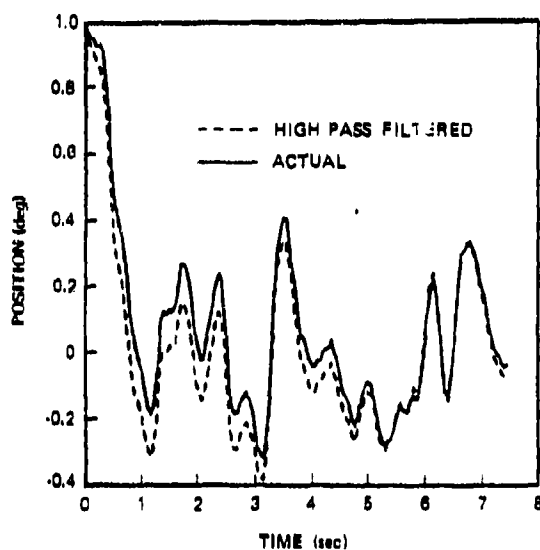
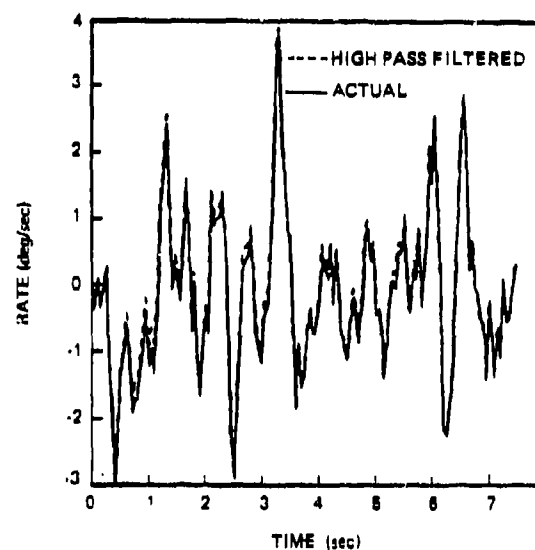
c) Position Observation  
Time Historyd) Rate Observation Time  
History

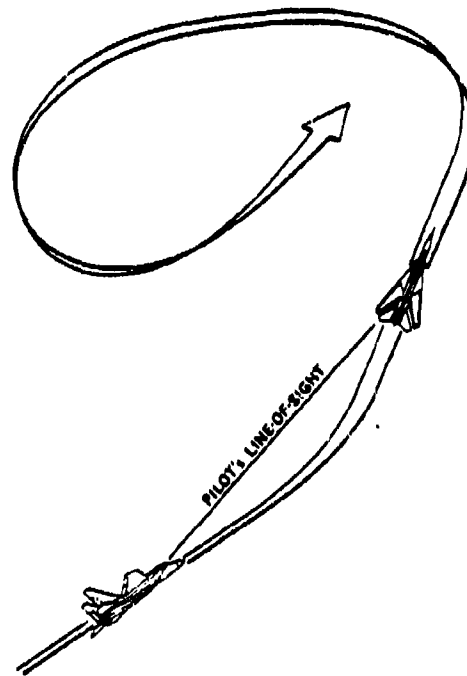
Figure 43 Pilot Model Hypothesis Testing Results for  
Different Neuromotor Noise Covariances and  
High-Passed Data

#### 4.5 FLIGHT TEST SELECTION

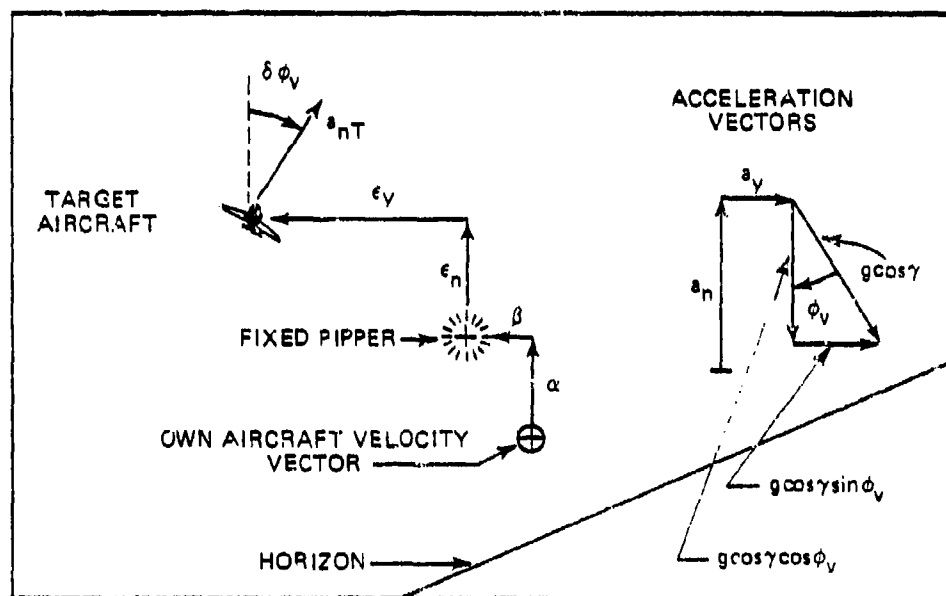
The simulated flight test selected for study is a wind up turn tracking task using the NASA-Langley Differential Maneuvering Simulator (DMS). The pilot is instructed to track a target aircraft which is displayed on a large hemi-spherical screen, within which the cockpit is mounted. A sky-earth representation is also displayed. The target aircraft's trajectory is prestored. There are no intentional disturbances affecting either the target aircraft or the piloted aircraft, although the prestored target trajectory exhibits rapid and continuous maneuvering.

The pilot is instructed not to use rudder pedals. Lateral-directional control by the pilot is accomplished using only lateral stick. The simulation is performed with the pitch and yaw sas operational, although the roll cas is off. The yaw sas improves the lateral-directional stability of the aircraft at high angles of attack. This means that the stability boundaries of the bare-aircraft determined in Refs. 1 and 23 cannot be used directly to evaluate pilot performance and the performance of the hypothesis testing scheme. The sas states also have to be included in the aircraft model increasing the dimension of the problem.

The view through the cockpit which is useful in constructing the tracking error equations is shown in Fig. 44. The vertical and lateral components of tracking error are  $\varepsilon_n$  and  $\varepsilon_y$ , respectively, which the pilot can directly perceive. The difference between the pilot's fixed pipper and the aircraft's velocity vector are the angle of attack,  $\alpha$ , and sideslip angle,  $\beta$ , which the pilot cannot directly perceive. The difference between the aircraft's stability-axis roll angle,  $\phi_v$ , and the stability-axis roll angle of the target,  $\phi_{VT}$ , is



a) Air-to-Air Combat



b) View Through Cockpit

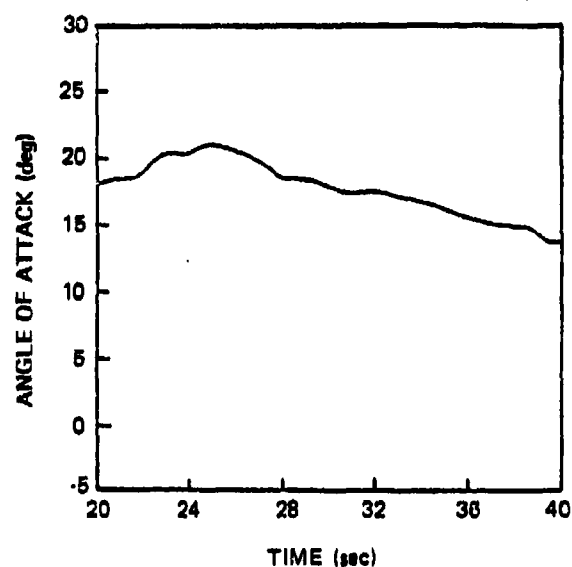
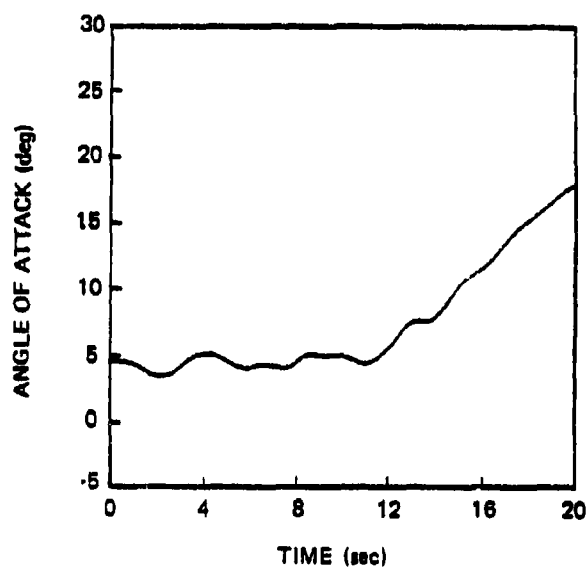
Figure 44 Pursuit-Tracking Task

$\delta\phi_v$  and is directly perceived by the pilot. The pilot does not have any motion cues. Any computational time delay in the DMS between the pilot's stick movement and changes on the screen is assumed to be small and is not modeled in the analysis.

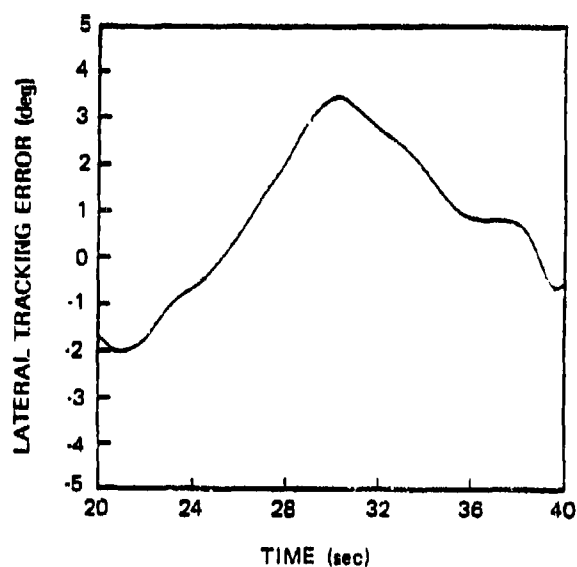
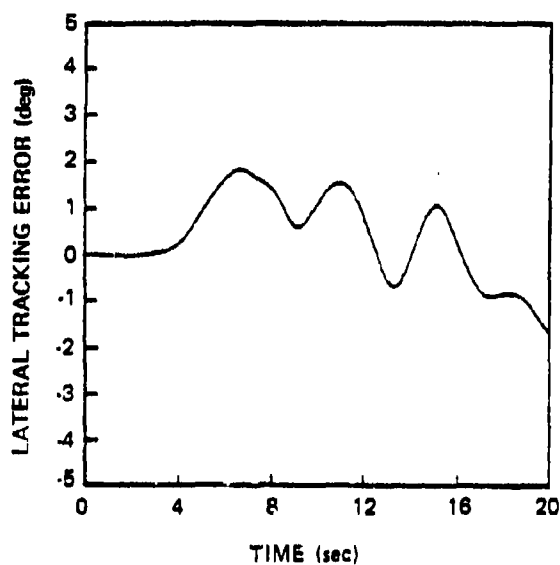
A complete record of the aircraft state and control histories is recorded at 32 samples per second. Additionally, the tracking angles and range to the target are recorded, and target motion is inferred from these measurements. This approach dictated the target aircraft identification procedure discussed in Section 4.6 and required the tracking equation simplifications shown in Appendix B.

The wind-up turn tracking task lasted 90 sec. At 50 sec into the run, the pilot is forced to saturate lateral stick almost continuously in order to continue tracking. Because of this, only the first 40 sec of the run are analyzed. Originally it was intended to perform hypothesis testing on both the lateral-directional and longitudinal dynamics, coupled and uncoupled. The complexity of the sas states increases the dimension of the coupled Kalman filter in Eq. 24 from 26 to 38 states placing the computation requirements of a coupled analysis outside the scope of this analysis. Only the uncoupled lateral-directional dynamics are to be investigated with the pilot model.

Variations of angle of attack and lateral tracking error,  $\varepsilon_y$ , are shown in Figs. 45a and 45b for the 40 sec interval. The aircraft remains at a low angle of attack flight condition for the first 10 seconds, then the aircraft angle of attack gradually increases passing through the  $\alpha = 16$  deg stability boundary discussed in the introduction of this chapter without incident. As previously mentioned, the lack of instability at high angles of attack is due to the yaw sas since

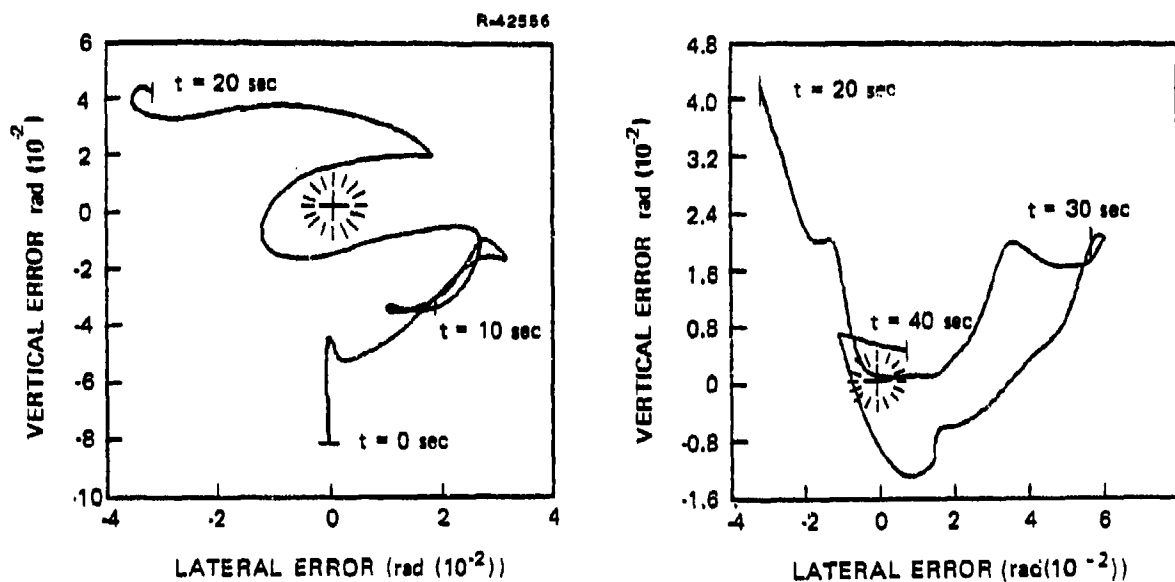


a) Angle of Attack Time History

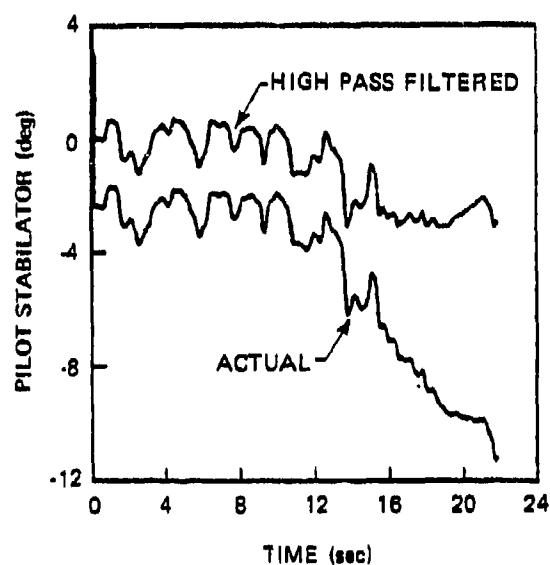


b) Lateral Tracking Error Time History

Figure 45 Aircraft State Time Histories



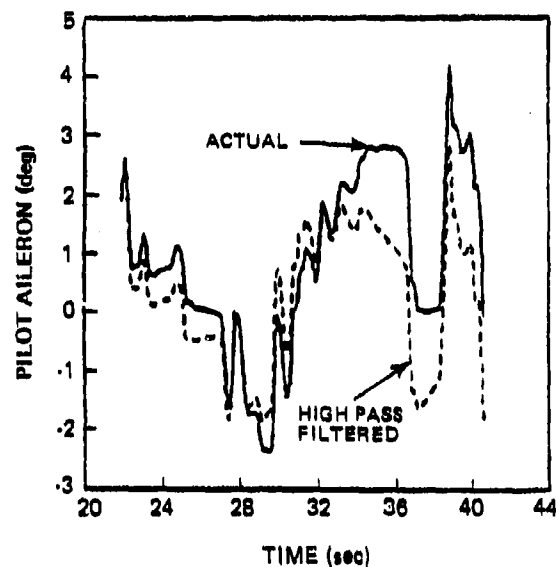
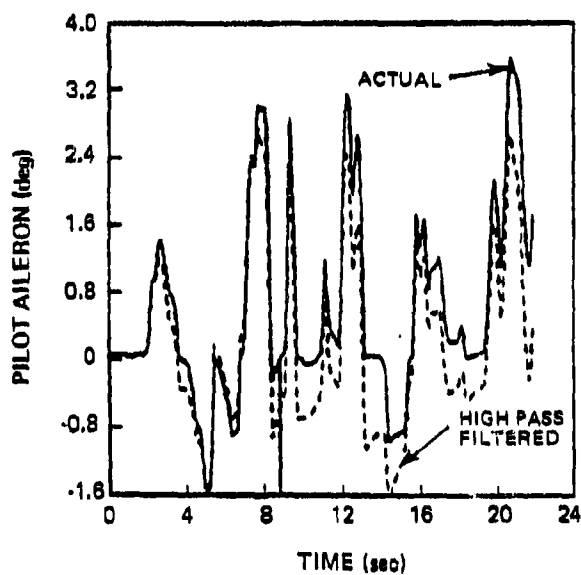
c) Path of Target Aircraft Referenced to Aircraft Pipper



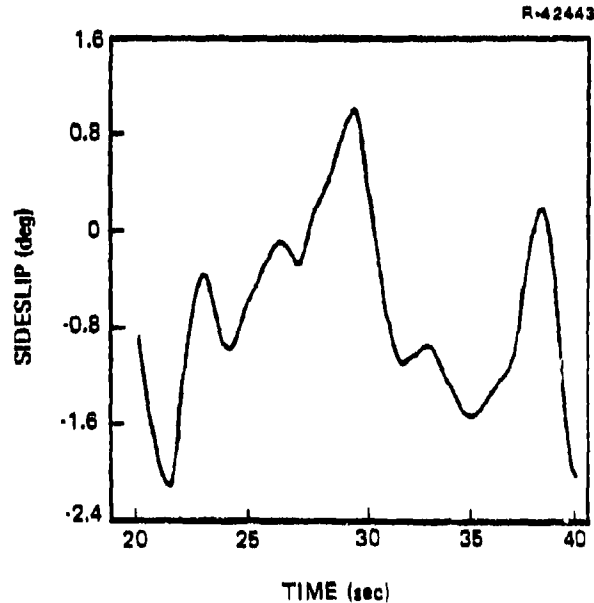
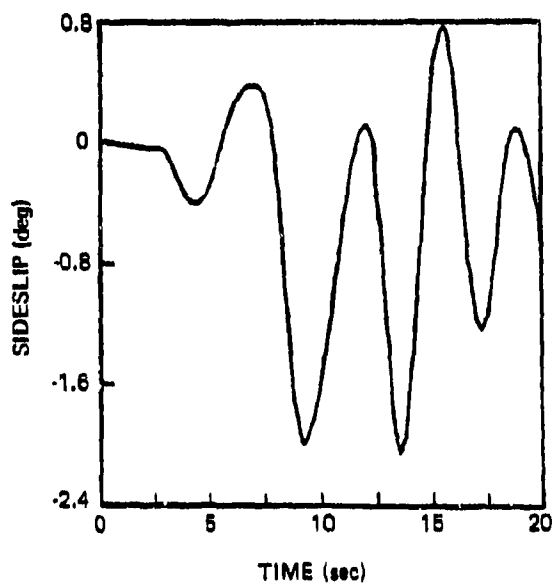
d) Pilot Longitudinal Control Time History

Figure 45 Aircraft Time Histories (Continued)





(e) Pilot Lateral Control Time History



(f) Sideslip Angle Time History

Figure 45 Aircraft State Time Histories (Continued)

former DMS simulations with the bare aircraft, at high  $\alpha$ , using only lateral stick, Ref. 23, exhibit piloting difficulties  $\alpha$  beyond 16 deg  $\alpha$ .

The trajectory of the target aircraft as seen through the windscreen is shown Fig. 45c. The target aircraft starts at the bottom of the screen and is eventually brought to the pipper area by the end of 40 sec. Figure 45d shows the pilot's stabilator commands from the longitudinal stick. Although there are no disturbances in the system, the pilot's control movements exhibit considerable activity. The intended operation of the high-pass filter is effectively shown in Fig. 45d. The high-pass filter moves the pilots stabilizing perturbation actions back to the zero axis from the a nominal  $\delta_s = -2$  deg.

The aileron control command of the pilot lateral stick is shown in Fig. 45e. In this case, the pilot's command is centered near the zero axis and there is no need to use the high-pass filter. The pilot similarly manages to keep  $\epsilon_y$  near the zero axis in Fig. 45b and, as shown in Fig. 46, also keeps  $\delta\phi_v$  near the zero axis. Since only the lateral-directional axis is to be investigated it is decided that the high-pass filter is not necessary and  $\delta_a$ ,  $\epsilon_y$ , and  $\delta\phi_v$  can be used directly in Eqs. 24 and 25. If the longitudinal axis would have been investigated, the high-pass filter would be required.

The pilot manages to keep sideslip angle close to zero as shown in Fig. 45f. A small sideslip angle is an indication the pilot is purposefully flying a coordinated turn and regulating sideslip. Some of the instabilities at high angle of attack simulated in Ref. 3 are characterized as a high frequency growing oscillation in  $\beta$  which is not evident in Fig. 45f. NASA Langley provided a second wind-up turn tracking task which had the unstable sideslip oscillation time

history but unfortunately could not be analyzed within available resources.

Using the aircraft time histories shown in Fig. 45, the pilot model hypothesis test can be well posed; when the angle of attack of the aircraft increases beyond 5 deg (see Fig. 45a), significantly changing the aircraft's dynamics, does the pilot's control behavior (Fig. 45e) remain fixed to a 5 deg  $\alpha$  strategy or does the pilot change his strategy to match the aircraft's changing dynamics? To begin answering this question, the hypothesized dynamical model of the aircraft-target dynamics must first be developed.

#### 4.6 TRACKING TASK MODEL

The tracking task model ((1) in Table 13) is composed of four components at the adaptation point; the linearized dynamics of the subject aircraft, the sas dynamics, the linearized tracking error dynamics, and the linearized target model. A derivation of the first two models is presented in Appendix A while the latter two models are derived in Appendix B. A summary of all the linearized models is given in Table 14.

Combining all the models in Table 14 results in the tracking task model used here and is shown in Eq. 27. The states  $\Delta v$ ,  $\Delta r$ ,  $\Delta p$ , and  $\Delta \phi_v$  in the model are the perturbation body y-axis velocity, body-axis yaw rate, body-axis roll rate, and stability axis roll angle of the aircraft, respectively. The state,  $\Delta \epsilon_y$ , is the perturbation lateral tracking error. The states  $\Delta p_{wT}$  and  $\Delta \phi_{vT}$  are the target's perturbation stability-axis roll rate and roll angle, respectively. The variable  $\Delta x_{SAS}$  is the state associated with the wash out filter in the yaw sas channel of the aircraft.

TABLE 14  
LINEARIZED TRACKING MODEL DYNAMICS

T-3121

<p>1. Bare Aircraft Dynamics</p> $\dot{\Delta \underline{x}}_a = F_a \Delta \underline{x}_a + G_a \Delta \underline{u}_a$ $\Delta \underline{u}_a = K_1 \Delta \underline{u}_p + \Delta \underline{u}_{SAS}$	<p><math>F_a, G_a</math> Linearized aircraft matrices</p> <p><math>\Delta \underline{x}_a</math> Aircraft states <math>\Delta v</math>, lateral body-axis velocity, <math>\Delta r</math>, body-axis yaw rate, <math>\Delta p</math>, body-axis roll rate and <math>\Delta \phi_v</math>, stability-axis roll angle</p> <p><math>\Delta \underline{u}_a</math> Aircraft controls <math>\Delta \delta_{sp}</math>, spoilers, <math>\Delta \delta_{ds}</math>, differential stabilizers and <math>\Delta \delta_r</math>, rudder</p> <p><math>\Delta \underline{u}_p</math> Pilot's lateral stick control</p>
<p>2. SAS Dynamics</p> $\Delta \underline{u}_{SAS} = K_2 \Delta \underline{x}_a + K_3 \Delta \underline{u}_a + K_4 \Delta \dot{\underline{x}}_{SAS}$ $\dot{\Delta \underline{x}}_{SAS} = F_{SAS} \Delta \underline{x}_{SAS} + G_{SAS} \Delta \underline{x}_a$	<p><math>\Delta \underline{u}_{SAS}</math> Stabilization commands from SAS to aircraft controls</p> <p><math>F_{SAS}, G_{SAS}</math> Dynamical representation of the SAS yaw rate wash-out filter given by</p> $\Delta \phi_{r, SAS} = K_1 \Delta a_y + \Delta r - \Delta \dot{\underline{x}}_{SAS}$ $\dot{\Delta \underline{x}}_{SAS} = -\frac{1}{\tau} \Delta \underline{x}_{SAS} + \frac{1}{\tau} \Delta r$ <p><math>\tau</math> Wash-out filter time constant</p>
<p>3. Tracking Error Dynamics</p> $\dot{\Delta \underline{e}}_y = K_5 \Delta \underline{x}_a + K_6 \Delta \underline{u}_a + K_7 \Delta \dot{\underline{x}}_T$	<p>Represents the equation</p> $\dot{\Delta \underline{e}} = -\frac{a_{nT_0}}{V_0} (\Delta \phi_{vT} - \Delta \phi_v) + \frac{\Delta a_y}{V_0} + \Delta \dot{\underline{e}}$ <p><math>a_{nT_0}</math> Target's nominal normal acceleration</p> <p><math>V_0</math> Aircraft's nominal velocity</p> <p><math>a_y</math> Inertial lateral acceleration expressed in body axis</p>
<p>4. Target Model</p> $\dot{\Delta \underline{x}}_T = F_T \Delta \underline{x}_T + G_T \Delta \underline{w}_T$	<p>Represents the equation</p> $\begin{bmatrix} \dot{\Delta p_{wT}} \\ \dot{\Delta \phi_{vT}} \end{bmatrix} = \begin{bmatrix} a_1 & a_2 \\ 1 & 0 \end{bmatrix} \begin{bmatrix} \Delta p_{wT} \\ \Delta \phi_{vT} \end{bmatrix} + \begin{bmatrix} \Delta w_T \\ 0 \end{bmatrix}$ <p><math>\Delta \phi_{vT}</math> target stability-axis roll angle</p> <p><math>\Delta p_{wT}</math> target stability-axis roll rate</p>

$$\begin{bmatrix} \dot{\Delta v} \\ \dot{\Delta r} \\ \dot{\Delta p} \\ \dot{\Delta \phi_v} \\ \dot{\Delta \dot{x}}_y \\ \dot{\Delta p_{wT}} \\ \dot{\Delta \phi_{vT}} \\ \dot{\Delta \dot{x}}_{SAS} \end{bmatrix} = \begin{bmatrix} F_a + G_a(1-K_3)^{-1}K_2 & 0 & 0 & G_a(1-K_3)^{-1}K_4 \\ K_5 + K_6(1-K_3)^{-1}K_2 & 0 & K_7 & K_6(1-K_3)^{-1}K_4 \\ 0 & 0 & F_T & 0 \\ G_{SAS} & 0 & 0 & F_{SAS} \end{bmatrix} \begin{bmatrix} \Delta v \\ \Delta r \\ \Delta p \\ \Delta \phi_v \\ \Delta \dot{x}_y \\ \Delta p_{wT} \\ \Delta \phi_{vT} \\ \Delta \dot{x}_{SAS} \end{bmatrix} + \begin{bmatrix} G_a(1-K_3)^{-1}K_1 \\ K_6(1-K_3)^{-1}K_1 \\ 0 \\ 0 \end{bmatrix} \begin{bmatrix} \Delta u_p \end{bmatrix} + \begin{bmatrix} 0 \\ 0 \\ G_T \\ 0 \end{bmatrix} \Delta w_T$$

The model is typical of air-to-air combat investigation models first performed in Ref. 36 and later in Ref. 37 using the optimal control pilot model. In both references the aircraft models are simplified linear time-invariant longitudinal dynamics implemented on simulators. Simple target dynamics are used both in the simulation and the model. In our case use of the complete target aircraft model, as used in the DMS, in the tracking task model is infeasible. An approximation whereby only the target aircraft states  $\Delta p_{wT}$  and  $\Delta \phi_{vT}$  are modeled in the tracking task model must be made.

The approximation is made by determining what target dynamics are essential to the pilot in formulating his internal model of the target. Since the stability axis roll angle is the important target state, only that state and its derivative are included in the target model. In the pilot's internal target model, unmodeled target model dynamics are lumped into a zero mean gaussian noise term  $\Delta w_T$  which drives  $\Delta p_{wT}$ . The implication of this assumption is that the human has no explicit information regarding  $\Delta w_T$  and must model its effect as white noise. A detailed discussion of this type of white noise assumption is given in Ref. 37. The parameters in the simplified target model in Table 14 can be determined by identification based on measured values of  $\phi_{vT}$ . The approach taken here is to perform an exhaustive search over  $a_1$ ,  $a_2$  and the covariance of  $\Delta w_T$  in Table 14 using the hypothesis testing scheme in Appendix C.  $\phi_{vT}$  is not available as a direct measurement from the NASA DMS data. Using the available measurements and the  $\epsilon_n$ ,  $\epsilon_y$  dynamics shown in Eqs. B-12 and B-13,  $\phi_{vT}$  is reconstructed from the data as

$$\delta \phi_v = \tan^{-1} \frac{-V(\dot{\epsilon}_y + \dot{\beta}) + a_y}{V(\dot{\epsilon}_n + \dot{\alpha}) + a_n} \quad (28)$$

$$\hat{\phi}_{vT} = \phi_v + \delta \phi_v$$

Back differencing is used to calculate the derivatives in Eq. 28. Figure 46 shows plots of the resulting calculations. The movements in the aircraft stability-axis roll angle,  $\phi_v$ , follows the movements of  $\phi_{vT}$  as the pilot tracks the target aircraft. The target's normal acceleration is also calculated and shown in Fig. 46. Using  $\hat{\phi}_{vT}$  in Fig. 46, a series of target model parameters are postulated, and hypothesis testing is used to choose the set which best matches the actual target data. This search yielded  $a_1 = -4.4$ ,  $a_2 = -1.6$ , and  $E\{w_T^2\} = 4.0$  ( $\text{deg}^2/\text{sec}^2$ ) for the pilot's internal target model parameters.

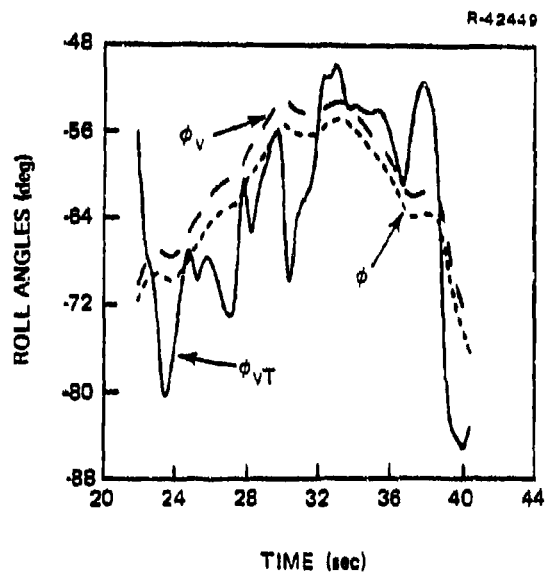
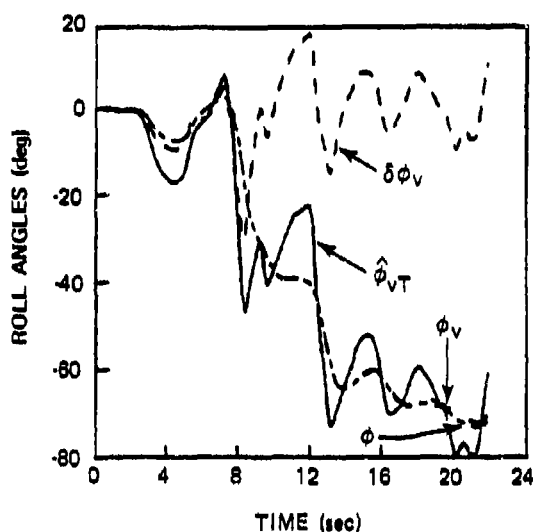
#### 4.7 PURSUIT TRACKING PILOT MODEL PARAMETERS

The parameters left to be specified for the pilot model are the pilot cues (2 in Table 13), a preliminary choice of the pilot's quadratic state weighting matrix,  $Q_c$ , in Table 12, the standard human parameters discussed in Section 4.3, and the flight conditions. The flight conditions are a priori specifications of hypothesized aircraft dynamics at which the pilot may formulate a control strategy. The perturbation dynamics at the chosen flight conditions form the pilot's internal model of the aircraft.

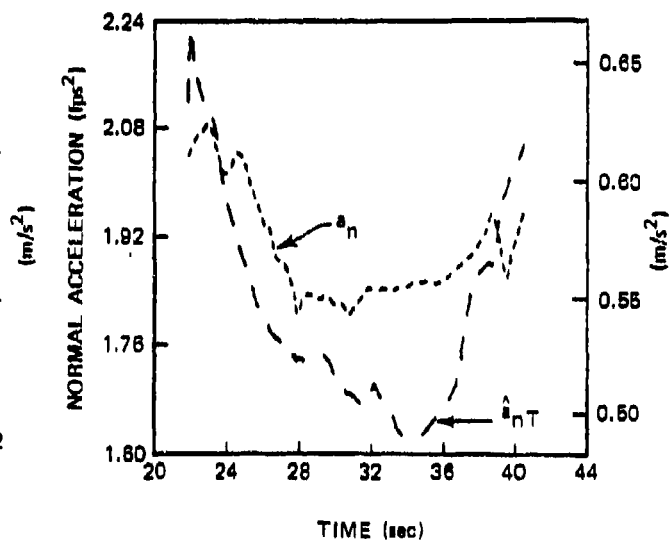
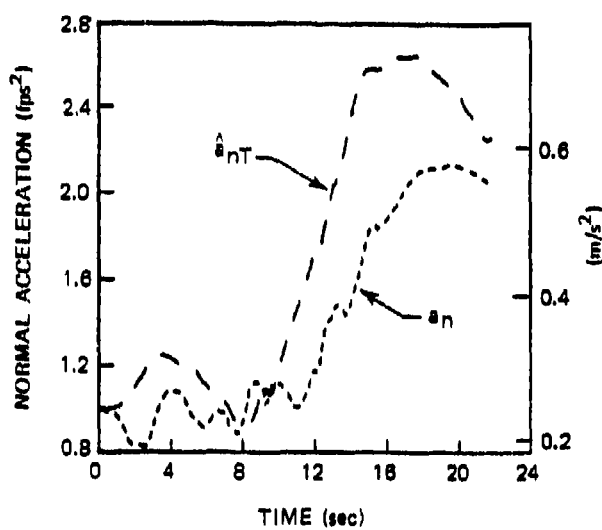
From Fig. 44, the pilot cues are the lateral error,  $\Delta\epsilon_y$ , and stability-axis roll angle error,  $\Delta\delta\phi_v$ . As is customary in optimal control control pilot models, the rates of these states are also assumed observed by the pilot resulting in

$$\Delta\mathbf{y}^T = [\Delta\epsilon_y, \Delta\dot{\epsilon}_y, \Delta\delta\phi_v, \Delta\dot{\delta}\phi_v]$$

The derivatives of the states in  $\Delta\mathbf{y}$  are computed by back differencing the measurements  $\Delta\epsilon_y$  and  $\Delta\delta\phi_v$ . From Fig. 45a, three flight conditions which primarily differ in angle of attack



a) Aircraft and Target Aircraft Roll Time Histories



b) Aircraft and Target Aircraft Normal Acceleration Time Histories

Figure 46 Postprocessing of Flight Data To Obtain Target Dynamics

are chosen for the pilot's internal model; low,  $\alpha_o = 5.2$  deg, medium,  $\alpha_o = 9.3$  deg, and high,  $\alpha_o = 19.2$  deg.

The quadratic cost function weights quantify the pilot's tradeoff of tracking error and control effort. High weights imply that the pilot expends significant control effort in order to minimize tracking error. He can be said to be a "high-gain" or "tight" pilot. On the other hand, low quadratic weights will typify a "low-gain" or "loose" piloting technique. The specific values for the quadratic weights used in the tests reported here are given in Table 15. The tracking error rate weight in  $Q_c$  is chosen to be one-fourth of the tracking error weight as suggested in Ref. 36. Based on Fig. 45f, lateral velocity is weighted and because the pilot seemed to place more emphasis on reducing  $\Delta\phi_v$  variations rather than  $\Delta\delta\phi_v$  variations in Fig. 46a,  $\Delta\phi_v$  is weighted in  $Q_c$ . At the low  $\alpha_o$  and medium  $\alpha_o$  flight conditions in Table 14, a high weight (2) and a low weight (1)  $Q_c$  are specified. The rest of the pilot model parameters are standard ( $\tau=0.2$  sec,  $\tau_n = 0.1$  sec,  $P_y = -20$  db,  $P_u = -30$  db).

The resulting pilot model closed-loop eigenvalues and feedback gain elements are shown in Tables 16 and 17 respectively. The eigenvalues and gains exhibit little change when  $Q_c$  changes between cost functions 1 and 2 in Table 15. The closed-loop eigenvalues are not very satisfactory from a control point of view. At  $\alpha_o = 9.3$  deg the sas/tracking error mode combination has poor damping while the roll angle eigenvalue at  $\alpha_o = 5.2$  deg is almost neutrally stable. The pilot model control gains at  $\alpha_o = 5.2$  deg and  $\alpha_o = 9.3$  deg are similar, while the high  $\alpha_o$  pilot model gains have significant differences. These differences indicate the hypothesis testing scheme should be able to make a clear decision between the high and low  $\alpha_o$  strategies.



TABLE 15  
SQUARE ROOT OF PILOT MODEL COST FUNCTION WEIGHTS

T-3122

AIRCRAFT ANGLE OF ATTACK	COST FUNCTION	LATERAL VELOCITY	ROLL ANGLE	TRACKING ERROR	TRACKING ERROR RATE
5.2	1	0.25	0.50	5.0	1.25
5.2	2	0.50	1.00	10.0	2.5
9.3	1	0.25	0.25	5.0	1.25
9.3	2	0.25	0.25	10.0	2.5
19.5	1	0.25	0.25	5.0	1.25

#### 4.8 HYPOTHESIS TESTING RESULTS

This section presents the results from the hypothesis testing scheme in two formats. In the first format, the one-step predicted pilot model control time history is overlaid on the actual pilot's lateral stick control time history. The closer these two trajectories match, the better the indication is that the assumed pilot model is correct. The second format is composed of plots of the probabilities that a pilot model is the best of those tested. The first format gives an absolute indication of pilot model performance while the second format gives a relative indication of performance between the pilot models.

Initial trials of the hypothesis testing calculation procedure with the piloted simulation data indicated a severe mismatch occurs between the Kalman filter's estimate of its output error covariance,  $S$  in Eq. 26, and the actual output error covariance, which is calculated as

TABLE 16  
PILOT-MODEL-AIRCRAFT CLOSED-LOOP EIGENVALUES

T-3123

VELOCITY, m/s	ANGLE OF ATTACK, deg	COST FUNCTION	DUTCH ROLL		TRACKING ERROR/ SAS STATE		PILOT LATERAL STICK, sec	ROLL MODE $t_r$ , sec	ROLL ANGLE $t_r$ , sec	TARGET ROLL RATE $t_r$ , sec	TARGET ROLL ANGLE $t_r$ , sec
			$\omega_n$ rad/sec	$\xi$	$\omega_n$ rad/sec	$\xi$					
178	5.2	1	5.48	0.513	0.621	0.820	0.192	0.530	310.0	0.25	2.5
178	5.2	2	5.51	0.517	0.691	0.820	0.192	0.530	310.0	0.25	2.5
165	9.30	1	5.29	0.566	0.630	0.184	0.268	0.391	1.74	0.25	2.5
165	9.30	2	5.36	0.579	0.643	0.113	0.296	0.355	1.71	0.25	2.5
165	19.2	1	5.18	0.548	0.435	0.937	0.287	0.488	3.34	0.25	2.5

TABLE 17  
PILOT MODEL LATERAL STICK GAINS

T-3124

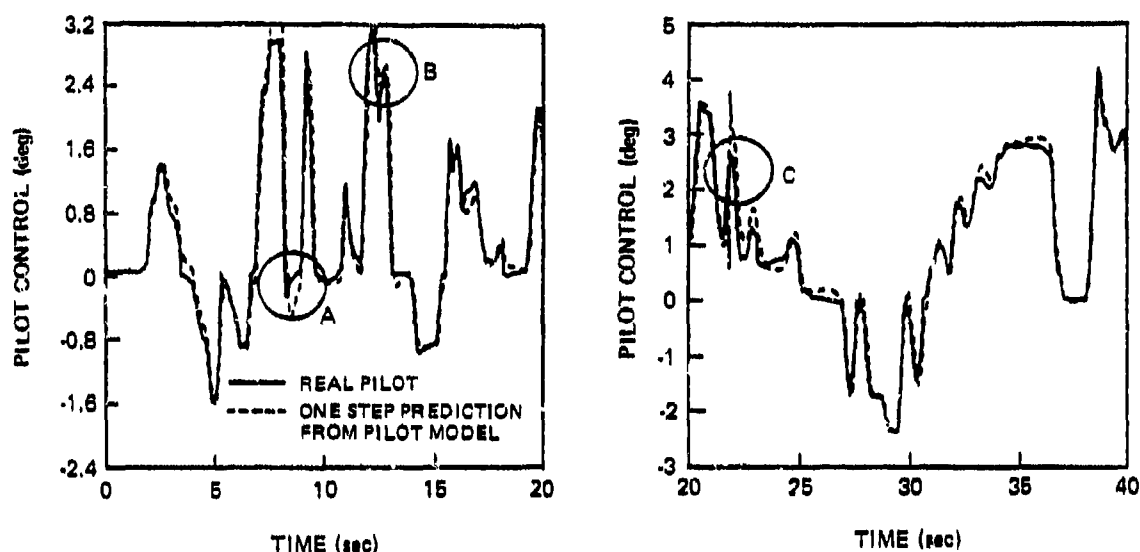
AIRCRAFT ANGLE OF ATTACK	COST FUNCTION	SIDE VELOCITY $\partial\delta/\partial\gamma$	VAV RATE $\partial\delta/\partial\gamma$	ROLL RATE $\partial\delta/\partial p$	ROLL ANGLE $\partial\delta/\partial\phi$	TRACKING ERROR $\partial\phi/\partial\delta$	TARGET ROLL RATE $\partial\delta/\partial p$	TARGET ROLL ANGLE $\partial\delta/\partial\phi$	SAS
									$\partial\phi/\partial x_{sas}$
5.2	1	-1.59	-9.51	2.44	4.98	51.9	-1.22	-5.66	7.38
5.2	2	-1.72	-9.64	2.47	5.05	52.8	-1.24	-5.70	7.53
9.3	1	-1.45	-10.63	3.59	5.08	44.7	-0.787	-4.62	-1.25
9.3	2	-1.38	-14.85	3.77	4.18	48.5	-0.587	-4.01	-3.96
19.2	1	14.05	-77.2	5.34	-30.2	-43.4	4.14	18.06	-98.6

$$S_k = \frac{1}{k} \sum_{i=1}^k (\underline{u}_{m,i} - \hat{\underline{u}}_i(-)) (\underline{u}_{m,i} - \hat{\underline{u}}_i(-))^T \quad (29)$$

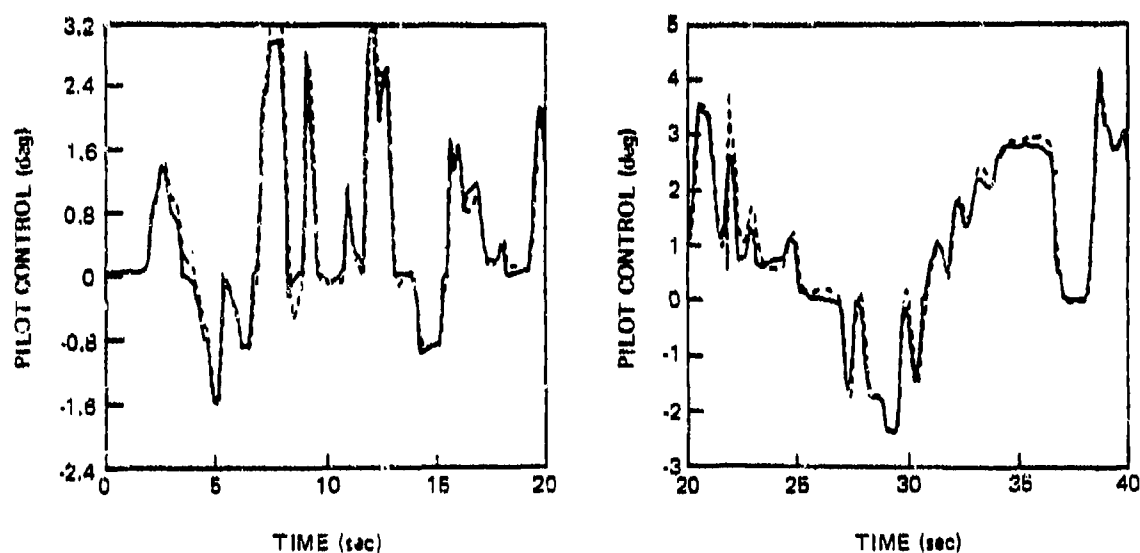
For a large number of data points ( $k$  is large), the matrix  $S_k$  should approach  $S$  for a linear, time-invariant system. The mismatch occurs because the pilot's internal model of the target driving covariance,  $E\{w_T^2\}$ , appears to differ from the actual value calculated in Section 4.5, and also due to the existence of unmodeled nonlinearities and the time-varying nature of the actual piloted simulation. The pilot model probabilities, which strongly depend on  $S$ , cannot be calculated in the presence of this mismatch.

One approach to resolve this mismatch, suggested in Ref. 35, is to adjust the pilot's internal model of the target driving covariance until the mismatch is minimized. Since this requires a large number of iterations of the pilot model calculations and the hypothesis testing procedure, this approach is not pursued here. Rather, a simpler approach is used whereby an estimate of  $S$ , based on Eq. 29 applied to the entire 1280 samples of data is used in the hypothesis testing scheme. This procedure yields well-behaved pilot model probabilities from the hypothesis testing scheme. The usefulness of this modification is confirmed by the agreement observed in the next paragraphs between the hypothesis testing results and the pilot control trajectory comparisons.

Comparisons of the actual pilot control time history to the pilot model predictions are illustrated in Fig. 47. The low  $\alpha$  pilot model with normal piloting technique shown in Fig. 47a matches the actual pilot's responses quite well, except perhaps in the regions circled. The  $\alpha_0$  pilot model with especially "tight" piloting technique (Fig. 47b) exhibits no

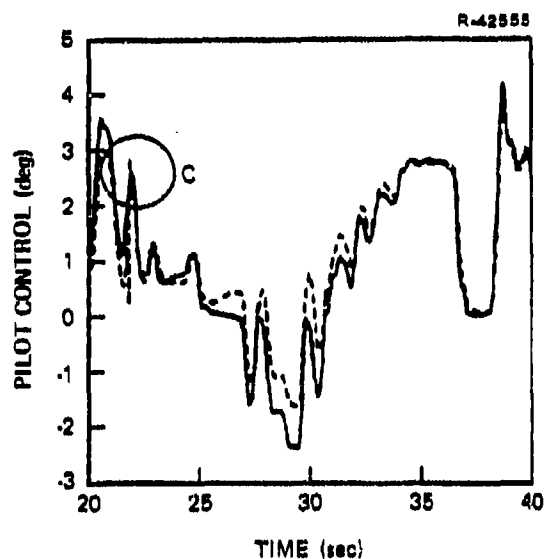
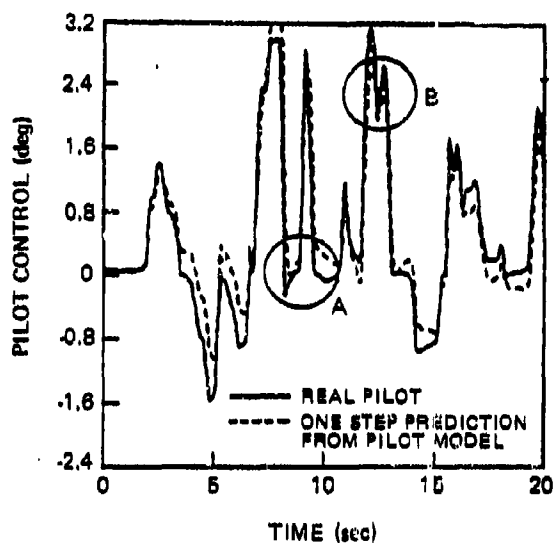


a) Low  $\alpha$  Pilot Model With Nominal Quadratic Cost Weights

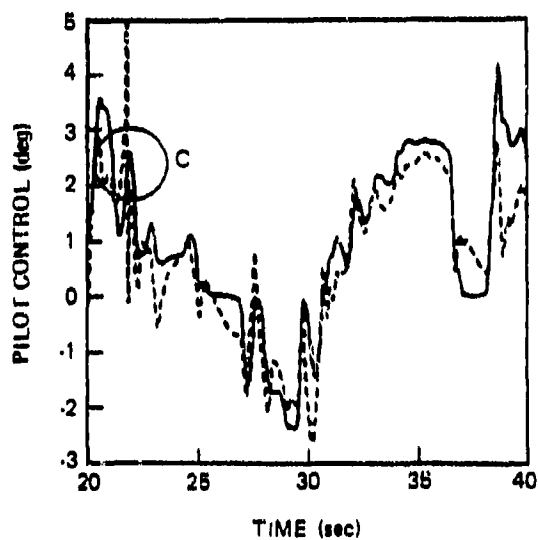
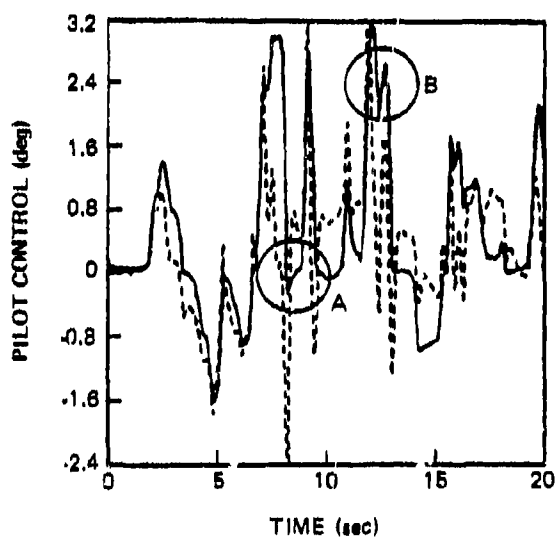


b) Low  $\alpha$  Pilot Model With High Quadratic Cost Weights

Figure 47 Comparison of Actual and Predicted Pilot Controls



c) Medium  $\alpha$  Pilot Model With Nominal Quadratic Weights



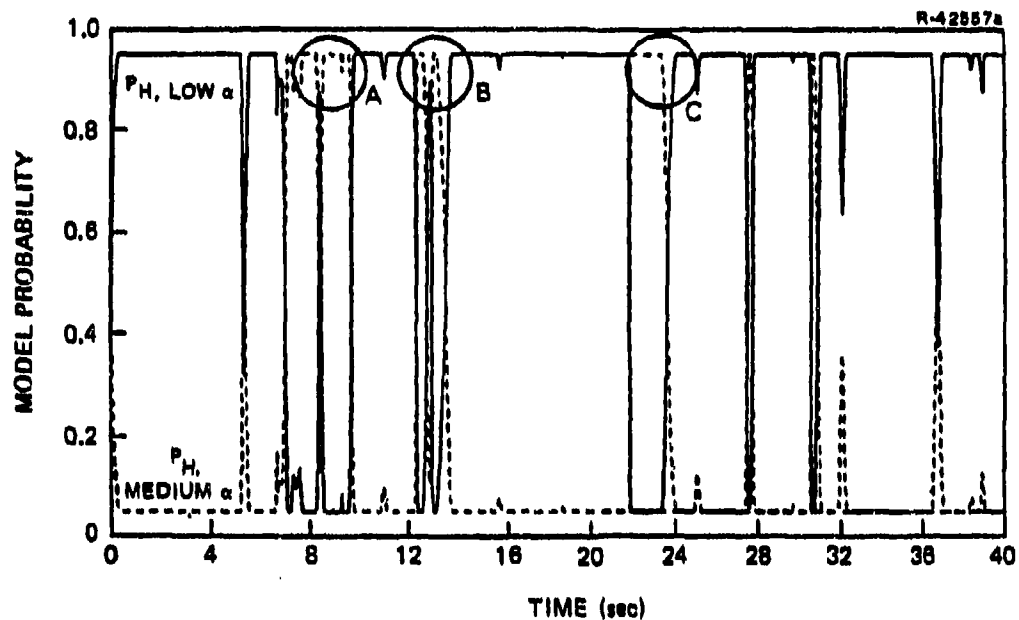
d) High  $\alpha$  Pilot Model

Figure 47 Comparison of Actual and Predicted Pilot Controls (Continued)

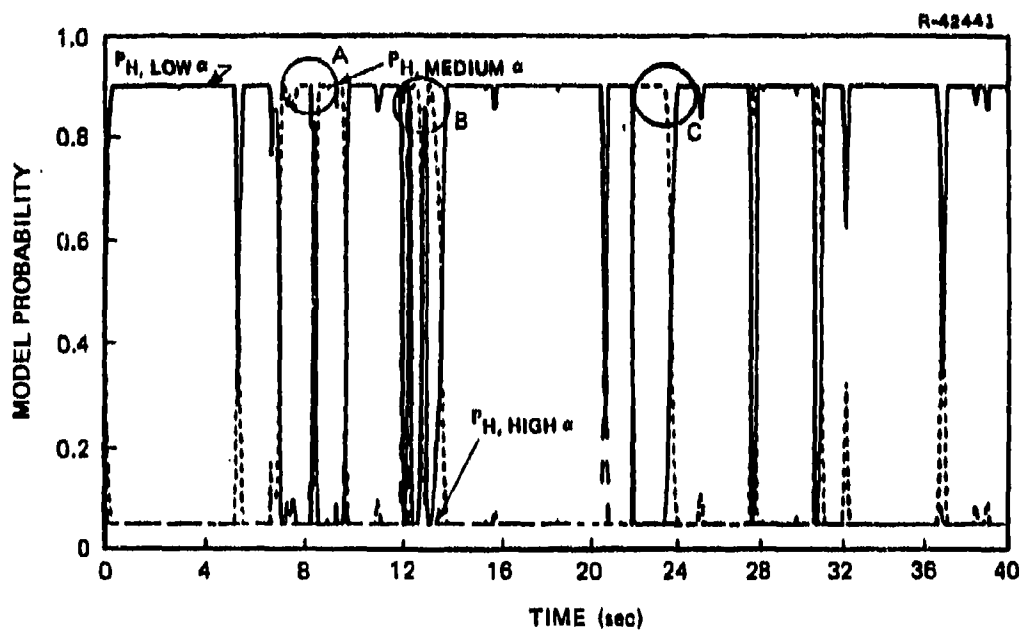
discernable difference from the low  $\alpha_0$  nominal pilot model. The medium  $\alpha$  pilot model (Fig. 47c) does not match the pilot control inputs as well as the low  $\alpha$  pilot model except perhaps within the circled regions. The high  $\alpha_0$  pilot model does a poor job of predicting pilot behavior even in high  $\alpha_0$  flight. This pilot does not significantly adapt his control strategy to match the changes in aircraft dynamics. Note that no conclusion regarding quadratic weight ("tight" or "normal" control effort-tracking error trade-off) can be made based on visual inspection of these figures.

The hypothesis testing results are shown in Fig. 48. Recall that these results take the form of a set of probabilities for each of the hypothesized pilot models, with the sum of the probabilities of all hypotheses in a given test equal to one. Allowing the hypothesis testing algorithm to choose between the low  $\alpha_0$  and medium  $\alpha_0$  pilot models results in the probability histories shown in Fig. 48a. The low  $\alpha_0$  model best matches the pilot's responses except in the circled regions. The hypothesis testing result confirms the qualitative analysis of the control time histories. The addition of the high  $\alpha_0$  pilot model (48b) to the set of hypotheses produces no change; at no time does the high  $\alpha_0$  model predict the actual pilot's behavior, even when the aircraft really is in a high  $\alpha_0$  flight condition.

Choice of pilot tracking error-control effort trade-off (quadratic weight level) could not be made from a visual examination of the control responses, but the hypothesis testing algorithm clearly indicates that the "normal" weights give a much better fit to the data than the "high" weights. This indicates that the "high-gain" or "tight" pilot model is not as good a representation of what the pilot actually did as is the normal or "low-gain" pilot model values.

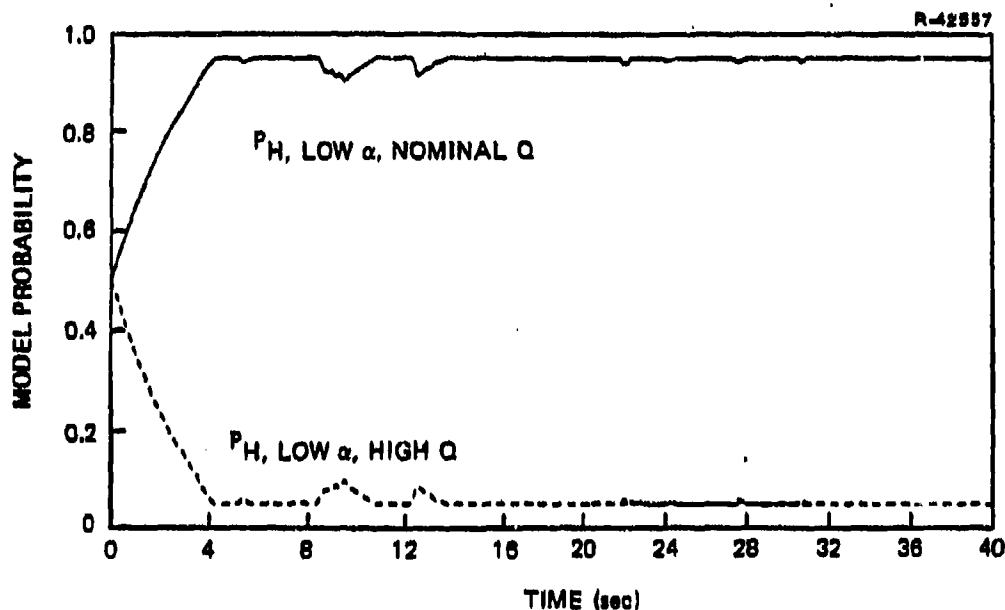


a) Comparison of Pilot Models at  $\alpha_0 = 5$  deg  
and  $\alpha_0 = 10$  deg



b) Comparison of Pilot Models at  $\alpha_0 = 5$  deg,  
 $\alpha_0 = 10$  deg and  $\alpha_0 = 20$  deg

Figure 48 Pilot Model Probabilities



c) Pilot Model at  $\alpha_0 = 5$  deg with  
Different Quadratic Weights

Figure 48 Pilot Model Probabilities (Continued)

These results apply to the pilot trajectory analyzed here. It is apparent that analysis of many more pilot trajectories is necessary before general conclusions can be made. Recall from Chapter 3 that the use of pedals at high  $\alpha_0$  to roll the F-14A is desirable. The pilot in this test was specifically requested not to use rudder pedals, and so it is not clear what this pilot's high- $\alpha_0$  responses would have been if pedals had been allowed.

#### 4.9 CHAPTER SUMMARY

Applications of the optimal control pilot model in Refs. 3 and 23 show great promise for expanding and understanding stability and performance characteristics of piloted aircraft in



maneuvering flight. The results in this chapter have substantiated these results by postprocessing simulated flight test data to determine actual control strategies used by a human pilot. The primary result is that the pilot, throughout most of the simulation studies, did not change his internal model of the aircraft's dynamics from a low angle of attack flight condition to others that the aircraft traversed; i.e., the pilot does not appear to adapt his control strategy to match changes in the aircraft's behavior. It is suggested that the reason the pilot did not adapt is the same as the reason given in Ref. 3 for the minimum control effort strategy. To adapt, the pilot would have to increase his control effort by subjectively increasing his feedback gains as shown in Table 17; increasing control effort is something pilots apparently try to avoid. The optimal control pilot model predicts control signals which closely match those of the actual pilot when the optimal control pilot model has a fixed low  $\alpha_0$  control strategy. The implications of these results are clear,

- If the pilot model's low angle of attack control strategy destabilizes the aircraft at high angles of attack then a human pilot will also have stability problems, since it cannot be assumed that he will adapt to the actual aircraft flight condition.
- An automatic control law (sas, cas, ARI, DFCS etc.) should be tested with a non-adapting pilot model to assess its capabilities. A very simple nonadapting pilot model is used in Chapter 3 to successfully test the DFCS designed in Chapter 2, for example.

A number of other results have been obtained in this study,

- A modified hypothesis testing scheme combined with a linear pilot model is developed that can be used to analyze nonlinear piloted aircraft data.
- The hypothesis testing scheme and the simple procedure used to handle total value aircraft states and controls (i.e., high-pass filtering) are successfully validated against computer generated synthetic data for which the true hypothesis is known
- The pursuit-tracking target/aircraft model developed in this report can be used in any future pilot-aircraft studies performed with (as in this study) or without (Refs. 3 and 23) pilot data to predict pilot control behavior. Specifically, lateral-directional and longitudinal tracking can be analyzed together to insure that all appropriate couplings are examined.

The hypothesis testing scheme with the optimal control pilot model has considerable room for improvement and continued analysis. Recommended extensions are outlined in Chapter 5.

5.

## CONCLUSIONS AND RECOMMENDATIONS

### 5.1 SUMMARY AND CONCLUSIONS

The main results of this report are that a digital flight control system for air combat can be constructed which demonstrates better handling qualities than a conventional control system along typical acm trajectories, and that it is possible to choose (from a set of pilot models) the pilot model that best matches actual pilot control motions.

Chapter 2 of this report is devoted to the construction of an Air Combat Digital Flight Control System (DFCS). This was demonstrated for the Grumman F-14A as an example. This DFCS exhibits the two major properties necessary for a command augmentation system:

- Modification of vehicle stability characteristics to provide frequency and damping that match MIL-F-8785B Level 1, Category A requirements at all flight conditions in the design regime.
- Modification of vehicle control response characteristics to provide fast and accurate response to pilot commands. Additionally, this response is uniform over the design regime.

It should be emphasized that the design regime spans the entire range of velocity, normal acceleration and roll rate expected in air combat maneuvering (ACM) flight. Sample rates and control calculation requirements are similar to those of a flight control algorithm designed by TASC that has been test flown as part of the NASA VALT program (Ref. 7).

Chapter 3 details the testing of the Air Combat DFCS against the conventional control system. A summary of the results and conclusions from these tests is as follows:

- The DFCS provides precise stability augmentation in steady turns and rapid rolling. The Dutch roll mode is well damped, and longitudinal maneuvers are quickened by the automatic maneuver flap feature built into the DFCS.
- The DFCS provides precise command response, with more accurate normal acceleration and much more accurate roll rate response. Automatic turn coordination operates by nulling sideslip excursions even in rapid maneuvering flight.
- The DFCS handles control saturation well, providing good stability and accurate command response right up to the performance bounds of the airframe. Control saturation is used by the DFCS (as is common in ACM flight) to produce rapid and accurate command response.
- Conventional piloting technique of the aircraft with a conventional mechanical control system produced a control-induced departure and incipient spin in one ACM test.
- Loss of lateral stick roll control power for the conventional control system in high- $\alpha$  requires the pilot to compensate by using rudder pedals. The DFCS does this automatically, enabling the same piloting technique to be used in all flight conditions.
- The DFCS can be implemented with conventional sensor inputs. Except for pilot control inputs, the present sensor suite should be sufficient.
- Tests of digital control of the present limited-authority sas actuators with the conventional pilot's mechanical control system gives preliminary indication that

most of the DFCS advantages can be gained by digital control of the present limited-authority sas actuators.

Chapter 4 of this report presents a method for evaluating actual pilot control actions (with data from the NASA Differential Maneuvering Simulator) with hypothesized pilot model predictions. The different pilot strategies tested here are adapted to low- $\alpha$ , medium- $\alpha$ , and high- $\alpha$  flight conditions. Also, a pilot model based on tight tracking error-high control effort is compared to a pilot model based on loose tracking error - lower control effort. The processing of piloted-simulation trajectory data led to the following results and conclusions:

- The hypothesis testing method can choose the candidate model even when differences are not apparent during visual inspection of the trajectories.
- The low angle of attack optimal control pilot model predicted the pilot input well, whereas the medium angle of attack model only appeared to be better in certain very short trajectory segments. The pilot's control strategy did not correspond to the high angle-of-attack model at all, even during high angle-of-attack flight.
- During the piloted-simulation evaluated here, the pilot did not adapt his control strategy to the angle-of-attack at which the aircraft was flying. Hence, a pilot/aircraft stability study such as that performed by TASC in Ref. 3 should provide useful information.

## 5.2 RECOMMENDATIONS

In the area of control system design, investigation of accelerometer feedbacks rather than aerodynamic angle feedback is desirable. This can be achieved by a digital estimator

which uses accelerometer output to estimate the aerodynamic angle feedbacks necessary in the present control algorithms, or the control algorithms can be designed for accelerometer feedbacks instead of aerodynamic angle feedbacks. Theoretical solutions to both approaches are available, with the second being desirable from a control system simplicity viewpoint. In any event, aerodynamic angles will still be necessary for gain scheduling. The choice between the two depends on sensor suite and sensor accuracy and noise properties. The output of this study would consist of control system designs better adapted to the present-day fighter sensor suites.

In the area of control system gain scheduling, a working ACM control system must be designed for additional types of flight conditions. The three parameters used in this study remain the most important (speed, normal acceleration, and roll rate), although the ranges may require some extension. The addition of flight conditions with different altitude, Mach number, cg location, and weight allows a determination of the importance of these effects and enables an examination of Air Combat DFCS performance changes due to these flight condition variations. The output of this task would be an evaluation of the importance of the various gain-scheduling parameters.

In the area of digital augmentation of a conventional aircraft, design of a version of the Air Combat sas optimized for operation through the limited-authority sas actuators should be aggressively pursued. This approach may provide a significant improvement in air combat handling qualities without major modification to the conventional mechanical control system. Retrofitting a digital sas computer during the F-14A CILOP program can possibly be justified by these improvements.

Previous aircraft stability and control studies and pilot-aircraft stability studies, along with the air combat

evaluation technique presented here form the basis of an analysis capability upon which an improved analog sas with aileron-rudder interconnect for good high angle-of-attack handling qualities can probably be designed. Although the handling qualities improvements are not likely to be as great for this approach as for the digital sas approach, the analysis tools do make this approach feasible.

Even though the pilot model testing performed in this study indicated that the pilot flying the aircraft simulation analyzed here did not adapt to the actual flight condition of the aircraft, it cannot be discerned whether this is typical of ACM pilots in general. Analysis of pilot data over many trajectories would be necessary. An additional data set generated by NASA Langley is available and can be examined using the pilot model hypothesis testing programs developed. There are a series of improvements to the approach used here which should be pursued in the event of additional pilot data analysis, the most important of which is improving the method used to select the pilot's internal model of the target driving covariance. This would enable the use of the Kalman filter's estimate of it's output error covariance in the hypothesis testing procedure. Other questions that can be answered in further data analyses include:

- Do other pilot models predict pilot response as accurately as the optimal control model?
- Does the pilot's control effort-tracking error trade-off vary along an ACM trajectory?
- Do different pilots exhibit different adaptation strategies or control effort-tracking error tradeoffs?
- Do additions to the pilot's observation set improve the pilot model's match of pilot response?

- In the multi-axis case, can attention allocation between axes be identified?

Some of these questions can be answered by further analysis of available data, while some of them require additional data.

More realistic target and target dynamics models can be incorporated in the piloted simulation analysis. While the analysis proceeded reasonably well, additional target data would reduce the need for simplifications to the target and target dynamics models made in Appendix B. It is not known if these simplifications reduced the accuracy of the pilot model analysis performed here; an investigation of more accurate models would answer this question.



## REFERENCES

1. Stengel, R.F., and Berry, P.W., "Stability and Control of Maneuvering High Performance Aircraft," Journal of Aircraft, Vol 14, August, 1977.
2. Stengel, R.F., Broussard, J.R., and Berry, P.W., "Command Augmentation Control Laws for Maneuvering Aircraft," AIAA Paper No. 77-1044, AIAA Guidance and Control Conference, August, 1977.
3. Stengel, R.F., Broussard, J.R., Berry, P.W., and Taylor, J.H., "Modern Methods of Aircraft Stability and Control Analysis," ONR-CR215-237-2, May, 1977.
4. Stengel, R.F., Broussard, J.R., and Berry, P.W., "Digital Controllers for VTOL Aircraft," IEEE Transactions on Aerospace and Electronic Systems, Vol. AES-14, January 1978.
5. Broussard, J.R., Berry, P.W., and Gully, S.W., "Synthesis of Digital Controllers for a Fighter Aircraft Using Continuous-Time Specifications," Proceedings of the Flight Control Systems Criteria Symposium, Naval Postgraduate School, Monterey, California, July 1978.
6. Broussard, J.R., Berry, P.W., and Gully, S.W., "Stability and Control Analyses of a V/STOL Type B Aircraft" The Analytic Sciences Corporation, Report No. TR-1259, February 1979.
7. Broussard, J.R., Berry, P.W., and Stengel, R.F., "Modern Digital Flight Control System Design for VTOL Aircraft," NASA Report CR-159019, March 1979.
8. Tomizuka, M., Auslander, D.M., and Takahashi, Y., "A Tutorial Introduction to Discrete Time Optimal Control" Winter Annual Meeting of the American Society of Mechanical Engineers, Paper No. 78-WA/DSC-18, December, 1978.
9. Huang, L.H., and Durbin, L.D., "Quadratic Error Based PI Control Features With Deadtime Processes" Proceedings of the 1978 Joint Automatic Control Conference, Philadelphia, October, 1978.

### REFERENCES (Continued)

10. Lee, W.H., Athans, M., Castanon, D., and Bacchiloloni, F., "Linear Tracking Systems With Applications To Aircraft Control System Design," M.I.T., Electronic Systems Laboratory, Report No., ESL-R-720, January 1977.
11. Smith, C.L., Digital Computer Process Control, Intex Educational Publishers, London, 1972.
12. Broussard, J.R., "Command Generator Tracking - The Discrete Time Case," The Analytic Sciences Corporation, Report No. TIM-612-3, March, 1978.
13. Davison, E.J., and Wang, S.H., "Properties and Calculation of Transmission Zeroes of Linear Multivariable Systems," Automatica, Vol. 10, No. 6 1974, pp. 643-658.
14. O'Brien, M.J., and Broussard, J.R., "Feedforward Control to Track the Output of a Forced Model" 17th IEEE Conference on Decision and Control, San Diego, California, January 1979.
15. Anon., "Flying Qualities of Piloted Airplanes," MIL-F-8785B (ASG), USAF/USN, August, 1969.
16. Kafer, G., Toles, R., and Golan, E., "Digital Control Laws for the Space Shuttle Orbiter ALT," Proceedings of the 1976 IEEE Decision and Control Conference, Clearwater, Florida, December 1976.
17. Vetsch, G.J., Landy, R.J., and Schaefer, D.B., "Digital Multimode Fly-By-Wire Flight Control System Design and Simulation Evaluation," Second Annual AIAA Digital Avionics Conference, AIAA Paper 77-1508, November 1977.
18. Dorato, P., and Levis, A.H., "Optimal Linear Regulators: The Discrete-Time Case," IEEE Transactions on Automatic Control, Vol. AC-16, No. 6 December 1971, pp. 613-620.
19. Gran, R., Berman, H., and Rossi, M., "Optimal Digital Flight Control For Advanced Fighter Aircraft," Journal of Aircraft, Vol. 14, No. 1, January 1977, pp. 32-37.
20. Keskar, D.A., and Slater, G.L., "Load Factor Response of Digitally Control Aircraft" AIAA Paper No. 77-1080, AIAA Guidance and Control Conference, August, 1977.

REFERENCES (Continued)

21. Bihrlle, W. "F-14A Air Combat Maneuvering System", Proceedings of the Symposium on Control Theory and Navy Applications, Monterey, CA, July 1975.
22. Lindahl, J.H., "Application of the Automatic Rudder Interconnect (ARI) Function in the F-14 Aircraft," Proceedings of the Symposium on Control Theory and Navy Applications, Monterey, CA, July 1975.
23. Stengel, R.F., Taylor, J.H., Broussard, J.R., and Berry, P.W., "High Angle of Attack Stability and Control", ONR-CR215-237-1, April, 1976.
24. Communications with Naval Air Development Center personnel.
25. Brown, D.Q., "Accelerated Testing Set for F-14A", Aviation Week and Space Technology, December 1971, pp. 49 to 53.
26. Kleinman, D.L., Baron, S., and Levison, W.H., "A Control Theoretic Approach to Manned-Vehicle Systems Analysis," IEEE Trans. on Automatic Control, Vol. AC-16, No. 6, December 1971.
27. Kleinman, D.L. and Baron, S., "Manned Vehicle Systems Analysis by Means of Modern Control Theory," Bolt Beranek and Newman, Inc., Cambridge, Mass., BBN Rep. 1967, June 1970.
28. Communications with NASA Langley Research Center personnel.
29. Communications with Naval Air Test Center personnel.
30. Fiske, P.H., "Advanced Estimation and Control Concepts for Air-to-Air Missile Guidance", The Analytic Sciences Corporation, Report No. TR-1353-1, February 1979.
31. Fiske, P.H., and Price, C.F., "A New Approach to Model Structure Identification," AIAA Atmospheric Flight Mechanics Conference, Paper No. 77-1171, Hollywood, Florida, August 1977.
32. Jagacinski, R.J., and Miller, R.A., "Describing the Human Operator's Internal Model of a Dynamic System," Human Factors, Vol. 20 No. 4, 1978.
33. Bengtsson, G., "Output Regulation and Internal Models - A Frequency Domain Approach", Automatica, Vol. 13, No. 4, July 1977.

### REFERENCES (Continued)

34. Baron, S., and Berliner, J., "The Effects of Deviate Internal Representations In the Optimal Model of The Human Operator," IEEE 1976 Decision and Control Conference, Clearwater, Florida, December 1976.
35. Rao, P.K., Kleinman, D.L., and Ephrath, A.R., "Adaptive Estimation Schemes for Minimizing Uncertainty in Manual Control Tasks", 17th IEEE Conference on Decision and Control, San Diego, California, January 1978.
36. Harvey, T.R. and Dillow, J.D., "Fly and Fight: Predicting Piloted Performance in Air-to-Air Combat," Proceedings of the 10th Annual Conference on Manual Control, Wright-Patterson AFB, April 9-11, 1974.
37. Korn, J., Boal, H.S., and Vikmanis, M., "Modeling Human Tracking Performance in a High G-Stress Environment", 17th IEEE Conference on Decision and Control, San Diego, California, January, 1979.
38. Glickman, H., Muller, W., and Gertz, D., "Implementation of Automatic Turn Coordination in Grumman Aircraft", Proceedings of the Flight Control Systems Criteria Symposium, Naval Postgraduate School, Monterey, CA, July 1978.
39. Beauchamp, K.G., Signal Processing Using Analog and Digital Techniques, John Wiley & Sons, New York, 1973.

## APPENDIX A

### AIRCRAFT EQUATIONS OF MOTION

#### A.1 OVERVIEW

This appendix reviews the equations of motion for a maneuvering aircraft. These derivations make extensive use of vector-matrix differential equation ("state-space") notation, and the resulting equations are written in a form suitable for analysis using concepts of modern control theory.

#### A.2 NONLINEAR DYNAMIC EQUATIONS

The derivation of nonlinear rigid-body equations is reviewed in this section. The equations are developed using "flat-earth" assumptions, i.e., the effects of earth curvature and rotation are assumed negligible. This means that earth-fixed and inertial reference frames are equivalent.

For the moderate velocities of interest in this report (typically below 305 m/s (1000 fps)), the equivalence of earth-fixed and inertial reference frames is a good assumption. The origin of the inertial reference frame used here is located on the surface of the earth, with the x-, y-, and z-axes in a north-east-down orientation. Since the simplest statement of Newton's Second Law is given in an inertial reference frame, this frame plays an important part in the derivation of the dynamic equations.

For point-mass analysis, the velocity reference frame is convenient. The origin lies at the cg of the vehicle, and the x-axis points along the velocity vector. The y-axis is horizontal and the z-axis lies in the vertical plane which includes the x-axis. The velocity heading angle,  $\xi$ , describes the heading of the projection of the velocity x-axis on the horizontal plane relative to north, and the flight path angle,  $\gamma$ , describes the inclination of the velocity vector relative to the horizontal.

The wind axes also include an x-axis along the velocity vector, but the z-axis lies in the plane of symmetry of the vehicle veing described. Hence, as the vehicle rolls about the velocity vector, the wind axes roll also. The roll angle relative to the velocity axes is  $\phi_v$ .

Detailed vehicle state equations can best be expressed in body-fixed rather than velocity-fixed axes. These are the axes in which the pilot, the sensors, and the control surface locations are defined. Body axes are the only axes in which the moment-of-inertia matrix is constant, and also dynamic data collected from sting-mounted wind tunnel models or from flight tests usually are expressed in body axes.

The various body-fixed axis systems have a common origin, located at the body center of mass, and are fixed in orientation with respect to the vehicle. Generally, the body x-axis extends forward out the vehicle's nose, the y-axis extends out the right wing, and the z-axis extends out the bottom of the vehicle. The x-z plane is usually a plane of geometric symmetry, if the vehicle has one. There are a number of possible body-fixed reference frames, and the one fixed by the builder is simply referred to in this report as the body-axis system. For any nominal flight condition, body-fixed axes can be chosen

so that the x-axis is aligned with the velocity vector, and the z-axis is in the body-axis plane. This set of body-fixed axes is referred to as the stability-axis system.

A transformation from inertial to body axes is composed of a right-handed yaw through an angle  $\psi$ , then a right-handed pitch through an angle  $\theta$ , and then a right-handed roll through an angle  $\phi$ . The body axes and wind axes are related to each other through the aerodynamic angles, angle of attack,  $\alpha$ , and angle of sideslip,  $\beta$ . Angle of attack represents the aircraft body pitch angle above the velocity vector, and sideslip is the angle that the aircraft nose is yawed left of the velocity vector.

In summary, the inertial axes, body axes, wind axes and velocity axes can be related to each other by the transformations illustrated in Fig. A.1. The inertial-to-body-axis transformation proceeds as follows:

$$H_I^B(\phi, \theta, \psi) = H_2^B(\phi) H_1^2(\theta) H_I^1(\psi)$$

$$= \begin{bmatrix} 1 & 0 & 0 \\ 0 & \cos\phi & \sin\phi \\ 0 & -\sin\phi & \cos\phi \end{bmatrix} \begin{bmatrix} \cos\theta & 0 & -\sin\theta \\ 0 & 1 & 0 \\ \sin\theta & 0 & \cos\theta \end{bmatrix} \begin{bmatrix} \cos\psi & \sin\psi & 0 \\ -\sin\psi & \cos\psi & 0 \\ 0 & 0 & 1 \end{bmatrix}$$

(A-1)

For orthonormal matrices such as these, the matrix inverse,  $( )^{-1}$ , is equal to the transpose,  $( )^T$ . Equation A-2 illustrates the inertial-to-velocity axis transformation matrix.

$$H_I^V(\gamma, \xi) = H_{LH}^V(\gamma) H_I^{LH}(\xi)$$

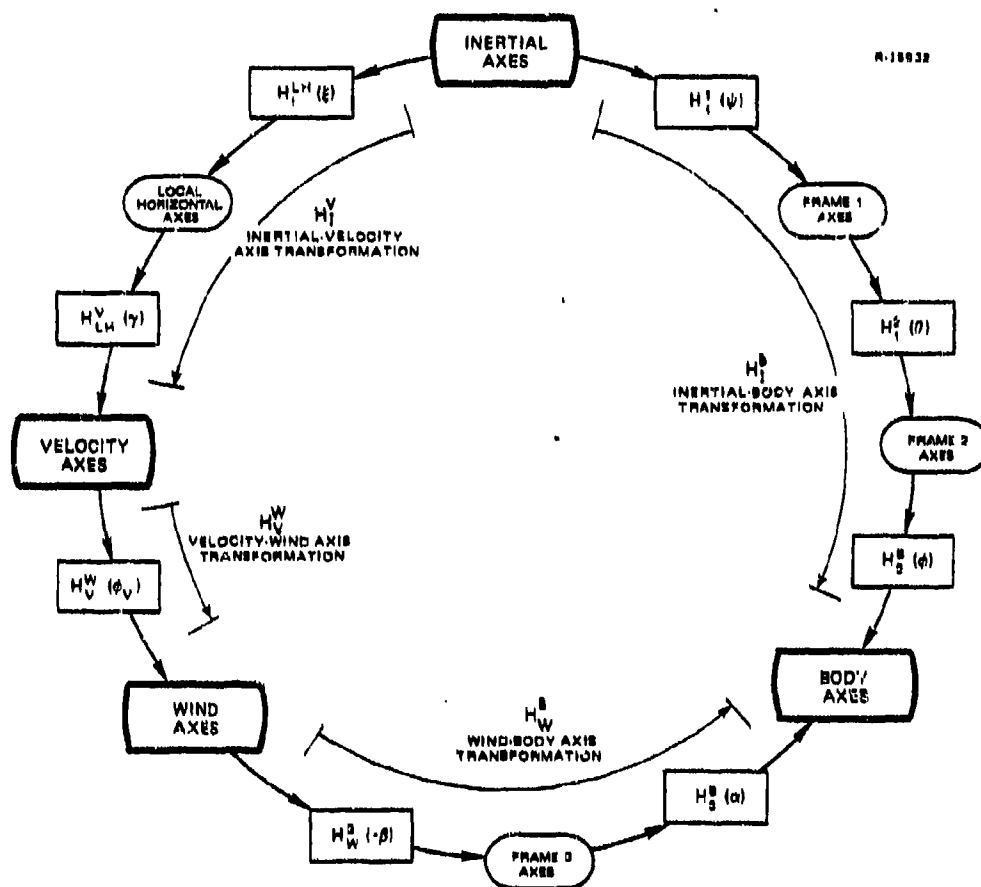


Figure A-1 Reference Axis Transformations (Arrows Indicate Right-Hand Rotation)

$$= \begin{bmatrix} \cos \gamma & 0 & -\sin \gamma \\ 0 & 1 & 0 \\ \sin \gamma & 0 & \cos \gamma \end{bmatrix} \begin{bmatrix} \cos \xi & \sin \xi & 0 \\ -\sin \xi & \cos \xi & 0 \\ 0 & 0 & 1 \end{bmatrix} \quad (A-2)$$

The velocity-to-wind axis transformation is defined by

$$H_V^W(\phi_V) = \begin{bmatrix} 1 & 0 & 0 \\ 0 & \cos \phi_V & \sin \phi_V \\ 0 & -\sin \phi_V & \cos \phi_V \end{bmatrix} \quad (A-3)$$



and the wind-body transformation matrix is given by

$$H_W^B(\alpha, -\beta) = H_3^B(\alpha) H_W^3(-\beta)$$

$$\begin{bmatrix} \cos \alpha & 0 & -\sin \alpha \\ 0 & 1 & 0 \\ \sin \alpha & 0 & \cos \alpha \end{bmatrix} \begin{bmatrix} \cos \beta & -\sin \beta & 0 \\ \sin \beta & \cos \beta & 0 \\ 0 & 0 & 1 \end{bmatrix} \quad (A-4)$$

In the remainder of this section, the vehicle's equation of motion is derived as a single state-vector equation of the form

$$\dot{\underline{x}} = \underline{f}(\underline{x}, \underline{u}) \quad (A-5)$$

where  $\underline{x}$  is the state vector,  $\underline{u}$  is the control vector,  $\underline{f}$  is the vector system dynamics equation, and disturbances are neglected. The state vector is a 12-element vector, and the nonlinear state equations are readily derived as four sets of three equations representing

- Translational Kinematics
- Rotational Kinematics
- Translational Dynamics
- Rotational Dynamics.

The kinematic equations relate the vehicle's translational and rotational velocities to its position in inertial space, and thus involve body-axis/inertial-axis relationships. The dynamic equations describe the changes of the vehicle velocity components caused by the applied forces and moments; they are best derived in a body-fixed frame of reference.

A second nonlinear vector equation is also derived to relate the output of the aircraft to its state and control. The output equation,

$$y = h(\underline{x}, \underline{u}) \quad (A-6)$$

is necessary in any control design problem because the goal of control system design is to cause the output to follow a desired trajectory. The specific components of the output vector depend on the vehicle and the tactical situation.

#### A.2.1 Kinematics

The translational and angular position of the vehicle are given relative to inertial space by the inertial position vector,  $\underline{x}_I$  and by the inertial-body Euler angle vector,  $\underline{v}_B$ :

$$\underline{x}_I = \begin{bmatrix} x_I \\ y_I \\ z_I \end{bmatrix} \quad (A-7)$$

$$\underline{v}_B = \begin{bmatrix} \phi \\ \theta \\ \psi \end{bmatrix} \quad (A-8)$$

It is important to note that the Euler angle "vector" is not a true vector in physical space; it is an ordered triple of right-handed rotations which occur about different axes of different reference frames.

The translational and angular rate vectors often are expressed in body axes, as in the following:

$$\underline{v}_B = \begin{bmatrix} u \\ v \\ w \end{bmatrix} \quad (A-9)$$

$$\underline{\omega}_B = \begin{bmatrix} p \\ q \\ r \end{bmatrix} \quad (A-10)$$

The body-axis translational rate vector,  $\underline{v}_B$ , is an expression, in body axes, of the derivative of the inertial position vector. This relationship supplies the first part of the nonlinear state equations of motion

$$\dot{\underline{x}}_I = H_B^I \underline{v}_B \quad (A-11)$$

where  $H_B^I$  is the inverse of the inertial-body transformation derived in Eq. (A-1).

The body angular rate vector also can be related to the derivative of the Euler angle vector by noting that the Euler angle derivatives occur in three different reference frames. The resulting transformation is constructed in Eq. (A-12), where the individual transformations are the same as those of Eq. (A-1):

$$\begin{aligned} \underline{\omega}_B &= \begin{bmatrix} \dot{\phi} \\ 0 \\ 0 \end{bmatrix} + H_2^B \begin{bmatrix} 0 \\ \dot{\theta} \\ 0 \end{bmatrix} + H_2^B H_1^2 \begin{bmatrix} 0 \\ 0 \\ \dot{\psi} \end{bmatrix} \\ &= L_B \dot{\underline{\psi}}_B \end{aligned} \quad (A-12)$$

In this equation,

$$L_B = \begin{bmatrix} 1 & 0 & -\sin \theta \\ 0 & \cos \phi & \sin \phi \cos \theta \\ 0 & -\sin \phi & \cos \phi \cos \theta \end{bmatrix}$$

The ordering of the transformations in Eq. (A-12) arises from the ordering of the Euler angles. As can be seen from Fig. A-1, the angular rate,  $\dot{\phi}$ , occurs about the  $x_B$  axis; the rate  $\dot{\theta}$ , occurs about the  $y_2$  axis; and  $\dot{\psi}$  occurs about the  $z_1$  axis. The inverse of Eq. (A-11) supplies the rotational kinematic part of the vehicle nonlinear state equations, and it is given by:

$$\dot{\underline{v}}_B = L_B^{-1} \underline{\omega}_B^I \quad (A-13)$$

### A.2.2 Dynamics

The dynamics of the vehicle involve Newton's Second Law, which equates the applied force to the time derivative of inertial translational momentum of a body. For rotational motion, this equivalence becomes one between torque and the derivative of angular momentum, measured in an inertial reference frame.

An expression for the inertial translational acceleration, expressed in body-axis variables, can be derived from Eq. (A-10) by taking the derivative of both sides:

$$\dot{\underline{x}}_I = H_B^I \dot{\underline{v}}_B + \dot{H}_B^I \underline{v}_B \quad (A-14)$$

Here,

$$\dot{H}_B^I = H_B^I \tilde{\omega}_B \quad (A-15)$$

and  $\tilde{\omega}_B$  is the cross-product equivalent matrix for  $\underline{\omega}_B$  given by

$$\tilde{\omega}_B = \begin{bmatrix} 0 & -r & q \\ r & 0 & -p \\ -q & p & 0 \end{bmatrix} \quad (A-16)$$

This leads to the body axis equation

$$\dot{\underline{v}}_B = H_{I \underline{x}}^B - \tilde{\omega}_B \underline{v}_B \quad (A-17)$$

The applied specific forces consist of gravitational forces and contact forces. In inertial axes, the gravity force is

$$\underline{g}_I = \begin{bmatrix} 0 \\ 0 \\ g \end{bmatrix} \quad (A-18)$$

The specific contact force can be broken into two components, one of which is due to aerodynamic forces,  $\underline{F}_B$ , and one of which is due to thrust,  $\underline{T}_B$ :

$$\underline{F}_B/m = \begin{bmatrix} X/m \\ Y/m \\ Z/m \end{bmatrix} \quad (A-19)$$

$$\underline{T}_B/m = \begin{bmatrix} T_{B_x}/m \\ T_{B_y}/m \\ T_{B_z}/m \end{bmatrix} \quad (A-20)$$

(Capital letters are conventionally used in aerodynamics to denote the force components.) The specific equations for the aerodynamic and thrust forces are given in Ref. 23.

The translational dynamic equation is formed by equating the sum of the aerodynamic and gravitational specific forces to the inertial translational acceleration of the vehicle. Then Eq. (A-17) becomes

$$\dot{\underline{v}}_B = (\underline{F}_B + \underline{T}_B)/m + H_I^B \underline{g}_I - \tilde{\omega}_B \underline{v}_B \quad (A-21)$$

To construct the rotational dynamic equation, an expression for the time derivative of angular momentum measured in inertial axes is necessary. The angular momentum,  $\underline{h}_B$ , is most easily expressed in body axes; neglecting rotating machinery, it is the product of the moment-of-inertia matrix (constant in body axes) and the angular rate vector

$$\underline{h}_B = I_B \underline{\omega}_B \quad (A-22)$$

where the inertia matrix contains all products and moments of inertia:

$$I_B = \begin{bmatrix} I_x & -I_{xy} & -I_{xz} \\ -I_{xy} & I_y & -I_{yz} \\ -I_{xz} & -I_{yz} & I_z \end{bmatrix} \quad (A-23)$$

The time derivative of the angular momentum, expressed in inertial axes, is derived as

$$\begin{aligned} \dot{\underline{h}}_I &= H_B^I I_B \dot{\underline{\omega}}_B + \dot{H}_B^I I_B \underline{\omega}_B \\ &= H_B^I I_B \dot{\underline{\omega}}_B + H_B^I \tilde{\omega}_B I_B \underline{\omega}_B \end{aligned} \quad (A-24)$$

The contact moments consist of aerodynamic and thrust components. These are defined as

$$\underline{M}_B = \begin{bmatrix} L \\ M \\ N \end{bmatrix} \quad (A-25)$$

$$\underline{G}_B = \begin{bmatrix} G_{B_x} \\ G_{B_y} \\ G_{B_z} \end{bmatrix} \quad (A-26)$$

(Capital letters are conventionally used for the moment components.) The specific equations for the aerodynamic and thrust moments are given in Ref. 23. The rotational dynamic equation is formed by equating the applied torques to the derivative of the angular momentum:

$$\dot{\underline{\omega}}_B = \underline{I}_B^{-1}(\underline{M}_B + \underline{G}_B) - \underline{I}_B^{-1} \tilde{\underline{\omega}}_B \underline{I}_B \underline{\omega}_B \quad (A-27)$$

### A.2.3 Summary of State Equations

The nonlinear state equations are

$$\dot{\underline{x}}_I = \underline{H}_B^I \underline{v}_B \quad (A-28)$$

$$\dot{\underline{v}}_B = \underline{L}_B^{-1} \underline{w}_B \quad (A-29)$$

$$\dot{\underline{v}}_B = (\underline{F}_B + \underline{T}_B)/m + \underline{H}_I^B \underline{g}_I - \tilde{\underline{\omega}}_B \underline{v}_B \quad (A-30)$$

$$\dot{\underline{w}}_B = I_B^{-1}(\underline{M}_B + \underline{G}_B) - I_B^{-1}\underline{\tilde{w}}_B I_B \underline{w}_B \quad (\text{A-31})$$

These equations fall into the general state equation form

$$\dot{\underline{x}} = \underline{f}(\underline{x}, \underline{u}) \quad (\text{A-32})$$

by defining the state vector as

$$\underline{x}^T = \left[ \underline{x}_I^T \quad \underline{v}_B^T \quad \underline{v}_B^T \quad \underline{w}_B^T \right] \quad (\text{A-33})$$

and noting that the aerodynamic forces and moments are functions of the states, controls, disturbances and, to some extent, the state history.

#### A.2.4 Output Equations

The output vector,  $\underline{y}$ , consists in general of nonlinear functions of the aircraft states,  $\underline{x}$ , and controls,  $\underline{u}$ , and is given by

$$\underline{y} = \underline{h}(\underline{x}, \underline{u}) \quad (\text{A-34})$$

For a conventional fighter aircraft, the four basic commanded motions are longitudinal, lateral, normal, and directional motions. Longitudinal motion results in a velocity magnitude change and can be commanded by  $V$  or  $\dot{V}$ . Lateral (rolling) motion is used to orient the maneuver plane and can be commanded by  $p$ ,  $p_w$ , or  $\phi$ . Normal and directional plane motions are two degree-of-freedom motions, and, in general, require two commands. In the normal plane, acceleration ( $a_n$  or  $q$ ) and/or attitudes ( $\theta$ ,  $\alpha$ , or  $\gamma$ ) can be commanded, with the two-element directional command vector chosen in an analogous way. All of these commands are desirable in one situation or



another. In ground attack, both flight path control ( $\gamma$ ) and independent fuselage pointing ( $\alpha$ ) might be desirable. In air combat maneuvering, normal acceleration ( $a_n$ ) is certainly a useful command, as is stability-axis rollrate ( $p_w$ ). Output equations for each of these quantities are needed so that they can be used in control system design.

The aircraft velocity and the aerodynamic angles are given in terms of the body axis velocities as follows

$$\begin{bmatrix} V \\ \beta \\ \alpha \end{bmatrix} = \begin{bmatrix} \sqrt{u^2 + v^2 + w^2} \\ \tan^{-1} (v/\sqrt{u^2 + w^2}) \\ \tan^{-1} (w/u) \end{bmatrix} \quad (\text{A-35})$$

The three components of earth-relative acceleration expressed in wind axes are given in terms of body-axis quantities as follows

$$\begin{bmatrix} \dot{V} \\ a_y \\ -a_n \end{bmatrix} = H_I^W \underline{\dot{x}}_I = H_I^W(\alpha, \beta) \begin{bmatrix} \dot{v}_B + \tilde{\omega}_B v_B \end{bmatrix} \quad (\text{A-36})$$

where it should be noted that these quantities are different than those usually named  $a_y$  and  $a_n$ , as the acceleration of gravity is included in these terms. Hence, a command system set up on this basis automatically compensates for gravity.

The earth-relative acceleration in wind axes can also be specified in terms of the velocity-axis angular rates as follows

$$H_I^W \underline{\dot{x}}_I = H_V^W H_I^V \underline{\dot{x}}_I$$

$$= \begin{bmatrix} 1 & 0 & 0 \\ 0 & \cos\phi_V & \sin\phi_V \\ 0 & -\sin\phi_V & \cos\phi_V \end{bmatrix} \begin{bmatrix} 1 & 0 & 0 \\ 0 & V\cos\gamma & 0 \\ 0 & 0 & -V \end{bmatrix} \begin{bmatrix} \dot{V} \\ \dot{\xi} \\ \dot{\gamma} \end{bmatrix} \quad (A-37)$$

The second two equations result in the following equations describing the velocity angle dynamics

$$V \cos\gamma \dot{\xi} = a_y \cos\phi_V + a_n \sin\phi_V \quad (A-38)$$

$$V \dot{\gamma} = -a_y \sin\phi_V + a_n \cos\phi_V$$

The wind-axis roll rate is the first component of the body angular velocity expressed in wind axes, which is

$$\begin{bmatrix} p_w \\ q_w \\ r_w \end{bmatrix} = H_B^W(\alpha, \beta) \underline{\omega}_B \quad (A-39)$$

Equations relating the body angular rate in wind axes to the aerodynamic and velocity angular rates can be derived with reference to Fig. A-1.

$$\begin{bmatrix} p_w \\ q_w \\ r_w \end{bmatrix} = H_V^W(\phi_V) H_{LH}^V(\gamma) \begin{bmatrix} 0 \\ 0 \\ \dot{\xi} \end{bmatrix} + H_V^W(\phi_V) \begin{bmatrix} 0 \\ \dot{\gamma} \\ 0 \end{bmatrix}$$

$$+ \begin{bmatrix} \dot{\phi}_V \\ 0 \\ 0 \end{bmatrix} + \begin{bmatrix} 0 \\ 0 \\ -\dot{\beta} \end{bmatrix} + H_3^W(-\beta) \begin{bmatrix} 0 \\ \dot{\alpha} \\ 0 \end{bmatrix} \quad (A-40)$$

which results in

$$\begin{bmatrix} p_w \\ q_w \\ r_w \end{bmatrix} = \begin{bmatrix} \dot{\phi}_V - \xi \sin \gamma + \dot{\alpha} \sin \beta \\ \xi \cos \gamma \sin \phi_V + \dot{\gamma} \cos \phi_V + \dot{\alpha} \cos \beta \\ \xi \cos \gamma \cos \phi_V + \dot{\gamma} \sin \phi_V - \dot{\beta} \end{bmatrix} \quad (A-41)$$

These last equations are useful in deriving simple ACM pilot models and setting up point-mass aircraft trajectory generators. The earth-relative velocity and the inertial-velocity angles are also candidates for inclusion in command systems. The equations are given below.

$$\begin{bmatrix} \dot{x}_I \\ \dot{y}_I \\ \dot{z}_I \end{bmatrix} = H_B^I(\psi, \theta, \phi) \begin{bmatrix} u \\ v \\ w \end{bmatrix} \quad (A-42)$$

$$\begin{bmatrix} V \\ \xi \\ \gamma \end{bmatrix} = \begin{bmatrix} \sqrt{\dot{x}_I^2 + \dot{y}_I^2 + \dot{z}_I^2} \\ \arccos \left( \dot{x}_I \sqrt{\dot{x}_I^2 + \dot{y}_I^2} \right) \\ \arcsin \left( -\dot{z}_I \sqrt{\dot{x}_I^2 + \dot{y}_I^2 + \dot{z}_I^2} \right) \end{bmatrix} \quad (A-43)$$

For a fighter pilot requiring rapid sustained orientation changes, an acceleration-oriented maneuvering set,

$$\underline{y}_d = \left[ V, a_n, \alpha, \beta, a_y, p_w \right]^T \quad (A-44)$$

could be useful. The maneuvering set gives the pilot direct control over normal acceleration,  $a_n$ , and roll rate about the velocity vector,  $p_w$ . Independent fuselage pointing is provided about the velocity vector using angle of attack,  $\alpha$ , and sideslip,  $\beta$ , commands. The air-relative velocity magnitude,  $V$ , is commanded, and the aircraft can be directed to make a flat turn (no bank angle) with the lateral acceleration,  $a_y$ , command.

### A.3 LINEAR DYNAMIC EQUATIONS

For aircraft stability and control response analysis, linearized versions of the nonlinear state and output equations are necessary. The linearized aircraft state equations are given in Ref. 23, along with a description of the linearized aerodynamic force and moment relationships. Linearization of the output equations described in Section A.2.4 is given here.

The command augmentation system design methods of Chapter 4 require linearized versions of the output vector, which is a function of both aircraft states and controls, so the following perturbation output vector equation results:

$$\Delta \underline{y}_d = H(\underline{x}_0, \underline{u}_0) \Delta \underline{x} + D(\underline{x}_0, \underline{u}_0) \Delta \underline{u} \quad (A-45)$$

The individual rows of  $H$  and  $D$  depend on the chosen elements of the command vector, and the following equations describe the available constituents. The perturbation wind-axis velocity vector is related to the perturbation body-axis velocity vector as

$$\begin{bmatrix} \Delta V \\ \Delta \beta \\ \Delta \alpha \end{bmatrix} = J_W^{-1}(V_o, \beta_o) H_B^W(\alpha_o, \beta_o) \Delta \underline{v}_B \quad (A-46)$$

$J_W$  is a diagonal matrix which has elements 1,  $V_o$ , and  $V_o \cos \beta_o$ .

The following linearized output equation gives the relationship between the body-axis state variables and the perturbation wind-axis accelerations:

$$\begin{bmatrix} \Delta \dot{v} \\ \Delta a_y \\ \Delta a_n \end{bmatrix} = H_B^W(\alpha_o, \beta_o) \left\{ \Delta \dot{\underline{v}}_B + \tilde{\omega}_{B_o} \Delta \underline{v}_B - \tilde{v}_{B_o} \Delta \underline{\omega}_B \right. \\ \left. - \left[ \dot{\underline{v}}_{B_o} + \tilde{\omega}_{B_o} \underline{v}_{B_o} \right] L_W(\alpha_o) J_W^{-1}(V_o, \beta_o) H_B^W(\alpha_o, \beta_o) \Delta \underline{v}_B \right\} \quad (A-47)$$

where

$$L_W(\alpha_o) = \begin{bmatrix} 0 & \sin \alpha_o & 0 \\ 0 & 0 & 1 \\ 0 & -\cos \alpha_o & 0 \end{bmatrix} \quad (A-48)$$

These equations are easily evaluated using general computer routines that have been developed for this type of analysis. Equation A-47 requires both the nominal and perturbation body-axis velocity derivatives,  $\dot{\underline{v}}_{B_o}$  and  $\Delta \dot{\underline{v}}_B$ .  $\dot{\underline{v}}_{B_o}$  is part of the nominal flight condition specification, while  $\Delta \dot{\underline{v}}_B$  consists of three rows of the linear system differential equation. Introducing these three rows causes the accelerations to be functions

of the perturbation Euler angles, body-axis translational and angular rates, and the perturbation control deflections.

The perturbation wind-axis roll rate depends on both the perturbation body-axis angular rate and on the perturbation body-axis velocity, which affects the body-to-wind axis transformation matrix. The linearized equations for body angular rate in wind axes are as follows

$$\begin{bmatrix} \Delta p_w \\ \Delta q_w \\ \Delta r_w \end{bmatrix} = H_B^W(\alpha_o, \beta_o) \Delta \underline{\omega}_B - H_B^W(\alpha_o, \beta_o) \tilde{\omega}_B L_W(\alpha_o) J_W^{-1}(V_o, \beta_o) H_B^W(\alpha_o, \beta_o) \Delta \underline{v}_B \quad (A-49)$$

Linearization of the wind axis quantities  $\dot{V}, \dot{\xi}, \dot{\gamma}$ , and  $\dot{\phi}_v$  can best be pursued by regarding them as the state rates in a system whose input consists of the commanded values of  $\dot{V}, a_n, a_y$  and  $p_w$ . Assume  $\beta_o = 0$ . The linear state equations are

$$\begin{bmatrix} \Delta \dot{V} \\ \Delta \dot{\xi} \\ \Delta \dot{\gamma} \\ \Delta \dot{\phi}_v \end{bmatrix} = \begin{bmatrix} 0 & 0 & 0 & 0 \\ (-\dot{\xi}_o/V_o) & 0 & (\dot{\xi}_o/\tan \gamma_o) & (\dot{\gamma}_o/\cos \gamma_o) \\ (-\dot{\gamma}_o/V_o) & 0 & 0 & (-\dot{\xi}_o \cos \gamma_o) \\ (-\dot{\xi}_o \sin \gamma_o) & 0 & (\dot{\xi}_o/\cos \gamma_o) & (\dot{\gamma}_o \tan \gamma_o) \end{bmatrix} \begin{bmatrix} \Delta V \\ \Delta \xi \\ \Delta \gamma \\ \Delta \phi_v \end{bmatrix} + \begin{bmatrix} 1 & 0 & 0 & 0 \\ 0 & (\cos \phi_{v_o}/(V_o \cos \gamma_o)) & (\sin \phi_{v_o}/(V_o \cos \gamma_o)) & 0 \\ 0 & (-\sin \phi_{v_o}/V_o) & (\cos \phi_{v_o}/V_o) & 0 \\ 0 & (\tan \gamma_o \cos \phi_{v_o}/V_o) & (\tan \gamma_o \sin \phi_{v_o}/V_o) & 1 \end{bmatrix} \begin{bmatrix} \Delta \dot{V}_c \\ \Delta a_y \\ \Delta a_n \\ \Delta p_w \end{bmatrix} \quad (A-50)$$

An additional portion of the linearized relationships deals with the aircraft control system. Only the yaw sas is modeled in the pilot-model testing work, as the roll cas is off and the longitudinal dynamics are not analyzed. As shown in Fig. 23, the yaw sas feeds back washed-out yaw rate and low-pass-filtered lateral accelerometer output. The low-pass filter bandwidth is very large and hence the filter is modeled as a simple gain. Hence, the yaw sas adds one state to the aircraft model. The yaw sas actuator deflection is given by the equation

$$\delta_{r,sas} = k_1 a_y + k_2 r - k_2 \Delta x_{sas} \quad (A-51)$$

and the yaw sas state equation is

$$\dot{\Delta x}_{sas} = (-1/\tau)\Delta x_{sas} + (1/\tau)r \quad (A-52)$$

where  $\tau$  is the yaw rate washout time constant,  $k_1$  is the lateral acceleration feedback gain and  $k_2$  is the yaw rate feedback gain.

## APPENDIX B

### AIR COMBAT EQUATIONS OF MOTION

The full-order, nonlinear equations of motion for the tracking dynamics model in the air combat scenario are developed in this section. Simplified linear equations of the nonlinear tracking dynamics model, amenable to computer analysis, are also derived for use in Chapter 4. The addition of pipper dynamics, although not needed in this work, is a straightforward extension of this approach.

The target tracking angles are defined as the pilot's view angles relative to the aircraft x-axis. These angles,  $\epsilon_n$  and  $\epsilon_y$ , are shown in Fig. 44b. Derivation of the tracking angle dynamics best occurs in the wind axis system because it is aligned with the velocity vector. By expressing the target-to-tracking aircraft displacement vector in wind axes and dividing by the target-aircraft range, the tracking angle equation results:

$$\underline{v}_{WT} = \frac{1}{R} \{ H_I^W (\underline{x}_{I,T} - \underline{x}_I) \} \quad (B-1)$$

where, for relatively small wind axes angles,

$$\underline{v}_{WT} = \begin{bmatrix} R/R \\ -(\epsilon_y + \beta) \\ -(\epsilon_n + \alpha) \end{bmatrix} \quad (B-2)$$

The derivative of the tracking angle equation follows directly (assuming  $\dot{R} = 0$ )



$$\dot{\underline{x}}_{WT} = \frac{1}{R} \{ H_I^W (\dot{\underline{x}}_{I,T} - \dot{\underline{x}}_I) \} + \frac{1}{R} \{ \dot{H}_I^W (\underline{x}_{I,T} - \underline{x}_I) \} \quad (B-3)$$

The aircraft velocity in wind axes, by definition, is

$$H_I^W \dot{\underline{x}}_I = \begin{bmatrix} V \\ 0 \\ 0 \end{bmatrix} \quad (B-4)$$

and one can define the target's velocity relative to the tracking aircraft velocity as follows

$$H_I^W \dot{\underline{x}}_{I,T} = \begin{bmatrix} V + \delta V_x \\ \delta V_y \\ \delta V_z \end{bmatrix} \quad (B-5)$$

The second term in Eq. B-3 can be redefined in terms of a cross-product of the tracking angle vector ( $\underline{v}_{VT}$ ) and the wind-axis angular rates. The lateral and normal tracking angle dynamic equations finally result

$$\dot{\epsilon}_y = -\delta V_y/R + (\epsilon_n + \alpha)(p_w - \dot{\alpha} \sin \beta) + a_y/V - \dot{\beta} \quad (B-6)$$

and

$$\dot{\epsilon}_n = -\delta V_z/R - (\epsilon_y + \beta)(p_w - \dot{\alpha} \sin \beta) - a_n/V - \dot{\alpha} \quad (B-7)$$

Equations for the dynamics of  $\delta V_y$  and  $\delta V_z$  can be derived by a similar process. The results are

$$\begin{aligned} \delta \dot{V}_y &= a_{nT} \sin(\delta \phi_V) - a_y + (\delta V_z)(p_w - \dot{\alpha} \sin \beta) \\ &\quad - (\delta V_x)(a_y/V) \end{aligned} \quad (B-8)$$

$$\begin{aligned}\delta\dot{V}_z = & - a_{nT} \cos(\delta\phi_v) + a_n - (\delta V_y)(p_w - \dot{\alpha} \sin \beta) \\ & + (\delta V_x) (a_n/V)\end{aligned}\quad (B-9)$$

where  $\delta\phi_v$  is defined as shown in Fig. 44b.

An attempt was made to calculate the target acceleration ( $a_{nT}$ ) and roll ( $\phi_{vT}$ ) time history from the available data ( $\varepsilon_n, \varepsilon_y, a_n, a_y, \alpha, \beta$ ) but was unsuccessful due to the amount of differentiation of the input time histories necessary. Because of this difficulty the tracking equations are simplified by assuming that  $\delta V_x$  and  $p_w - \dot{\alpha} \sin \beta$  are identically zero. Further simplification occurs by noting that near steady state, the perturbation velocities can be expressed as

$$\delta V_y = R(a_y/V) + \delta\dot{V}_y \Delta t \quad (B-10)$$

$$\delta V_z = R(-a_n/V) + \delta\dot{V}_z \Delta t \quad (B-11)$$

Using  $R/V$  as the time interval  $\Delta t$  in Eq. B-10 and B-11 allows these short term approximations to be inserted into Eqs. B-6 and B-7. The derivatives  $\delta\dot{V}_y$  and  $\delta\dot{V}_z$  can then be eliminated from Eqs. B-6 and B-7 by inserting Eqs. B-8 and B-9. This produces the final simplified nonlinear equations.

$$\dot{\varepsilon}_y = (-1/V) (a_{nT} \sin(\delta\phi_v) - a_y) - \dot{\beta} \quad (B-12)$$

$$\dot{\varepsilon}_n = (1/V) (a_{nT} \cos(\delta\phi_v) - a_n) - \dot{\alpha} \quad (B-13)$$

These equations enable the identification of the target trajectory, and also form the basis for the final linearized equations, which assume  $a_{nT} = a_{n_0}$ , and  $\delta\phi_{v_0} = 0$ . These linearized equations are

$$\Delta\dot{\varepsilon}_y = (-1/V_0)(a_{nT_0})(\Delta\delta\phi_v) + (1/V_0)\Delta a_y - \Delta\dot{\beta} \quad (B-14)$$

$$\Delta \dot{\epsilon}_n = (1/V_o)(\Delta a_{n_T} - \Delta a_n) - \Delta \dot{\alpha} \quad (B-15)$$

The lateral tracking equation, Eq. B-14, is used in Chapter 4 in the construction of an air combat pilot model.

## APPENDIX C

### HYPOTHESIS TESTING

This appendix gives the detailed equations for the hypothesis testing procedure used in Chapter 4. The procedure is based on a model structure identification algorithm modified to allow for changes in the true hypothesis.

The hypothesis testing philosophy for investigating pilot control adaptation in flight is to construct a number of different pilot models and then determine which pilot model best represents the pilot control behavior. The  $i^{\text{th}}$  pilot model is represented by the discrete-time equation

$$\begin{bmatrix} \Delta u \\ \Delta \hat{x}_E \\ \Delta z \end{bmatrix}_{k+1} = \Phi_{PM}^i \begin{bmatrix} \Delta u \\ \Delta \hat{x}_E \\ \Delta z \end{bmatrix}_k + \Gamma_{PM}^i \Delta y_k + \Gamma_W^i \Delta w_k^i \quad (C-1)$$

The pilot model is taken from Ref. 23 where the pure time delay in the optimal control pilot model is replaced by a Padé approximation. The steps for arriving at Eq. C-1 are discussed in Section 4.1. In Eq. C-1,  $\Delta u_k$  is the control predicted by the pilot model,  $\Delta \hat{x}_E$  is the state vector of the pilot model's internal Kalman filter,  $\Delta z_k$  are states associated with the Padé approximation,  $\Delta y$  are the assumed observations of the pilot, and  $\Delta w_k$  is the process noise of the pilot model.

The method for determining which pilot model provides the best fit at any given time is taken from Refs. 30 and 31

and illustrated in Fig. C-1. The notation used in the figure is as follows:

$\Delta \underline{u}_{m,k}$ : measured value of pilot perturbation control at time  $t_k$

$\Delta \underline{y}_k$ : measured values of perturbation states assumed observed by pilot

$\Delta \hat{\underline{u}}_k^i(-)$ : one-step predicted value of  $\Delta \underline{u}_{m,k}$  based upon  $\{\Delta \underline{u}_{m,1}, \dots, \Delta \underline{u}_{m,k-1}\}$  and  $\{\Delta \underline{y}_1, \dots, \Delta \underline{y}_{k-1}\}$  for the  $i^{\text{th}}$  pilot model Kalman filter

$\Delta \hat{\underline{r}}_k^i$ : one-step predicted residual at the  $k^{\text{th}}$  step for the  $i^{\text{th}}$  pilot model Kalman filter

$P_{H,i}^{(k)}$ : probability that the  $i^{\text{th}}$  pilot model is best, based upon knowledge of  $\{\Delta \underline{u}_{m,1}, \dots, \Delta \underline{u}_{m,k-1}\}$  and  $\{\Delta \underline{y}_1, \dots, \Delta \underline{y}_{k-1}\}$

The pilot model Kalman filter is constructed using Eq. C-1 as the plant,  $\Gamma_w \Delta \underline{w}_k$  as the plant process noise,  $\Delta \underline{y}_k$  as the known plant inputs, and the observation is

$$\Delta \underline{u}_{m,k} = [I \quad 0 \quad 0] \begin{bmatrix} \Delta \underline{u} \\ \Delta \hat{\underline{x}}_E \\ \Delta \underline{z} \end{bmatrix}_k + \Delta \underline{v}_k \quad (\text{C-2})$$

For our purposes,  $\Delta \underline{v}_k$  is the measurement noise encountered when attempting to measure the actual pilot controls. The data analyzed in Chapter 4 exhibited very low measurement noise on the pilot controls and  $\Delta \underline{v}_k$  is assumed to be zero. The pilot model Kalman filter just described is not to be confused with the internal Kalman filter in the pilot model.

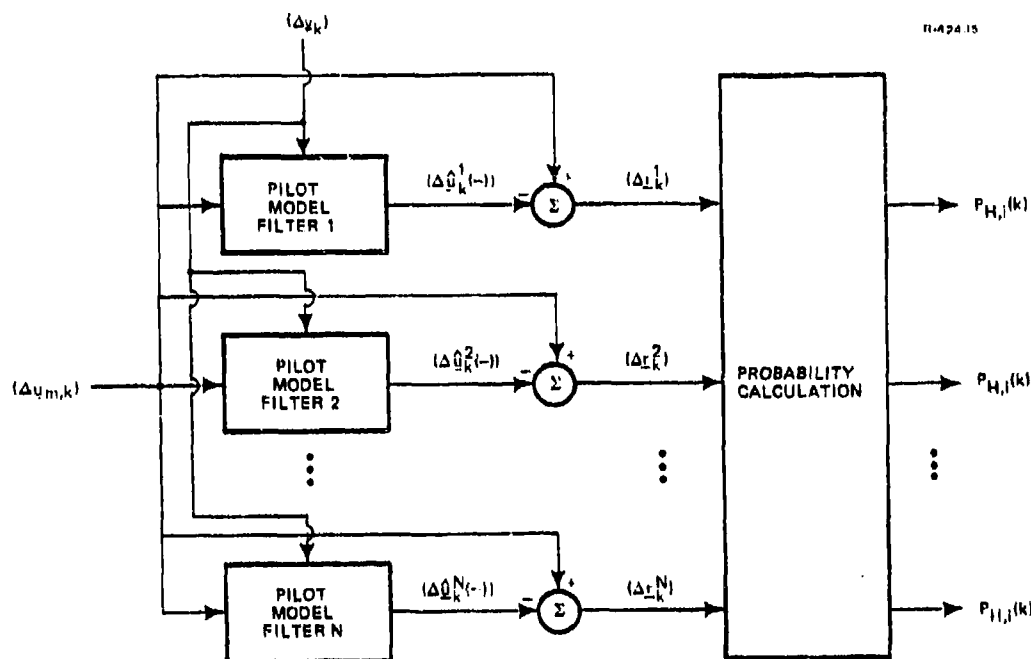


Figure C-1 Kalman filter Approach to Pilot Control Strategy Hypothesis Testing

The output of the  $i^{\text{th}}$  pilot model filter is a state estimate  $[\Delta \hat{u}^T(-), \Delta \hat{x}_E^T(-), \Delta \hat{z}^T(-)]_k^i$  of the pilot's internal perturbation states and controls based upon the first  $k-1$  input-output pairs,

$$\begin{bmatrix} \Delta \hat{u}(-) \\ \Delta \hat{x}_E(-) \\ \Delta \hat{z}(-) \end{bmatrix}_k^i = \Phi_{PM}^i \begin{bmatrix} \Delta \hat{u}(+) \\ \Delta \hat{x}_E(+) \\ \Delta \hat{z}(+) \end{bmatrix}_{k-1}^i + \Gamma_{PM}^i \Delta y_{k-1} \quad (C-3)$$

The update part of the pilot model Kalman filter is

$$\Delta \underline{r}_k^i = \Delta \underline{u}_{m,k} - [I \ 0 \ 0] \begin{bmatrix} \Delta \hat{\underline{u}}(-) \\ \Delta \hat{\underline{x}}_E(-) \\ \Delta \hat{\underline{z}}(-) \end{bmatrix}_{-k}^i \quad (C-4)$$

$$\begin{bmatrix} \Delta \hat{\underline{x}}_x(+) \\ \Delta \hat{\underline{x}}_E(+) \\ \Delta \hat{\underline{z}}(+) \end{bmatrix}_k^i = \begin{bmatrix} \Delta \hat{\underline{u}}(-) \\ \Delta \hat{\underline{x}}_E(-) \\ \Delta \hat{\underline{z}}(-) \end{bmatrix}_{-k}^i + K^i \Delta \underline{r}_k^i \quad (C-5)$$

The matrix  $K^i$  is the steady-state pilot model Kalman filter gain for the  $i^{\text{th}}$  pilot model.

For notational purposes, let

$$\underline{U}_k = \{\Delta \underline{u}_{m,1}, \dots, \Delta \underline{u}_{m,k}\} \quad (C-6)$$

Applying Bayes' rule, one can write:

$$\begin{aligned} P_{H,i}(k) &\triangleq P(H,i|\underline{U}_k) \\ &= P(H,i|\Delta \underline{u}_{m,k}, \underline{U}_{k-1}) \\ &= \frac{P(\Delta \underline{u}_{m,k}|H,i,\underline{U}_{k-1})P(H,i|\underline{U}_{k-1})}{P(\Delta \underline{u}_{m,k}|\underline{U}_{k-1})} \\ &= \frac{P(\Delta \underline{u}_{m,k}|H,i,\underline{U}_{k-1})P(H,1)\underline{U}_{k-1}}{\sum_{i=1}^N P(\Delta \underline{u}_{m,k}|H,i,\underline{U}_{k-1})P(H,i|\underline{U}_{k-1})} \\ &= \frac{P(\Delta \underline{u}_{m,k}|H,i,\underline{U}_{k-1})P_{H,i}(k-1)}{\sum_{i=1}^N P(\Delta \underline{u}_{m,k}|H,i,\underline{U}_{k-1})P_{H,i}(k-1)} \quad (C-7) \end{aligned}$$

Using the fact that  $\Delta \underline{w}_k$  is assumed to be a zero-mean gaussian sequence, along with the assumption the Kalman filter state vector  $[\Delta \hat{\underline{u}}^T(-), \Delta \hat{\underline{x}}_E^T(-), \Delta \hat{\underline{z}}^T(-)]^T$  is also gaussian, it follows that

$$P(\Delta \underline{u}_{m,k} | H, i, U_{k-1}) \approx \frac{1}{(2\pi)^{m/2} |\det S^i|^{\frac{1}{2}}} e^{-\frac{1}{2}(\Delta \underline{r}_k^i)^T (S^i)^{-1} (\Delta \underline{r}_k^i)} \quad (C-8)$$

where

$$S^i = [I \ 0 \ 0] P^i(-) \begin{bmatrix} I \\ 0 \\ 0 \end{bmatrix} \quad (C-9)$$

$P^i(-)$ : a priori steady state error covariance matrix computed using  $i^{\text{th}}$  pilot model Kalman filter

Note that the  $P_{H,i}(k)$  are computed recursively. In addition, it should be mentioned that the approximation shown in Eq. C-8 is based on the assumption that the "true" hypothesis remains constant. If the true hypothesis changes with time, the probability density function in Eq. C-8 must be conditioned on the hypothesis values at all previous times. This leads, as time progresses, to an expanding "tree" of hypotheses. It is necessary to calculate  $P_{H,i}(k)$  for each of these hypotheses. Since this imposes an excessive computational burden, an efficient suboptimal approach to the problem is developed in Ref. 30. The suboptimal approach is nearly optimal in situations where the probability of switching hypotheses at any given time is low. The suboptimal approach is derived by noting that if the  $i^{\text{th}}$  pilot model is true then the recursive calculation in Eq. C-7 causes  $P_{H,i}$  to approach 1. If  $P_{H,i}$  should



equal one, it will remain "trapped" at one regardless of changes in the pilot's control strategy. To prevent this, Eqs. C-2 and C-3 are modified in the following fashion. Define a parameter  $\varepsilon$  corresponding to the minimum value that one of the  $P_{H,i}(k)$  can fall to and still "recover" if  $H_i$  suddenly becomes the true hypothesis. (In the simulation studies reported in Ref. 30,  $\varepsilon=0.05$  was found to be a good value and is used in Chapter 4). Define

$$\delta(k) \triangleq \sum_{\{i: P_{H,i}(k) < \varepsilon\}} [\varepsilon - P_{H,i}(k)] \quad (C-10)$$

$$m(k) \triangleq \text{number of } P_{H,i}(k) \text{ that are greater than } 2\varepsilon \quad (C-11)$$

where the symbology in the equation for  $\delta(k)$  is meant to denote the fact that the sum is taken over all  $i$  such that  $P_{H,i} < \varepsilon$ . First update the  $P_{H,i}(k)$  using Eqs. C-7 and C-8 then reset these probabilities as follows:

- If  $P_{H,i}(k) < \varepsilon$ , set  $P_{H,i}(k) = \varepsilon$
- If  $P_{H,i}(k) > 2\varepsilon$  and  $\delta(k) > 0$ , set
 
$$P_{H,i}(k) = \left[ P_{H,i}(k) \right]_{\text{old}} - \frac{\delta(k)}{m(k)} \quad (C-12)$$

where  $\left[ P_{H,i}(k) \right]_{\text{old}}$  denotes the value obtained from Eq. C-7.

The reset procedure guarantees that all of the  $P_{H,i}(k)$  are greater than (or equal to)  $\varepsilon$  and that they sum to one. Returning to the previous example, the problem of  $P_{H,i}(k)$  becoming so small that it cannot recover when the true hypothesis switches to  $H_i$  is now avoided. In addition, the procedure

can be implemented with only  $N$  parallel filters. The simulation results in Chapter 4 indicate that this suboptimal procedure is effective in detecting changes in the true hypothesis.

The above hypothesis testing procedure can be generalized. The  $i^{\text{th}}$  pilot model matrices in Eq. C-1 can be time-varying and the pilot model can even be nonlinear. The time-varying Kalman filter can be used in the former assumption and the extended Kalman filter can be used in the latter assumption.

# APPENDIX D LIST OF SYMBOLS

In general, matrices are represented by capital letters and vectors are underscored; exceptions to these rules are only made when they are contradicted by standard aerodynamic notation. Capital script letters are used to denote scalars in some cases.

<u>VARIABLE</u>	<u>DESCRIPTION</u>
a	Control deflection weighting scalar
$a_n$	Normal acceleration (inertial acceleration normal to the velocity vector in the body x-z plane - including gravitational acceleration)
b	Wing span
C	Gain Matrix (Type 1) Pilot control-strategy feedback matrix
$C_{12}$	Partial derivative of the nondimensional coefficient of force or moment 1 with respect to the nondimensional variable 2 (scalar)
$\bar{c}$	Mean aerodynamic chord
D	Control observation matrix
F	System dynamics matrix
$\underline{F}$	Aerodynamic contact force vector
$\underline{f}$	Vector-valued nonlinear function for system dynamics
G	Control input allocation matrix
$\underline{G}$	Thrust moment vector
g	Magnitude of $\underline{g}$ ( $=  \underline{g} $ )

$g$	Gravitational acceleration vector Vector-valued nonlinear function for output equations
$H$	Aircraft state observation matrix
$H_E$	Total pilot observation matrix for pilot model
$H_1^2$	Euler angle transformation from Frame 1 axes to Frame 2 axes
$h$	Altitude
$\underline{h}$	Angular momentum vector
$I$	Identity matrix
$I_B$	Rotational inertia matrix
$J$	Cost functional
$K$	Gain matrix (Type 0) Pilot Kalman filter gain matrix
$L$	Angular velocity transformation matrix Aerodynamic moment about the x-axis (scalar)
$l$	Number of outputs
$M$	Aerodynamic moment about the y-axis (scalar) Weighting matrix on state-control rate and control-control rate products
$\underline{M}$	Aerodynamic contact moment vector
$m$	Mass of the vehicle Number of controls Number of pilot model probabilities that exceed a specified level
$N$	Aerodynamic moment about the z-axis (scalar)
$n$	Number of states
$P$	Riccati matrix in the optimal regulator problem
$P_H$	Probability that a pilot model among a set of pilot models is correct

$P_u$	Pilot noise-to-signal ratio for neuromotor noise
$p$	Rotational rate about the body x-axis
$Q$	State weighting matrix
$q$	Rotational rate about the body y-axis
$q_\infty$	Free stream dynamic pressure ( $=\frac{1}{2}\rho_\infty V^2$ )
$R$	Control or control-rate weighting matrix
$R_L$	Matrix with diagonal consisting of the inverse of human neuromuscular time constants
$r$	Rotational rate about the body x-axis
$\underline{r}$	Kalman filter innovations vector
$S$	Reference area (usually wing area for aircraft). Covariance matrix of Kalman filter innovations vector
$T$	Thrust force magnitude ( $ \underline{T} $ )
$\underline{T}$	Thrust force vector
$t$	Time
$U$	A set of control vectors ordered in time
$u$	Body x-axis velocity component
$\underline{u}$	Control vector
$\underline{u}_c$	Pilot model control command
$V$	Inertial velocity magnitude ( $ \underline{V} $ ) Covariance matrix for pilot control measurement noise
$\underline{V}$	Velocity vector of body observed from inertial axes
$V_u$	Pilot neuromotor noise covariance matrix
$V_y$	Pilot observation noise covariance matrix
$v$	Body y-axis velocity component

$\underline{v}$	Pilot control measurement noise vector
$\underline{v}_u$	Pilot neuromotor noise vector
$\underline{v}_y$	Pilot observation noise vector
$w$	Body z-axis velocity component
$\underline{w}$	Total disturbance vector (including pilot noise)
$X$	Aerodynamic force along the x-axis (scalar)
$x$	Position along the x-axis
$\underline{x}$	State vector
$x_{cg}$	Longitudinal distance between actual c.g. location and point used for aerodynamic moment measurements (expressed in body axes)
$Y$	Aerodynamic force along the y-axis (scalar)
$y$	Position along the y-axis
$\underline{y}$	Pilot observation vector
$\underline{y}_E$	Lagged pilot observation vector
$Z$	Aerodynamic force along the z-axis (scalar)
$z$	Position along the z-axis
$\underline{z}$	Lagged states associated with the Padé approximation

VARIABLE  
(GREEK)

DESCRIPTION

$\alpha$	Wind-body pitch Euler angle (angle of attack)
$\beta$	Negative of wind-body yaw Euler angle (sideslip angle)
$\Gamma$	Discrete time control effect matrix
$\gamma$	Inertial-velocity axis pitch Euler angle (flight-path angle)

$\delta$	The number of pilot model probabilities that are less than a specified level
$\delta_{ds}$	Differential stabilator deflection
$\delta_{mf}$	Maneuver flap deflection
$\delta_r$	Rudder deflection
$\delta_s$	Symmetric or collective stabilator deflection
$\delta_{sp}$	Spoiler deflection
$\varepsilon$	Tracking error
$\xi$	Damping ratio
$\theta$	Inertial-body pitch Euler angle
$\lambda$	Eigenvalue
$\underline{v}$	Aircraft orientation vector
$\xi$	Inertial-velocity axis yaw Euler angle (velocity heading angle)
$\rho$	Correlation coefficient
$\rho_\infty$	Air density
$\sigma$	Real part of an eigenvalue in radians/sec
$\tau$	Pilot time delay
$\tau_n$	Human neuromuscular time constant
$\Phi$	Discrete time state transition matrix
$\phi$	Inertial-body axis roll Euler angle
$\phi_v$	Stability-axis roll angle
$\psi$	Inertial-body axis yaw Euler angle
$\Omega$	System inverse matrix
$\omega$	Frequency in radians/sec; imaginary part of an eigenvalue

$\underline{w}_1^2$ 

Rotational rate vector of Reference Frame 2 with respect to Reference Frame 1 and expressed in Frame 1 coordinates.

( $\underline{w}_1^2 = H_2^1 \underline{w}_2^1$  so  $\underline{w}_2^1$  is left-handed. Thus, Frame 1 and Frame 2 are not interchangeable.)

VARIABLE  
(SUBSCRIPT OR  
SUPERSCRIPT

DESCRIPTION

a	Aircraft dynamics
B	Body axes
c	Commanded value
D	Discrete time matrices for optimal control law
d	Desired value
E	Earth axes (north, east, down) Conglomerated pilot model matrices
I	Inertial axes
i	Pilot model index
k	Time index for discrete time quantity
l	Aerodynamic moment about the x-axis
m	Aerodynamic moment about the y-axis
n	Aerodynamic moment about the z-axis
O	Nominal value about which linearization occurs
PM	Pilot Model
s	Pseudoinverse weighting matrix
T	Target dynamics
V	Velocity axes
W	Wind axes (same as stability axes for $\beta_0 = \alpha_0 = 0$ )



x	Component along the x-axis
y	Component along the y-axis
z	Component along the z-axis
X	Aerodynamic force along the x-axis
Y	Aerodynamic force along the y-axis
Z	Aerodynamic force along the z-axis

# OPERATOR

# DEFINITION

( $\dot{\phantom{x}}$ )	Time derivative
( $\sim$ )	Matrix equivalent to vector crossproduct. Specifically, if $\underline{x}$ is the three-dimensional vector
$\underline{x} = \begin{bmatrix} x \\ y \\ z \end{bmatrix}, \text{ then } \tilde{x} = \begin{bmatrix} 0 & -z & y \\ z & 0 & -x \\ -y & x & 0 \end{bmatrix}$	
and the cross product of $\underline{x}$ and $\underline{f}$ is equal to the product of the matrix $\tilde{x}$ and the vector $\underline{f}$ ,	
$\underline{x} \times \underline{f} = \tilde{x} \underline{f}$	
(-)	The one step predicted estimate of a quantity immediately before measurement
(+)	The best estimate of a quantity immediately after a measurement
( $\sim$ )	Difference between a vector and its expected value
( $\wedge$ )	Estimated value
( $\phantom{x}$ ) <sup>T</sup>	Transpose of a vector or matrix
( $\phantom{x}$ ) <sup>-1</sup>	Inverse of a matrix
( $\phantom{x}$ )'	Limited value
( $\phantom{x}$ ) <sup>*</sup>	Perfect model following values

$\Delta( )$	Perturbation about the nominal value of a variable
$\delta( )$	The variable is the difference between the target variable and the aircraft variable
$e( )$	Exponential of ( )
$( )^R$	Right pseudoinverse of a matrix
$( )_{\max}$	Maximum value, usually due to displacement of an actuator.
$\angle( )$	Clockwise angular rotation
$(\bar{\phantom{x}})$	Nondimensional or average value

<u>ACRONYM</u>	<u>CORRESPONDING PHRASE</u>
ACM	Air Combat Maneuvering
ARI	Aileron-Rudder Interconnect
cas	Command Augmentation System
CGT	Command Generator Tracker
CILOP	Conversion in lieu of procurement
c.g.	Center of Gravity
DFCS	Digital flight control system
DOF	Degrees of Freedom
DMS	Differential Maneuvering Simulator
NASA	National Aeronautics and Space Administration
NL	Nonlinear
PI	Proportional Integral
PIO	Pilot Induced Oscillation
sas	Stability Augmentation System
VALT	VTOL Approach and Landing Technology

# DISTRIBUTION LIST

Office of Naval Research 800 N. Quincy St. Arlington, VA 22217 R. von Husen, Code 211 S. L. Brodsky, Code 432	4 1	David Taylor Naval Ship R&D Center Bethesda, MD 20084 Technical Library	1
Office of Naval Research Eastern/Central Regional Office 495 Summer St. Boston, MA 02210	1	Naval Post Graduate School Monterey, CA 93940 Technical Reports Library L. Schmidt	1 1
Office of Naval Research Western Regional Office 1030 E. Green St. Pasadena, CA 91106	1	Defense Technical Information Center Building 5 Cameron Station Alexandria, VA 22314	12
Naval Research Laboratory Washington, DC 20375 Code 2627	3	Air Force Office of Scientific Research Building 410 Bolling Air Force Base Washington, DC 20332 G. W. McKemie	1
Naval Air Systems Command Washington, DC 20361 D. Kirkpatrick, AIR 320D R. C. A'Harrah, AIR 53011	1 1	Air Force Flight Dynamics Laboratory Wright-Patterson Air Force Base Dayton, OH 45433 R. Anderson, Control Dyn. Br. F. George, Control Dyn. Br.	1 1
Naval Air Development Center Warminster, PA 19874 C. J. Mazza, Code 6053 C. R. Abrams, Code 6072	1 1	Air Force Institute of Technology Wright-Patterson Air Force Base Dayton, OH 45433 P. Maybeck	1
Naval Material Command Washington, DC 20360 Code 08T23	1	Army Armament R&D Command Building #18 Dover, NJ 07801 N. Coleman, DRDAR-SCFCC	1
Naval Weapons Center China Lake, CA 93555 B. Hardy, Code 3914	1	NASA Langley Research Center Hampton, VA 23665 J. R. Chambers E. Anglin	1 1
Naval Surface Weapons Center Silver Spring, MD 20910 J. Wingate, Code R44	1	NASA Dryden Research Center P. O. Box 273 Edwards, CA 93523 Technical Library	1
Naval Air Test Center Patuxent River, MD 20670 J. McCue, Code TPS	1		

ENCLOSURE (3)

Systems Technology, Inc.  
13766 South Hawthorne Blvd.  
Hawthorne, CA 90250  
R. Whitbeck

1

Massachusetts Institute of Technology  
Lab. for Information and Decision  
Systems  
Cambridge, MA 02139  
M. Athans

1

University of Michigan  
Dept. of Naval Architecture & Marine  
Engr.  
Ann Arbor, MI 48109  
M. G. Parsons

1

Nielsen Engineering & Research, Inc.  
510 Clyde Avenue  
Mountain View, CA 94043  
J. N. Nielsen

1

University of Notre Dame  
Dept. of Electrical Engineering  
Notre Dame, IN 46556  
M. K. Sain

1

The C. S. Draper Laboratory, Inc.  
555 Technology Square  
Cambridge, MA 02139  
R. V. Ramnath

1

Honeywell, Inc.  
Systems and Research Center  
2600 Ridgway Parkway  
Minneapolis, MN 55413  
C. A. Harvey

1

Alphatech, Inc.  
3 New England Executive Park  
Burlington, MA 01803  
N. R. Sandell

1

Scientific Systems, Inc.  
Suite No. 309-310  
186 Alewife Brook Parkway  
Cambridge, MA 02138  
R. K. Mehra

1

Calspan Corp.  
P. O. Box 400  
Buffalo, NY 14225  
E. G. Rynaski  
K. S. Govindaraj

Systems Control Inc.  
1801 Page Mill Road  
Palo Alto, CA 94306  
E. Hall

Flight Research Laboratory  
Dept. of Mechanical & Aerospace  
Engineering  
Princeton University  
Princeton, NJ 08544  
R. F. Stengel

National Transportation Safety Board  
Bureau of Technology  
Laboratory Services Division  
800 Independence Ave., SW  
Washington, DC 20394  
R. von Husen